



KTH Electrical Engineering

Synchronous Reluctance Machine (SynRM) Design

by

Reza Rajabi Moghaddam

Master Thesis

Supervisor:

Dr. Freddy Magnussen

Examiner:

Prof. Chandur Sadarangani

Royal Institute of Technology

Department of Electrical Engineering

Electrical Machines and Power electronics

Stockholm 2007

To my Parents

در بازار کوزه گری رفتم و دوش
 دیدم ده هزار کوزه گویا و خوش
 ناگهان یکی کوزه برآورد و خردش
 کوزه گر کوزه خرد کوزه فروش

Literal:

Once upon a time, in a potter's shop
 I saw two thousand clay pots and cup
 Suddenly a lone pot cried out, "stop!
 Where the vendor, buyer, where my prop?"

OR

To a pottery I went by chance
 Two thousand pots I saw in a glance
 Cried out a pot awakened from trance
 "whither potter, vendor and buyer prance?"

Meaning:

We simply exist, silent, unaware
 Busy with minute mundane worldly care
 Occasionally find someone who'll dare
 To ask why we came, and from here go where?

Fitzgerald:

And strange to tell, among that Earthen Lot
 Some could articulate, while others not:
 And suddenly one more impatient cried--
 "Who is the Potter, pray, and who the Pot?"



Omar **Khayyam** Nishapuri

1048 - 1123 CE
 Nishapur, Persia (Iran)

	<p style="text-align: center;">MSc Final Project Report</p> <p style="text-align: center;">ABB Corporate Research & KTH</p>	
Doc. title	By: Reza Rajabi Moghaddam	Page
Synchronous Reluctance Machine Design		I

Abstract

The Synchronous Reluctance Motor (SynRM) has been studied. A suitable machine vector model has been derived. The influence of the major parameters on the motor performance has been theoretically determined.

Due to the complex rotor geometry in the SynRM, a suitable and simple combined theoretical (analytical) and finite element method has been developed to overcome the high number of involved parameters by identifying some classified, meaningful, macroscopic parameters.

This macroscopic parameters are for example: insulation ratio in q- and d-axis, number of barriers, number of poles, end points of barriers in the air gap, type of barrier distribution ie. with- or without-cut-off, stator slots per pole per phase (q). Intermediate variables are barriers position and sizes.

Reducing the number of parameters effectively was one of the main goals. For this purpose, attempt has been made to find and classify different parameters and variables, based on available literatures and studies. Thus a literature study has been conducted to find all useful ideas and concepts regarding the SynRM. The findings have been used to develop a simple, general, finite element aided and fast rotor design procedure. By this method rotor design can be suitably achieved by related and simplified finite element sensitivity analysis.

The procedure have been tested and confirmed. Then it is used to optimize a special rotor for a particular induction machine (IM) stator. This optimization is mainly focused on the torque maximization for a certain current. Torque ripple is also minimized to a practically acceptable value. The procedure can also be used to optimize the rotor geometry by considering the other machine performance parameters as constrains.

Finally full geometrical parameter sensitivity analysis is also done to investigate the influence of the main involved design parameters on the machine performance.

Some main characteristics like magnetization inductances, power factor, efficiency, overload capacity, iron losses, torque and torque ripple are calculated for the final designs and in different machine load conditions.

Effects of ribs, air gap length and number of barriers have been investigated by means of suitable FEM based method sensitivity analysis.

Keywords

Synchronous reluctance motor, sensitivity analysis, main parameter, transversally laminated anisotropy, design, vector model, torque ripple minimization, torque maximization, optimization, geometric parameter, saliency ratio, finite element analysis, theoretical rotor geometry model, combined optimization.

	<p style="text-align: center;">MSc Final Project Report</p> <p style="text-align: center;">ABB Corporate Research & KTH</p>	
Doc. title	By: Reza Rajabi Moghaddam	Page
Synchronous Reluctance Machine Design		II

Preface

Certainly this work will never be perfect, because the writer is taking his first steps towards the electrical engineering world. In this situation lack of perfect knowledge is normal.

It must also be taken into account that this work has been an MSc final project and it is clear that the lack of time has also affected the quality.

Thus expecting comprehensive solutions is unrealistic. Instead the writer has tried to find critical questions and ignite some new questions for the readers, because good and relevant questions can in itself be part of the solution. The project has thus focused on gathering and classifying as much material as possible that is related to the main subject.

All new ideas and critics will be very warmly welcomed by the author, who is looking for deeper insight towards, especially the subjects of iron losses, torque ripple, control, thermal behavior, and flux fluctuation in the rotor and so on.

Acknowledgement

This master thesis has been carried out at ABB Corporate Research in Västerås, Sweden and at the department of Power Technologies group of Electrical Machines and Intelligent Motion in cooperation with the School of Electrical Engineering, Royal Institute of Technology (KTH) during the 5 months.

First of all, I would like to express my deepest appreciation to my supervisor Dr. Freddy Magnussen for all his assistances during this master thesis work. Special thanks also to Heinz Lendenmann head of the group in ABB for his friendly support.

I am also very grateful to Prof. Peter Isberg and Dr. Gunnar Kylander from ABB LV. Motors and the constructive meetings we had on practical issues of motor design, construction and manufacturing.

I am grateful to Prof. Chandur Sadarangani for introducing me to ABB at the very beginning. My sincere appreciation also goes to Prof. Chandur Sadarangani for his invaluable discussions and examining my thesis and his comprehensive suggestions and corrections to the final report.

I would like to thank all the other personal of ABB Corporate Research in particular Dr. Hector Zelaya De La Parra and Dr. Stefan Toader for reviewing my report and for constructive comments and for helping me. It has been a pleasure to work in this friendly environment.

This is also time to gratefully thank the international MSc. Program coordinator of KTH School of Electrical Engineering, Dr. Mehdad Ghandehary, who admitted my application for the 2005 program and given me this opportunity study.

I would like also to thank all other members of the staff at the Power Engineering department, from whom I have learned a lot through different courses in the last 2 years. Their works really have changed and upgraded my personality and knowledge.

	<h1>MSc Final Project Report</h1> <p>ABB Corporate Research & KTH</p>	
Doc. title	By: Reza Rajabi Moghaddam	Page
Synchronous Reluctance Machine Design		III

I will send my deepest gratitude to my family. Thank you for your understandings and providing me an opportunity for study. Especial tanks to my brothers Mehdi Rajabi Moghaddam who encouraged me to continue my education and Ali Rajabi Moghaddam who fully supported me during my study at KTH for 2 years.

Finally, I gratefully present this work to my parents who could not realize their talents due to the hard living condition in their crowded families and also especially during the war between Iran and Iraq in the 1980s. They have never stopped teaching children for more than 30 years. All what I have is due to their self-denial and abnegation.

Rajabi Moghaddam Reza

Stockholm, Norooz (new spring), (April) 2007

TABLE OF CONTENTS

1	INTRODUCTION.....	1
	SYNCHRONOUS RELUCTANCE MACHINE (SYNRM) – BASIC PRINCIPLES	3
2	BASIC THEORY	3
2.1	RELUCTANCE CONCEPT.....	3
2.2	VECTOR EQUIVALENT CIRCUIT AND MAIN PERFORMANCE CHARACTERISTICS	4
2.3	MAGNETIZATION CHARACTERISTIC	8
2.3.1	Saturation	8
2.3.2	Cross-coupling	9
2.3.3	Slotted stator	9
3	ROTOR GEOMETRY REALIZATION TECHNIQUES	10
3.1	ROTOR GEOMETRY CLASSIFICATION AND DEVELOPMENT HISTORY	10
3.2	TLA AND ALA COMPARISON	13
3.3	COMPARISON OF SYNRM AND IM.....	14
4	BASIC CONTROL CONCEPTS.....	15
	SYNRM – DESIGN ASPECTS.....	17
5	PARAMETER CLASSIFICATION AND DESCRIPTION FOR TLA-ROTOR.....	17
5.1	DESIGN OR SELECTED PARAMETERS	17
5.1.1	Power	17
5.1.2	Pole number $2p$	18
5.1.3	Flux barrier and segment.....	20
5.1.4	Rotor barrier Insulation ratio	24
5.1.5	Tangential and radial ribs	26
5.1.6	Air gap length	27
5.2	DESIGN VARIABLES	28
5.2.1	Position and Size of barriers	28
5.2.2	Basic theory of a transversally laminated anisotropic rotor (Barriers sizing)	29
5.2.3	Barriers positioning and segment sizing.....	32
5.3	TARGET VARIABLES	34
5.3.1	Torque per stator current and Efficiency	34
5.3.2	Iron losses and torque ripple	35
5.3.3	Torque per kVA & power factor	38
5.3.4	Inverter size and field-weakening range.....	39
5.3.5	Maximum saliency ratio, inductance difference and efficiency times power factor	41
6	PRIMARY DESIGN PROCEDURE	43
6.1	SCOPE	43
6.2	WITHOUT CUT-OFF DISTRIBUTION TYPE	43
6.2.1	End point angles (rotor slot pitch angle: α_m)	43
6.2.2	Segments width (S_k)	45
6.2.3	Barrier width in q-axis (W_{1_k})	46
6.2.4	Barrier width in d-axis (W_{k_d})	47
	SYNRM – FEM PARAMETERS SENSITIVITY ANALYSIS AND OPTIMIZATION	49
7	BASIC ROTOR STRUCTURES ANALYSIS.....	49
7.1	ONE BARRIER.....	49

7.1.1	Insulation ratio in q-axis.....	49
7.1.2	Barrier end points in the air gap and d-axis insulation ratio	52
7.1.3	Optimum q-axis barrier positioning.....	53
7.2	ONE BARRIER ANALYSIS CONCLUSIONS	54
7.3	ONE BARRIER AND ONE CUT-OFF	55
7.3.1	Theoretical model aided sensitivity analysis	55
7.3.2	Pure geometrical sensitivity analysis	57
7.3.3	Comparison	60
8	ELECTRO MAGNETIC SENSITIVITY ANALYSIS AND OPTIMIZATION (BASED ON THE THEORETICAL INITIAL DESIGN PROCEDURE).....	61
8.1	AVERAGE TORQUE OPTIMIZATION	61
8.1.1	Torque and torque ripple for different number of barriers.....	61
8.1.2	Number of layers effect on machine's inductances	62
8.1.3	Optimum number of barriers for maximum torque	63
8.2	TORQUE RIPPLE OPTIMIZATION	64
8.2.1	Torque and torque ripple	65
8.2.2	Torque ripple minimization for 4 barriers geometry.....	65
8.2.3	Torque ripple minimization results.....	67
8.3	MAIN MACHINES CHARACTERISTICS	69
8.3.1	Inductances for different current loading and d-q axis cross-coupling	69
8.3.2	IPF for different current loading	69
8.3.3	Torque vs. current angle curves	71
8.3.4	Torque, current characteristic	71
8.3.5	Maximum torque and power factor loci.....	72
8.3.6	Iron losses	72
8.4	FINAL COMPARISON.....	73
8.5	RIBS	74
8.5.1	Rib distribution	74
8.5.2	Rib width.....	74
8.5.3	Rib radius	74
8.6	AIR GAP LENGTH	75
8.6.1	Machine magnetizing inductances.....	75
8.6.2	Torque and torque ripple	75
8.6.3	IPF.....	76
8.6.4	Iron losses	77
8.6.5	Efficiency	77
8.7	OVER LOAD CAPACITY	78
9	CONCLUSIONS.....	79
10	FUTURE WORK	80
11	REFERENCES.....	81
12	APPENDICES.....	85
12.1	APPENDIX A: DIFFERENT POSSIBLE OPERATING POINTS FOR SYNRM	85
12.1.1	Comparison of point (A): max. T/A and (B): max. T/V for constant current	85
12.1.2	Comparison of point (A): min. Amp. and (C): min. voltage for certain torque.....	88
12.1.3	Comparison of point (A): max. T/A and (D): max. IPF for certain current	89
12.1.4	Comparison of point (A): min. current and point (G): max. IPF or min. kVA for certain torque.....	90
12.2	APPENDIX B: FIELD-WEAKENING RANGE CALCULATION.	91
12.2.1	Maximum torque strategy (T).....	91
12.2.2	Maximum power factor strategy (PF)	93
12.3	APPENDIX C: OPTIMUM INSULATION RATIO FOR A SIMPLE ANISOTROPIC STRUCTURE.....	93
12.4	APPENDIX D: TORQUE EQUATIONS IN CONSTANT CURRENT AND CONSTANT VOLTAGE CONDITIONS.....	95

	<p style="text-align: center;">MSc Final Project Report</p> <p style="text-align: center;">ABB Corporate Research & KTH</p>	
Doc. title	By: Reza Rajabi Moghaddam	Page
Synchronous Reluctance Machine Design		1

1 INTRODUCTION

The purpose of this report is to present information necessary for developing a suitable Synchronous Reluctance Motor (SynRM) rotor geometry design procedure.

To achieve this a suitable theoretical model is essential, thus a simple but complete motor model is developed.

To have a feeling about the potential position of the SynRM in industry a performance comparison between this machine and the other most used machines such as the IM will be presented. Special attention will be paid to the possible rotor geometries of SynRM, because as it has been shown by J. K. KOSTKO, 1923 [30] this can directly influence our insight on the machine's potential abilities.

These issues will give the readers a general insight on the machine's characteristic and also highlight the most important parameters of the machine that affect its performance.

The main task is to determine the influence of the major parameters on the motor performance. This can be suitably achieved by finite element sensitivity analysis.

Due to the complex rotor geometry in the SynRM, a suitable and simple combined theoretical (analytical) and finite element method is targeted to overcome the high number of involved parameters by identifying classified, meaningful, macroscopic parameters.

Reducing the number of parameters effectively was one of main goals. For this purpose, attempt has been made to find and classify different parameters and variables, based on available literatures and studies. A comprehensive literature study has been conducted to find all useful ideas and concepts regarding the SynRM. The findings have been used to develop a simple, general, finite element aided and fast rotor design procedure. Parameter classification resulted in the identification of three major classes of parameters:

- 1- Design parameters or macroscopic parameters (for example pole number, stator structure, insulation ratios in rotor ...).
- 2- Design variables or microscopic parameters (for example barrier's dimensions ...).
- 3- Target variables (for example torque density, efficiency, power factor ...).

The first group mainly includes parameters which due to their complexity and nonlinear effects, are preferably analyzed by the finite element method.

The second group includes variables that are mainly based on the rotor geometry.

The third group should be calculated from a finite element analysis in order to obtain accurate results.

Finally full parameter sensitivity analysis and optimization will be done.

Subject of this report have been divided into the following main categories:

- 1- SynRM basic principles, chapters 2, 3 and 4.
- 2- SynRM Design aspects, chapterd 5 and 6.
- 3- SynRM Finite element sensitivity analysis study and optimization, chapters 7 and 8.

The combined theory and finite element procedure which is suggested here should be used to reduce the number of barriers as much as possible (suitable for manufacturing and production) and not to find an absolute optimum design for a certain number of barriers. If only the torque maximization is targeted the procedure will work, but if other parameters like torque ripple and iron losses, especially in the rotor, are considered, then a more detailed model for controlling these two target variables is needed. For example such models which are based on analyzing the whole stator MMF harmonic content and rotor reaction are presented in [33, 39, 40].

Definitions:

SynRM	Synchronous Reluctance Motor
TLA	Transversally Laminated Anisotropic
ALA	Axially Laminated Anisotropic
Ld	d-axis inductance in the rotor reference frame
Lq	q-axis inductance in the rotor reference frame
HEV	Hybrid electric vehicle
FEM	Finite element modeling
IM	Induction Machine

SYNCHRONOUS RELUCTANCE MACHINE (SYNRM) – BASIC PRINCIPLES

2 BASIC THEORY

2.1 Reluctance concept

The synchronous reluctance machine (SynRM) utilizes the reluctance concept and rotating sinusoidal MMF, which can be produced by the traditional IM stator, for torque production. The reluctance torque concept has a very old history and it can be traced back to before 1900 [33, 30].

The main idea can be explained by Fig. 2.1. In this figure object (a) with an isotropic magnetic material has different (geometric) reluctances in the d-axis and the q-axis while the isotropic magnetic material in object (b) has the same reluctance in all directions.

A magnetic field (ψ) which is applied to the anisotropic object (a) is producing torque if there is an angle difference between the d-axis and the field ($\delta \neq 0$). It is obvious that if the d-axis of object (a) is not aligned with the field, it will introduce a field distortion in the main field. The main direction of this distortion field is aligned along the q-axis of the object.

In the SynRM field (ψ) is produced by a sinusoidally distributed winding in a slotted stator and it links the stator and rotor through a small air gap, exactly as in a traditional IM. The field is rotating at synchronous speed and can be assumed to have a sinusoidal distribution.

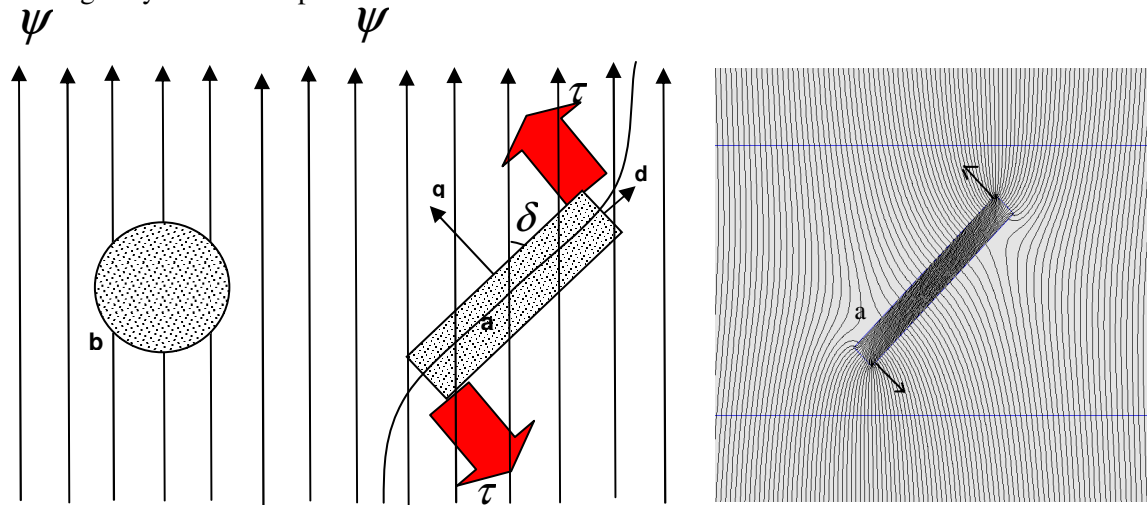


Fig. 2.1: An object with anisotropic geometry (a) and isotropic geometry (b) in a magnetic field ψ and torque production mechanism.

In this situation there will always be a torque which acts to reduce the whole system potential energy by reducing the distortion field in the q-axis, ($\delta \rightarrow 0$). If (δ) load angle is kept constant, for example by control or applying a load torque, then electromagnetic energy will be continuously converted to mechanical energy.

The stator current is responsible for both the magnetization (main field), and the torque production which is trying to reduce the field distortion, this can be done by controlling the current angle, which is the angle between the current vector of the stator winding and the rotor d-axis (θ) in synchronous reference frame [42, 26].

2.2 Vector equivalent circuit and main performance characteristics

Since the stator winding of the SynRM is sinusoidally distributed, flux harmonics in the air gap contribute only to an additional term in the stator leakage inductance [33, 10]. Hence the equations which describe the behavior of the SynRM can be derived from the conventional equations depicting a conventional wound field synchronous machine, which are Park's equations. In the SynRM, the excitation (field) winding is non-existent [33]. Also, the machine cage in the rotor is omitted and the machine can be started synchronously from stand still by proper inverter control [33].

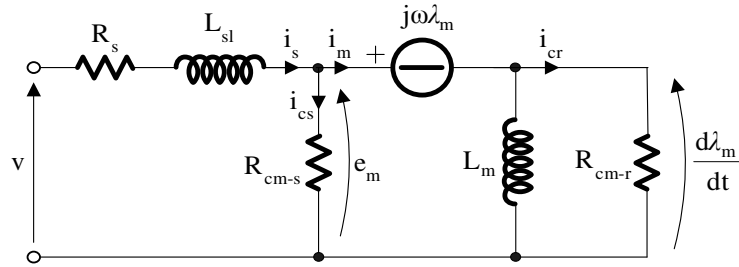


Fig. 2.2: Equivalent vector circuit of SynRM including rotor and stator iron losses [33].

Therefore by eliminating both the field and damper winding equations from Park's equations, the SynRM vector equations in the d-q-axis (synchronous reference frame) can be written as follows, see Fig. 2.2 and 2.3:

$$v = e_m + R_s i_s + j\omega L_{sl} i_s \quad (2.1)$$

$$e_m = \frac{d\lambda_m}{dt} + j\omega \lambda_m \quad (2.2)$$

In eqs. 2.1 and 2.2: $v = v_d + j \cdot v_q$ is the machine's terminal voltage vector, λ_m is the air gap linkage flux, L_{sl} is the total winding leakage inductance, R_s is the winding resistance, $i_s = i_{sd} + j \cdot i_{sq} = i_m + i_{cs}$ is the stator current vector, ω is the reference frame electrical angular speed and e_m is the air gap electromotive voltage (internal voltage of stator winding). Its RMS and argument values in steady state $\left(\frac{d\lambda_m}{dt} \cong 0\right)$ can be calculated from the following equation [33, 38], see Fig. 2.3:

$$|E_m| = \sqrt{2} \cdot N_1 \cdot \pi L D f \hat{B}_{\delta 1} = \sqrt{2} \cdot \left(\frac{n_s q k_{w1}}{C_s} \right) \cdot \pi L D f \hat{B}_{\delta 1}, \quad \arg(e_m) = \frac{\pi}{2} + \delta \quad (2.3)$$

In eq. 2.3: $e_m \rightarrow \text{vector}$ & $E_m \rightarrow \text{phasor}$, n_s is the number of conductors per stator slot, q is the number of stator slot per pole per phase, C_s is the winding connection factor [38], L is the machine active length, D is the air gap diameter, f is the supply frequency, k_{w1} is the fundamental winding factor¹, N_1 is the winding equivalent number of turns per pole per phase [38] and $\hat{B}_{\delta 1}$ is the maximum amplitude of the air gap fundamental flux density.

¹ This factor can be calculated as following, where y_{sp} is the phase winding pole pitch length in number of slots [38]:

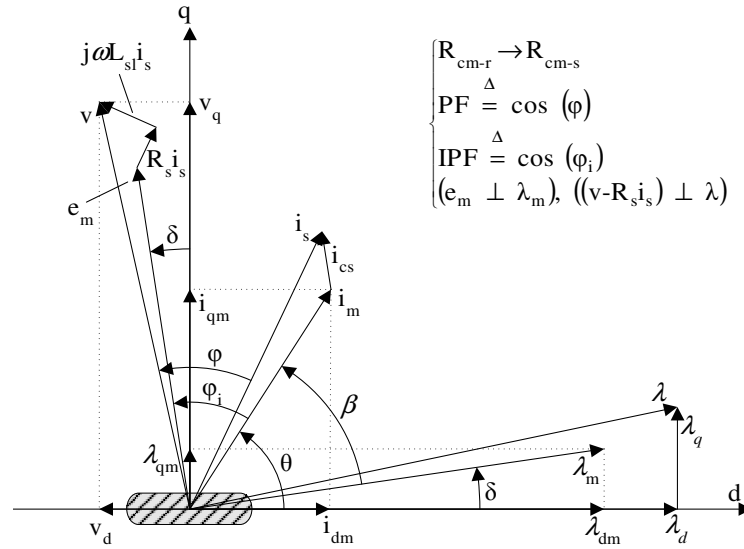


Fig. 2.3: Vector diagram of SynRM in steady state, including the total iron losses [33, 12].

Also, see Fig. 2.2:

$$\begin{aligned}
 e_m &= j\omega\lambda_m = j\omega(\lambda_{dm} + j\lambda_{qm}) = \\
 &= j\omega(L_{dm}(i_{dm}) \cdot i_{dm} + jL_{qm} \cdot i_{qm}) = \\
 &= -\omega L_{qm} \cdot i_{qm} + j\omega L_{dm}(i_{dm}) \cdot i_{dm}
 \end{aligned} \tag{2.4}$$

Note: In this report all calculations are based on the air gap values for the different parameters, because in Flux2D it is possible to evaluate the air gap values for the parameters independently. Also all iron losses in the equivalent circuit are transferred to the stator side and the equivalent rotor iron losses resistance R_{cm-r} is disregarded for simplicity [42, 18, 26]. Therefore λ_m according to the magnetization current $i_m = i_{dm} + j \cdot i_{qm}$ can be defined as following [33, 12]:

$$\begin{aligned}
 \lambda_m &= L_m \cdot i_m \cong \begin{bmatrix} L_{dm}(i_{dm}) & \sim 0 \\ \sim 0 & L_{qm} \end{bmatrix} \cdot i_m \\
 \lambda_m &= \lambda_{dm}(i_{dm}) + j \cdot \lambda_{qm}(i_{qm}) \cong \lambda_{dm}(i_{dm}) + j \cdot L_{qm} i_{qm}
 \end{aligned} \tag{2.5}$$

The flux in the d-axis can not be considered as a linear function of the current, but in the q-axis this is applicable with an acceptable accuracy. Generally there are two major side effects that can affect these assumptions: first the cross-coupling effect between the d- and q-axis, and second the stator slot effect [33, 31, 28]. Therefore the general flux equations can be written as in eq. 2.6. However in this report eqs. 2.4 and 2.5 will be used for the analysis and theoretical calculations.

$$\begin{aligned}
 \lambda_{dm} &= \lambda_{dm}(i_{dm}, i_{qm}, \vartheta) \\
 \lambda_{qm} &= \lambda_{qm}(i_{dm}, i_{qm}, \vartheta)
 \end{aligned} \tag{2.6}$$

$$k_{w1} = \frac{1}{q} \cdot \frac{\sin\left(\frac{\pi}{6}\right)}{\sin\left(\frac{\pi}{6q}\right)} \cdot \sin\left(\frac{y_{sp}\pi}{6q}\right)$$

In eq. 2.6, (ϑ) is the rotor position angle with reference to the stator and it shows the effect of the stator slot on main magnetizing inductances, this issue will be discussed later. The stator slot effect on stator leakage inductances in d- and q- axis is disregarded.

With the equivalent circuit, see Fig. 2.2, and vector diagram, see Fig. 2.3, the main machine characteristics can be calculated in steady-state according to the following.

The internal (or apparent or air gap) power factor can be written, [33, 31, 23, 7]:

$$\begin{aligned}
 IPF = \cos(\varphi_i) &= \sin(\beta) = \cos\left(\frac{\pi}{2} + \delta - \theta\right) = \\
 &= \cos\left(\tan^{-1}\left(\frac{\frac{L_{dm}}{L_{qm}} \frac{i_{dm}}{i_{qm}} + \frac{i_{qm}}{i_{dm}}}{\frac{L_{dm}}{L_{qm}} - 1}\right)\right) = \frac{(\xi - 1)}{\sqrt{\xi^2 \frac{1}{\sin^2 \theta} + \frac{1}{\cos^2 \theta}}} = \\
 &= (\xi - 1) \sqrt{\frac{\sin(2\theta)}{2(\tan \theta + \xi^2 \cot \theta)}} \quad (2.7)
 \end{aligned}$$

In eq. 2.7 $\left(\xi = \frac{L_{dm}(i_{dm})}{L_{qm}}\right)$ is the machine air gap saliency ratio and θ is the current angle, see

Fig. 2.3. The internal power factor is highly dependent of the machine saliency ratio and is maximized when $\tan(\theta) = \sqrt{\xi}$ [23]. Maximum IPF can be calculated according to the following equation:

$$IPF|_{\max} = \cos(\varphi_i)|_{\max} = \frac{\xi - 1}{\xi + 1} \quad (2.8)$$

The terminal power factor can be calculated according to the following [33, 9, 29]:

$$PF = \cos(\varphi) = \frac{v_d i_{sd} + v_q i_{sq}}{|v| \cdot |i_s|} \quad (2.9)$$

By eq. 2.3, the total iron losses equivalent resistance in the stator R_{cm} can be written as, see Fig. 2.2:

$$R_{cm} \cong \frac{3|E_m|^2}{P_{fe}^{tot}} \quad (2.10)$$

And the iron losses current will be as follows:

$$i_{cs} = \frac{e_m}{R_{cm}} \quad (2.11)$$

The electromagnetic torque including iron, friction and stray losses can be calculated with the air gap flux and magnetizing current according to eq. 2.12 [33, 12, 28]. In eq. 2.12, I_m is the stator magnetizing current RMS value, β is the angle between current and flux in the air gap, see Fig. 2.3, and p is the pole number. For the shaft torque calculation, the iron losses, friction and stray losses equivalent torque must be subtracted from the air gap total torque in eq. 2.12.

$$\begin{aligned}
T_{em-g} &= \frac{3}{2} \frac{p}{2} (\lambda_m \times i_m) = \frac{3}{2} \frac{p}{2} \cdot |\lambda_m| \cdot |i_m| \cdot \sin \beta = \\
&= \frac{3}{2} \frac{p}{2} (\lambda_{dm} i_{qm} - \lambda_{qm} i_{dm}) = \frac{3}{2} \frac{p}{2} (L_{dm}(i_{dm}) - L_{qm}) \cdot i_{dm} i_{qm} = \\
&= \frac{3}{2} \frac{p}{2} (L_{dm}(i_{dm}) - L_{qm}) \cdot I_m^2 \sin(2\theta) \tag{2.12}
\end{aligned}$$

This equation shows high dependency of the machine torque to the inductances difference $(L_{dm} - L_{qm})$ for certain stator current. The air gap back EMF, e_m can be introduced to the torque equation (eq. 2.12). Firstly for the back EMF we can write, refer to eq. 2.3 & 2.4, also see Fig. 2.3:

$$\begin{aligned}
\lambda_{dm} &= \frac{e_{qm}}{\omega} = \frac{e_m \cos \delta}{\omega} = \frac{\sqrt{2} \cdot E_m \cos \delta}{\omega} \\
\lambda_{qm} &= \frac{(-e_{dm})}{\omega} = \frac{e_m \sin \delta}{\omega} = \frac{\sqrt{2} \cdot E_m \sin \delta}{\omega} \tag{2.13}
\end{aligned}$$

On the other hand the torque equation can be written as follows [33]:

$$\begin{aligned}
T_{em-g} &= \frac{3}{2} \frac{p}{2} (L_{dm}(i_{dm}) - L_{qm}) \cdot i_{dm} i_{qm} = \\
&= \frac{3}{2} \frac{p}{2} \left(\frac{1}{L_{qm}} - \frac{1}{L_{dm}(i_{dm})} \right) \cdot (L_{dm}(i_{dm}) \cdot i_{dm}) \cdot (L_{qm} i_{qm}) = \\
&= \frac{3}{2} \frac{p}{2} \left(\frac{1}{L_{qm}} - \frac{1}{L_{dm}(i_{dm})} \right) \cdot \lambda_{dm} \lambda_{qm} = (\text{Using eq. (2.13)}) = \\
&= \frac{3}{2} \frac{p}{2} \left(\frac{1}{L_{qm}} - \frac{1}{L_{dm}(i_{dm})} \right) \cdot \left(\frac{E_m}{\omega} \right)^2 \sin(2\delta) \tag{2.14}
\end{aligned}$$

Eq. 2.14 shows that the torque, for a certain voltage and speed condition, is maximized for $\left(\delta = \frac{\pi}{4} \right)$. Also the inductance term in this equation with an acceptable estimation is almost constant, because in nominal condition $(L_{dm} \gg L_{qm})$ and the q-axis inductance is almost constant.

The flux angle and current angle relation can be derived as follows, see Fig. 2.3:

$$\tan \delta = \frac{\lambda_{qm}}{\lambda_{dm}} = \frac{L_{qm} i_{qm}}{L_{dm}(i_{dm}) \cdot i_{dm}} = \frac{1}{\xi} \tan \theta \tag{2.15}$$

In nominal condition typically $\xi \approx 10$ for a 4 pole machine [1], therefore the maximum torque in both constant voltage and constant current operation points dictates a small flux angle (maximum: $\frac{\pi}{4}$) and large current angle (minimum: $\frac{\pi}{4}$), but the optimum point is completely related to the supply condition. For comparison of maximum achievable torque with constant current and constant voltage supply refer to Appendix A and D.

By calculating the air gap flux density (\hat{B}_1) and its angle from d-axis (load angle or flux angle), (δ) by means of FEM method, the magnetizing inductances can be calculated by the following equations [15]. A similar calculation method is used in [31]:

$$L_{md} = \frac{k_{w1} Q_s n_s}{6 p C_s} \frac{DL \hat{B}_1 \cos(\delta)}{i_{dm}} \quad (2.16)$$

$$L_{mq} = \frac{k_{w1} Q_s n_s}{6 p C_s} \frac{DL \hat{B}_1 \sin(\delta)}{i_{qm}} \quad (2.17)$$

Using the energy concept for the calculation of inductances does not give realistic results because harmonics affect the energy values where as only the fundamental air gap flux density is responsible for the torque production (average).

2.3 Magnetization characteristic

The machine main magnetization fluxes λ_{dm} & λ_{qm} characteristic generally can be expressed according to eq. 2.6. In this report it is assumed that all machine inductances except the magnetization inductances L_{dm}, L_{qm} can be modeled as constant lumped elements, i.e. stator leakage inductances in d- and q-axis are equal and constant etc. and the side effects of saturation, slotting and cross-coupling on these elements are disregarded.

Therefore the effect on total stator terminal flux, $\lambda = \lambda_d + j\lambda_q$ for the main sources of nonlinearity in SynRM, which are saturation, slotting and cross-coupling, can just be modeled by the behavior of the air gap flux linkage, $\lambda_m = \lambda_{dm} + j\lambda_{qm}$, see Fig. 2.3.

2.3.1 Saturation

Equations 2.7 and 2.12 clearly show that the direct effect of magnetization inductances on torque and power factor. These inductances are highly affected by the level of saturation in the machine core iron due to high amount of iron in both d- and q-axis flux paths.

But the saturation effect in the q-axis flux is much lower than in the d-axis, because of the insulation layers (barriers) actually cutting the q-axis flux lines so that the major responsible for saturation effect in the q-axis is the presence of the ribs in the rotor structure. Saturation effect on machine main characteristics is deeply discussed in [33, 23, 31, 29, 1, 15].

A typical saturation effect on d- and q-axis fluxes in SynRM is shown in Fig. 2.4 [28]. The rated current of the machine is 10 A. This figure shows that the saturation is normal under nominal condition in SynRM especially in d-axis.

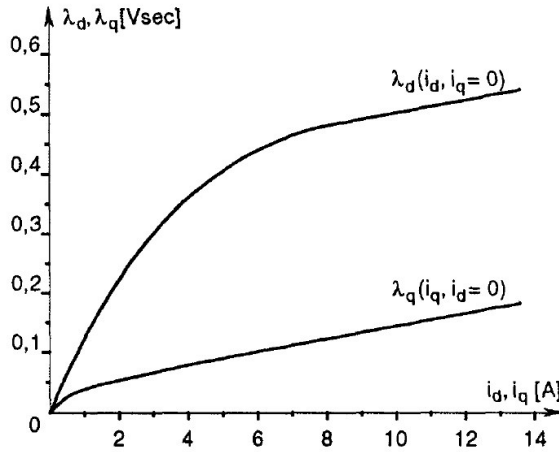


Fig. 2.4: Typical magnetizing characteristic of d- and q-axis in a SynRM with rated 10 A current [28].

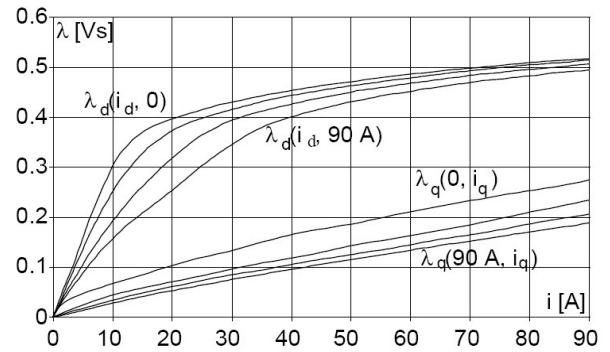


Fig. 2.5: Typical magnetizing characteristic including the cross-coupling effect of the d- and q-axis in a SynRM with 30 A rated current [1].

2.3.2 Cross-coupling

The dependency of each axis flux to another axis current in eq. 2.6 expresses another nonlinear effect in SynRM: Cross-coupling or cross-magnetization. Particularly the dependency of λ_{dm} on i_{qm} can present the well known armature-reaction effect, in other words, demagnetization of the d-axis occurs due to a large q-axis current [28]. A typical cross-coupling effect is shown for a machine with 30 A stator nominal current in Fig. 2.5 [1].

The cross-coupling effect is mainly due to the shared iron part of the rotor between d- and q-axis, also the rotor ribs increase this effect [1]. Cross-coupling also effectively reduces the q-axis flux. A typical effect of cross-coupling on machine inductances is measured and modeled in [31, 23].

Both saturation and armature-reaction effects reduce the machine torque by decreasing the d-axis inductance.

2.3.3 Slotted stator

The slotting effect in SynRM is modeled in eq. 2.6 by the dependency of magnetization inductances to rotor position ϑ . This issue is deeply discussed in [33, 41].

A schematic rotor position relative to the stator at 4 different situations is shown in Fig. 2.6 when the rotor is rotating one stator slot pitch. Considering the central segment (CS), there are two extreme situations. The first position is when the rotor is as in Fig. 2.6.a, when teeth and segments are in phase. In this case the total reluctance of the flux path that includes the CS is minimum and therefore L_d is at its maximum value. The second position is when rotor changes to the situation shown in Fig. 2.6.c, when teeth and segments are in opposition. Now the total air gap reluctance that the CS is facing is maximized and therefore L_d is at its minimum. Similar behavior for the q-axis inductances is discussed in [41]. When the rotor is in the situations that are shown in Fig.

2.6.b and 2.6.d, CS shares half of the stator teeth and slot and thus applying eg. a d-axis flux causes some q-axis flux also. This shows an interconnection effect between d- and q-axis inductances that is caused by the stator slots [41].

The change of inductances due to rotor position firstly produces torque ripple and secondly high flux fluctuation deep inside the rotor segments and consequently iron losses in the rotor body [33, 3, 43]. If the slotting effect during the rotor design stage is not attended then the iron losses in the rotor can be comparable with the rotor copper losses in an equivalent IM [43].

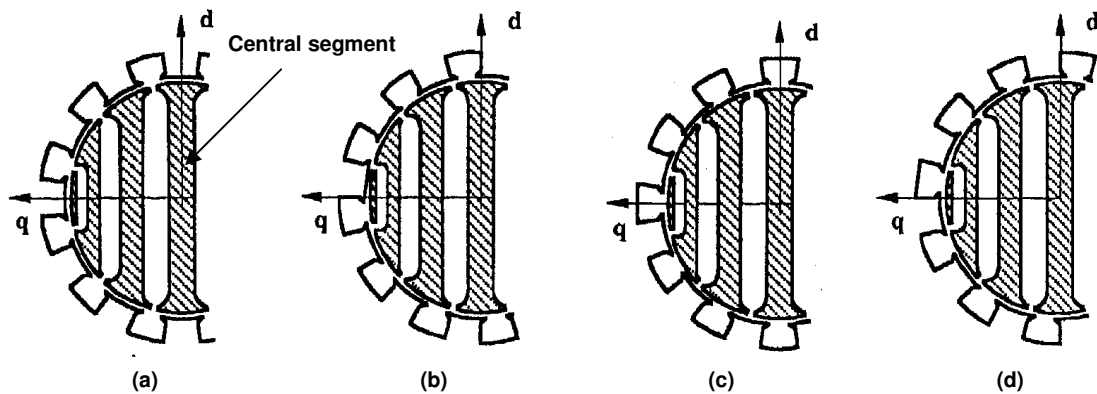


Fig. 2.6: Comparison of rotor segments position with reference to the stator teeth in four different situation when the rotor is rotating one stator slot pitch from (a) to (d) [41].

The torque ripple reduction can be achieved effectively (acceptable for traditional IM applications) by adopting the skewing technique [41]. The torque ripple can not be completely eliminated by the skewing, because, as was discussed above, at rotor positions in Fig. 2.6.b and 2.6.d there is always an interaction between the d- and q-axis fluxes due to the effects of stator slotting [28, 41].

Nevertheless rotor skewing, the rotor slot pitch has a significant contribution to the reduction of torque ripple and can therefore be used to minimize the ripple. Some design idea regarding this can be found in [33, 37, 39, 40, 44].

3 ROTOR GEOMETRY REALIZATION TECHNIQUES

3.1 Rotor geometry classification and development history

Mainly there are three different types of SynRM with anisotropic rotor structures, see Fig. 3.1. The salient pole rotor as the first possibility is made by removing some iron material from each rotor in the transversal region, see Fig. 3.1a.

In the axially laminated rotor, which is the second type of SynRM, the laminations (iron) are suitably shaped at each pole and insulated from each other using electrically and magnetically passive materials (insulation) and the resulting stacks are connected through pole holders to the central region to which the shaft is connected, see Fig. 3.1.b.

In the third type of rotor the laminations are punched in the traditional way. Thin ribs are left when punching, thus the various rotor segments are connected to each other by these ribs, Fig.3.1.c.

The SynRM does not have a starting torque characteristic, and introducing a traditional cage to the rotor structure can add an asynchronous starting torque. But by using the modern inverter technology, suitable field oriented control and PWM technique without inserting the cage to the rotor, the machine can be started from stand still.

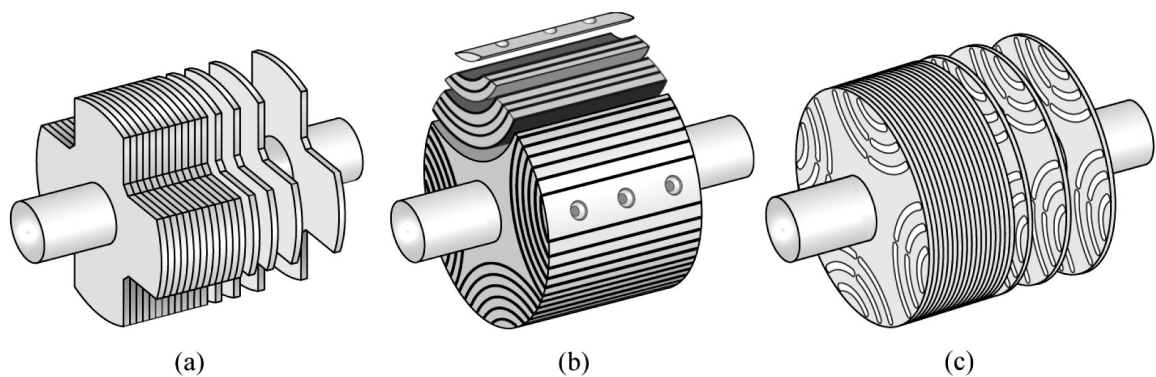


Fig. 3.1: Possible rotor design for a SynRM: (a) Simple salient pole (SP) rotor, (b) Axially laminated anisotropy (ALA) rotor, (c) Transversally laminated anisotropic (TLA) rotor [45].

A brief history of alternative rotor geometries can be useful to understand SynRM, see Fig. 3.2.

The rotor in Fig. 3.2.a is obtained by removing of material from a conventional induction motor rotor, either by a milling operation after casting the cage, or by punching before casting the cage. Rotors of this type ('synchronous induction motors') have a simple construction, but the saliency ratio is too small to give competitive performance [23, 46].

Fig. 3.2.b shows the salient pole construction, like a conventional salient pole synchronous motor with the windings removed. An unsaturated inductance ratio of about 3 has been reported for this kind of rotor decreasing to about 2.5 under load. No value of saliency ratio higher than 3.8 has been reported [23].

Despite the poor saliency ratio the other performance characteristics of salient pole geometry are also not acceptable, because, if the inter-polar space region in the q-axis is spread to reduce L_q , it also results in narrowing the pole space in the d-axis thus also reducing L_d . In this case other kind of rotor configurations, for example barrier ones must be employed to improve the machine performances [46].

A one barrier configuration, Fig. 3.2.c and Fig. 3.2.d, is also not sufficient to improve the machine performance [46]. The configuration in Fig. 3.2.d is derived from the synchronous motor with interior PM, if the PMs are removed.

Therefore the number of barriers must be increased. As early as 1923, Kostko [30] analyzed a rotor of the form of Fig. 3.2.e, see also Fig. 3.3.a, embodying several features of both the main schools of later development, including the use of multiple flux barriers, segmental geometry and a q-axis channel.

3.2 TLA and ALA comparison

As is mentioned in the last chapter the recent development in the rotor structure design is focused on two major types: TLA and ALA, see Fig. 3.4. Here an ultimate comparison between these two is investigated, which is reported in [1] and somewhat also in [28].

In practice, the better suitability of TLA structure to industrial manufacturing is evident. In this case, the rotor lamination can be punched as a whole, like for other more traditional machines. The axially laminated structure, on the other hand, is theoretically appealing, because it looks the nearest to an ideal “distributed anisotropic structure”. However, this is only true for a two-pole structure ($p = 1$), while, for $p \neq 1$, it has been shown in [47] that the ideal structure should have a variable ratio between the depths of magnetic and non-magnetic structures [1].

Moreover, the above considerations only apply to an ideal slot less stator, while the usual toothed stator structure enhances in a practical axially laminated motor both torque ripple and additional iron losses [1].

Regarding torque ripple, this is due to the rotor magnetic reaction to stator slot harmonics, as explained in [44]. Of course, a torque ripple is present also in the transverse-type of motor [41]. However, in this case the rotor can be easily skewed, while this is clearly unpractical for an axially laminated rotor. On the other hand, stator skewing is normally avoided, because it is a disadvantage when using automatic winding facility [1].

Regarding the additional iron loss in the rotor of the axially laminated type, they have been analyzed by [18] and confirmed by [27]. They can be explained in different ways. In [48] a simplified analytical model is given, valid for $p = 1$, which suggest that these losses are due to flux oscillations in the deep rotor iron due to the effect of stator teeth. On the other hand, a different explanation is given in [27], where these losses are allocated to eddy current induced in the rotor laminations by harmonic fields. Anyway, apart from the explanation, the amount of additional loss is considerable and represents a further drawback for the axially laminated type of rotor construction [1]

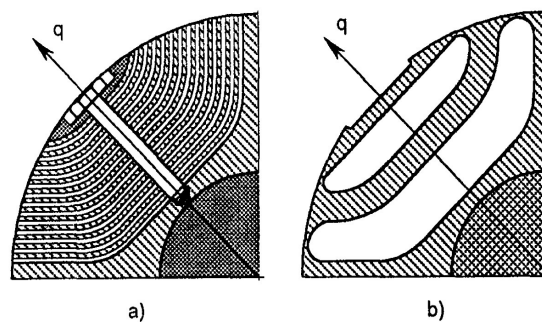


Fig. 3.4: High anisotropy rotor structures with axially (a) and transversally (b) lamination [1].

The above cited reasons are largely sufficient to choose the transverse-laminated type of rotor. However, the persistent interest on the other type is probably due to the believe that the axially laminated rotor gives a better saliency. This is not correct as comparable anisotropy values are obtained from both rotors, of course, when the pole number is the same. Ten is a typical, non saturated value for four-pole machines while it can grow up to 20, for a two-pole rotor [1].

However, the unsaturated saliency ratio clearly gives insufficient information about motor performance. This is due to both the highly nonlinear magnetic behavior and the existence of a

trade-off between rotor magnetic insulation and allowed stator MMF at fixed power dissipation [33, 2], [1].

Moreover, with reference to general purpose drives, the transverse laminated structure leads to a motor which could be even cheaper than the IM, because casting is avoided [1].

3.3 Comparison of SynRM and IM

Induction motors are the world wide most used motor in industrial and civil applications, due to its low cost, robustness and the possibility to be supplied directly from the mains, without the need for a power electronic converter. However, when the application requires speed regulation, different types of motor can be profitably adopted and parameters as torque/volume, efficiency and control easiness assume more importance [11]. A comparative definition of machine parameters for both SynRM and IM is shown in Fig. 3.5.

For the TLA type SynRM, production cost is comparable to IM and somehow it can even be cheaper due to the cage elimination in the rotor and the removal of casting stage in the production line. If the same stator size is chosen as the IM then just by changing the punching tools for the rotor geometry the SynRM can be produced with the same production line [11]. Also TLA can easily be skewed like IM for torque ripple reduction.

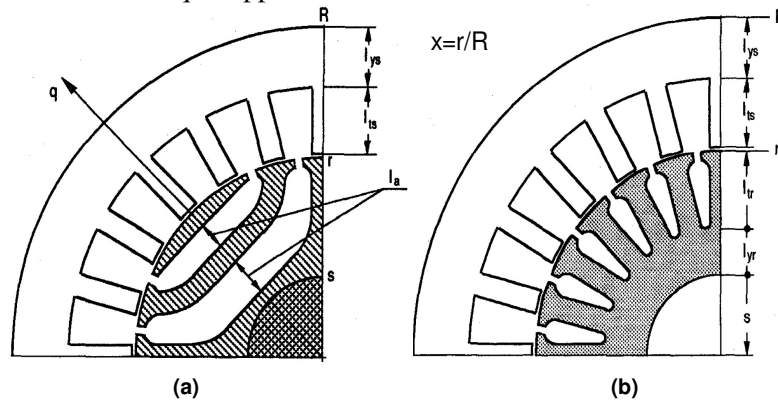


Fig. 3.5: Schematic section and comparative definition of the rotor geometric parameters for SynRM (a), and IM (b) [4].

If the stator structure and air gap diameter are kept constant for both IM and SynRM it is quite easy to compare their performances [33, 43, 28, 21].

The analysis is based on estimating torque ratio between the two machines by using some experimental values at the operating point and main machine electrical parameters [28].

In SynRM there is no cage in the rotor and consequently lower copper losses. Therefore the rated current can be increased for the same power dissipation or same temperature rise for both machines. It is shown that in this situation the SynRM can produce 20% to 40% higher torque compared to the IM. Also at the same stator current the SynRM, $\xi \approx 10$, produce about 90%-100% of the IM torque with about 50% lower total losses and consequently a higher efficiency of about 5%-8% - unit [11].

If the stator structure can be changed then the optimum machine geometry for maximum stall torque at constant loss power dissipation shows that the SynRM with the ribs always has higher torque density than IM with a copper cage [32, 4]. Also it shows that the optimum air gap to outer

diameter ratio, (x) in Fig. 3.5, for maximum stall torque is not the same in both machines. Its value for IM is around 0.6 and for SynRM it is around 0.5 see Fig. 3.6 [4].

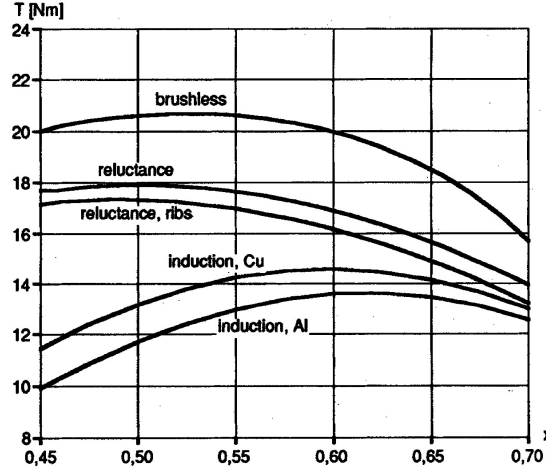


Fig. 3.6: Stall torque versus inner to outer diameter ratio (4 pole machine) at the optimum air gap flux density and same power dissipation, overall design and optimization of Fig. 3.5 geometries [4].

These analytical calculations are also verified by measurement [11, 5, 24, 16].

No copper losses in the SynRM rotor also result in cooler shaft and bearings. SynRM has higher overload (T) capacity compared to the IM and it can reach up to 3 times nominal load [1, 31]. The high saliency and anisotropic rotor can be used to adapt the sensor-less and zero speed control techniques [11].

SynRM has 5% to 10% lower power factor than IM. This is due to the combined effect of cross coupling and larger q-axis inductance. The large q-axis reactance is an inherent drawback of the SynRM. It depends on the different field distribution in the rotor and cannot be overcome. Moreover, the flux in the rotor ribs adds to this effect [11]. In practice, this drawback becomes important when a large constant power speed range is requested by the application [11, 3, 16].

In fact, the inverter oversizing which is needed in this case to cope with a fixed constant power speed range directly depends on the rated $\left(\frac{\lambda_q}{\lambda_d}\right)$ value. The larger this value is, the larger is the

inverter oversizing. However, this drawback can be overcome by introducing some permanent magnets into the rotor [11], thus changing from a TLA SynRM to a Permanent Magnet Assisted Synchronous Reluctance Motors (PM SynRM) [3, 49]. Inverter size is also related to the machine efficiency. Therefore the required inverter size can be judged by the product of efficiency and power factor $(\eta \cdot \cos \phi)$.

4 BASIC CONTROL CONCEPTS

Current angle control is straight forward and a natural way to control SynRM see eqs. 2.12 and 2.7 [33, 26, 42].

Constant torque trajectories according to eq. 2.12 are hyperbolas in current dq-plane, see Fig. 4.1. The constant voltage trajectories can be expressed according to eq. 4.1, see eq. 2.4.

This equation shows that constant voltage trajectories are ellipses as it is shown in Fig. 4.1.

$$\left(\frac{e_m}{\omega \cdot L_{qm}} \right)^2 = (i_{qm})^2 + \xi^2 \cdot (i_{dm})^2 \quad (4.1)$$

Point A is the maximum torque per current control point and B is the maximum torque per voltage or maximum rate of change of torque control point. It is clear that the terminal stator current angle must be increased to compensate the air gap flux displacement due to saturation, cross-coupling, winding leakages and iron losses see Fig. 2.3 and compare the stator flux vector λ and air gap flux vector λ_m [42].

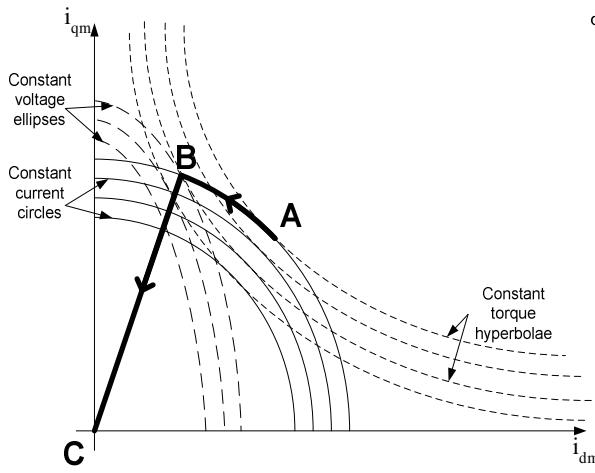


Fig. 4.1: SynRM current dq-plane and full operation trajectory (ABC) (below base speed and field-weakening ABC) [27]. Saturation is disregarded here.

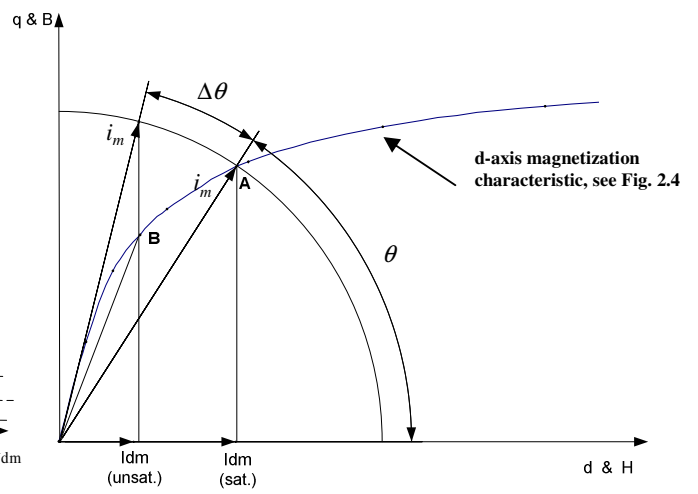


Fig. 4.2: Saturation compensation by current angle control.

Saturation, mainly in the machine d-axis, reduces L_{dm} and consequently torque for a certain current see point A in Fig. 4.2. By increasing the current angle the d-axis current is reduced to point B. Therefore the level of saturation and also air gap flux density are reduced also L_{dm} and torque are increased and compensated [42].

The iron losses require an additional angle advance to ensure optimal torque per current operation this is clearly shown in the vector diagram of Fig. 2.3. Compare the angle of stator current i_s and i_m in that figure. Because of the iron losses, i_{cs} , the effective current vector i_m is pushed back towards the d-axis by an angle. In order to have optimal torque per ampere operation, the stator current i_s needs to be adjusted to an angle that is even larger than the angle needed when saturation is considered alone [42].

To have optimal efficiency operation, an even larger increase in the current angle is required to further reduce the flux and hence the core loss. The optimum occurs when the additional copper loss associated with the increased q-axis current required to produce the torque offsets the reduction in core loss [42].

The same idea can be used to compensate the loss of effective flux λ_m due to stator leakage, see Fig. 4.3 and voltage drop over the leakage inductance.

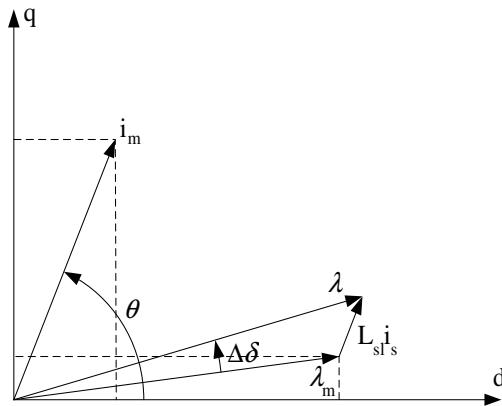


Fig. 4.3: Winding leakage effect on useful air gap flux, iron losses are neglected.

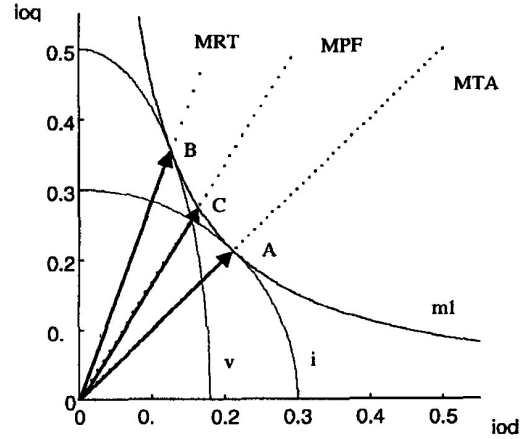


Fig. 4.4: comparison of different control strategies [26]. Saturation is disregarded in this figure.

Different strategies can be applied by current angle control, ie. a) Maximum torque per ampere (MTA), b) Maximum power factor (MPF), c) Maximum rate of change of torque (MRT), d) Constant d-axis current (CDC), e) Maximum efficiency (ME). MRT, MPF and MTA control strategies are compared in Fig. 4.4. ME control becomes important if machine iron losses become comparable to the copper losses. Otherwise MTA and ME are equivalent [26, 42, 25]

SYNRM – DESIGN ASPECTS

5 PARAMETER CLASSIFICATION AND DESCRIPTION FOR TLA-ROTOR

5.1 Design or selected parameters

To get realistic sensitivity analysis results for these parameters, macroscopic parameters, it is more efficient to examine their effect on targeted variables by FE instead of theoretical calculations.

5.1.1 Power

There are several papers, which present laboratory measurement of a prototype SynRM, for a wide power range, less than 0.2 up to 110 kW [20, 21, 13, 14, 11, 1, 7, 18, 15, 16, 19, 12, 17, 5].

Regarding the power selection, if the maximum achievable improvement of efficiency is targeted for the SynRM in comparison to the IM for the same frame size the following equation can be used for a rough estimation:

$$\Delta\eta = \frac{1}{1 + \frac{y}{x} \left(\frac{1}{\eta_i} - 1 \right)} - \eta_i \quad (5.1)$$

As a primary estimation, in eq. 5.1, y is the total losses ratio typically 0.63 and x is output power ratio = 1.00 for the SynRM over the IM, at the same speed (1500 rpm) and for the same output power, for similar comparison refer to [33, 21, 16]. This equation is demonstrated in Fig.5.1.

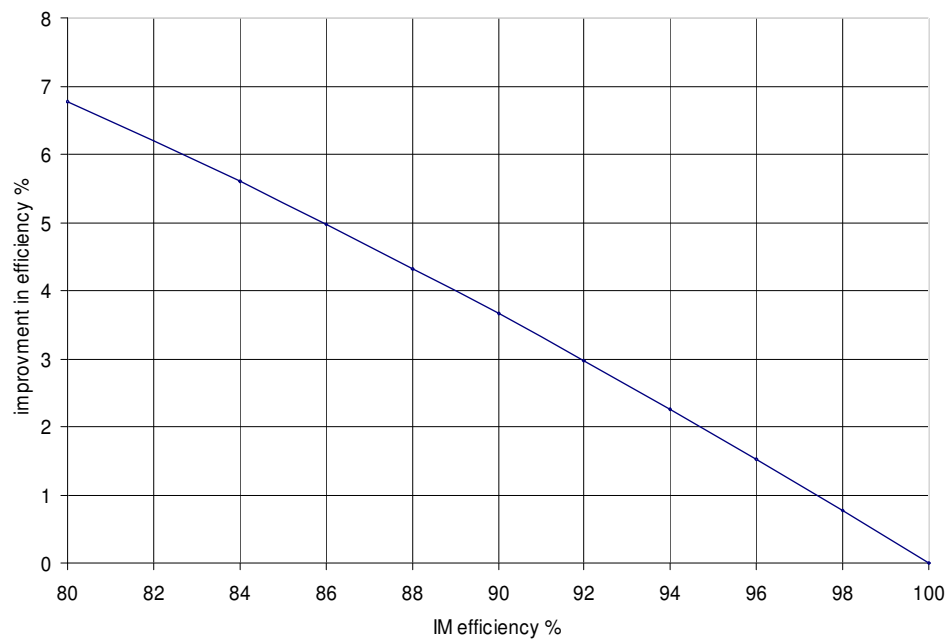


Fig. 5.1: The maximum expected efficiency improvement of a SynRM in comparison to the IM for the same size, speed and output power.

Normally the efficiency of IM increases if the nominal power increases, this graph shows that for low rated power of the IM, the SynRM can be much more efficient than the IM.

In this report a 15 kW IM, is chosen because its manufacturing volume is high, but this choice is completely related to the application. For traction application (HEV) 30 to 60 kW is suggested in many papers. This power level has been chosen and reported in [22].

5.1.2 Pole number $2p$

The pole pair number has a strong influence on the SynRM performance. A comprehensive description is given in [4] that also include the effect of pole number on the saliency ratio which will be presented here.

The anisotropic behavior of the general multiple-segment structure (TLA) is analytically treated in [2], [33]. The most important conclusions are presented below.

A d-axis sinusoidal magneto motive force (MMF) leads to an inductance (L_{md}) which is practically equivalent to the magnetizing inductance of an induction motor, for a given air gap.

A q-axis sinusoidal MMF leads to a q-axis inductance which is the sum of two terms. The term L_{cq} is related to the fluxes that circulate across the segment ends, as shown in Fig. 5.2, while the term L_{fq} is related to fluxes flowing through the segments and involving the insulation layers between segments. When ribs connecting segments are present, a rib flux must also be added. This flux is strongly limited by iron saturation.

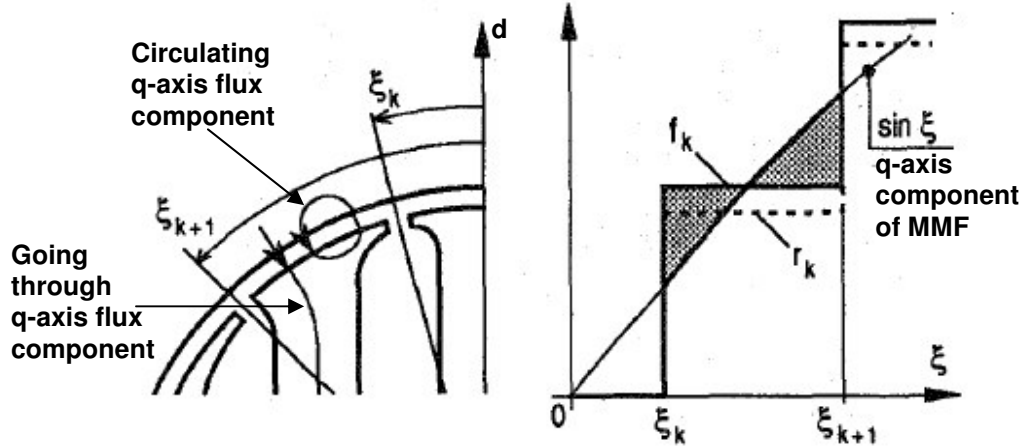


Fig. 5.2: Going through and circulating components of q-axis flux in the k -th segment and its related rotor barriers opening (slots) angular position (ξ) definitions (left) and the stator per-unit MMF excitation in the q-axis (MMF_q) and the k -th segment magnetic potential response (r_k) to the average MMF_q over the k -th segment (f_k). Circulating flux is shown by the shaded area (right) [4].

It is shown in [2] and [33] that the ratio L_{cq}/L_{md} is independent of the pole-pair number p , but decreases as the number of segments per pole-pair is increased. If each insulation layer is seen as a pair of nearly closed slots, the L_{cq} inductance is practically equivalent to the rotor zigzag inductance of an induction motor L_{zr} . Thus eq. 5.2 can be adopted [32], [10] (eq. 7.33, page 197 in [10]), where n_r is the number of rotor “slots” per pole. As can be seen, the ratio in eq. 5.2 rapidly decreases with n_r , for $n_r = 9$, L_{cq} is reduced to 1% of L_{md} .

$$\frac{L_{cq}}{L_{md}} \cong \frac{\pi^2}{12n_r^2} \quad (5.2)$$

In contrast, the ratio L_{fq}/L_{md} is practically independent of n_r , but depends on p . As a first approximation, a linear dependence on p can be supposed. Moreover, L_{fq} depends on the permeances of the various insulating layers. However, in the simple but effective case of equally spaced “slots” and uniform permeance distribution, eq. 5.3 can be used. This states that L_{fq} is inversely proportional to the internal gap l_a , measured along the q-axis, and L_{md} is inversely proportional to the air gap width g :

$$\frac{L_{fq}}{L_{md}} \cong (const.) \cdot p \frac{g}{l_a} \quad (5.3)$$

In conclusion, to obtain high anisotropy, first a sufficiently large number of rotor segments must be chosen, together with a low pole number. Then, the internal gap ‘ l_a ’ (see Fig. 5.3) should be as large as possible. Of course, ‘ l_a ’ can not be chosen freely but must be related to the choices of main flux and inner diameter.

These considerations are valid in general for both axially and transversally laminated structures. In addition, when the latter is chosen, the rib flux must be conveniently limited. Since the rib width is practically independent of ‘ p ’ while the main flux decreases with p , the choice of a low p number is once more recommended [4].

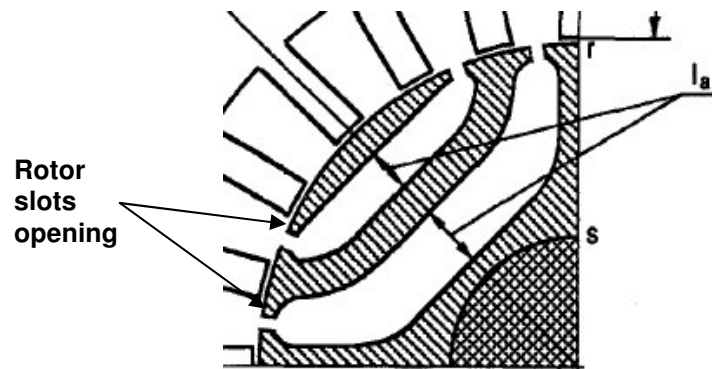


Fig. 5.3: Definition of amount of air in q-axis parameter (l_a) and rotor slot openings [4].

In this report, 2 or 3 pole pair number is suggested which is also compatible with the manufacturing of the most frequently sold product and has a high priority in this study. More analysis related to effect of p is out of the scope for this report, and it will require more investigation on the different reactances of the machines.

5.1.3 Flux barrier and segment

Field surveying of rotor flux lines [5, 30] without slots for selecting the number of segments per pole-pair is essential. That is necessary if in the final geometry, the maximum saturation in the rotor segments is required to be lower than saturation in the stator back (see Fig. 5.4 B & C and Fig. 5.6).

There is an essential rule for the design of SynRM: the rotor's slot pitch must be equal to (or multiple of) the stator's [2]. Also there is an optimum value, because the higher the number of segments, the lower becomes the rotor iron losses [3].

The segments sizes in the q-axis inside the rotor body in Fig. 5.4.A [2] and Fig. 5.5 [32] have a specific pattern; the size of the segment is reduced as the radial distance of the segment from rotor center is increased.

Putting segments inside the rotor is important to increase the d-axis inductance as much as possible. This inductance will characterize the rotor reaction to the stator MMF in the d-axis (MMFd).

In ideal condition it can be assumed that MMFd has a sinusoidal shape with a maximum in the d-axis. Therefore the amount of MMFd which each rotor segment is facing is reduced by increasing the angular distance of segment end in the air gap from the d-axis; and consequently the necessary thickness of iron in that segment is reduced.

By this assumption it is insured that the flux density in all segments are the same and iron utilization in rotor will be increased.

A straight forward assumption for segment size is that it should be proportional to the average MMFd which that segment is facing in the air gap. This MMFd reduces sinusoidally with the segment end angle in the air gap from the d-axis; therefore the segment size is also reducing sinusoidally.

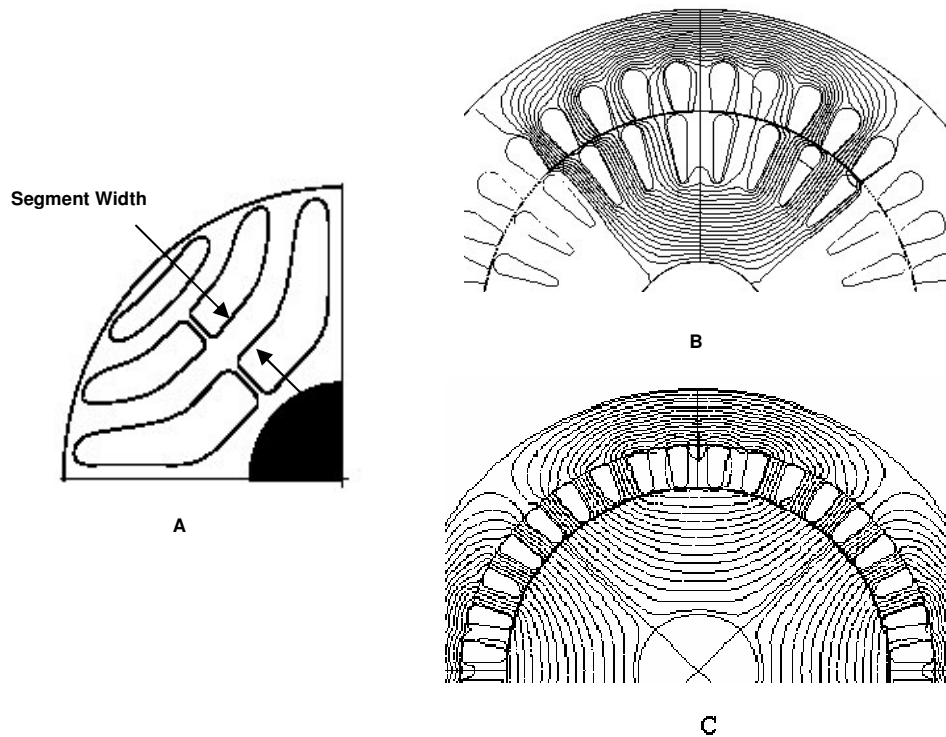


Fig. 5.4: A) Segment width [1], B) flux in standard IM rotor, C) natural flux path in rotor without any barrier.

Considering that, the number of rotor segments ideally should be as high as possible (see eq. 5.2), the motor performance will then be better [2, 3, 4]. However, from the mechanical and manufacturing point of view in order to avoid the axially laminated model, the number of segments must be limited to a reasonable value, see Fig. 5.5.

If the number of segments is limited then the circulating component of q-axis flux (see eq. 5.2) can not be reduced any more, and the improvement will be concentrated on the going through component (see eq. 5.3) of the q-axis flux. This means that the amount of air in the q-axis must be maximized (high ' l_a ') to reduce L_q as much as possible.

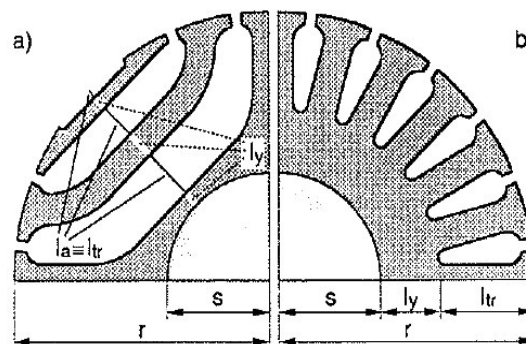


Fig. 5.5: Comparative definition of rotor parameters in a) SynRM TLA type and b) IM [32]

By keeping the segment size constant all along the segment length inside the rotor and also sinusoidally reducing the width of upper segments then for machines with more than two poles it is possible to increase ' l_a ' by increasing the barrier widths from the end toward the q-axis, see

Figs. 5.4.A and 5.5. This is possible because the total available space for both barriers and segments in the d-axis will be smaller than in the q-axis and eq. 5.3 suggests higher 'la' in the q-axis and not in the d-axis. Actually increasing air in the d-axis is not suggested because it reduces the rotor capturing capability of stator MMF and therefore the d-axis inductance.

For a specific 4 pole stator with 36 slots, which is also the case in this report, calculation of the number and width of flux barriers in the rotor shows that 2 or 4 for flux barriers plus one cut-off barrier in front of the q-axis is suitable [6, 7].

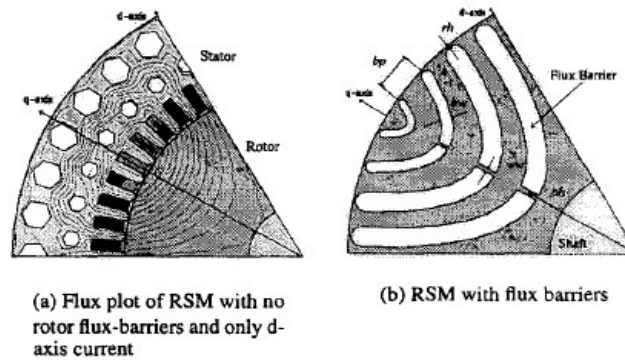


Fig. 5.6: Introduction of flux barriers in the rotor structure (b) with minimum disturbance to the main flux path in the rotor (a) [5].

This fact can be explained with reference to Fig. 5.4.C. If the rotor slot pitch is considered to be equal to the stator slot pitch, it clear that the number of active stator teeth in the flux path is 4 teeth per half pole, which is equivalent to 3 flux barriers plus one cut-off barrier. Fig. 5.7.b also demonstrates such conditions for a two pole machine with 2 stator slots per pole per phase which has 3 stator active teeth in the flux path [2].

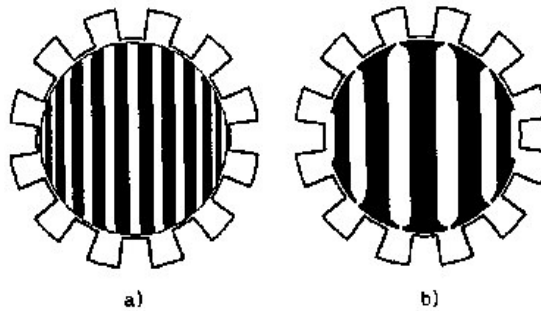


Fig. 5.7: Segmenting rotor proportional to stator active teeth number in the main flux path (b) which is equivalent to 2 barriers and one cut-off [2]. These are also suggested designs to reduce the rotor iron losses in the rotor specially (a) [2].

Surveying IM rotor structure as it has been optimized through years it has been found that the best number of rotor slots for a 36 slots stator is 28. this is shown in Fig. 5.8.A. From air gap point of view it is obvious that, the optimum number of rotor slots for maximum utilization of the magnetic circuit with minimum distortion of the natural field path inside the rotor and also for reduction of torque ripple is 7.

Using this concept for SynRM and introducing barriers: 1 proportional to rotor slot 1, 2 proportional to rotor slots 2 & 3, 3 proportional to rotor slots 4 & 5, 4 proportional to rotor slots 6 & 7, will result in a SynRM rotor geometry as shown in Fig. 5.8.B.

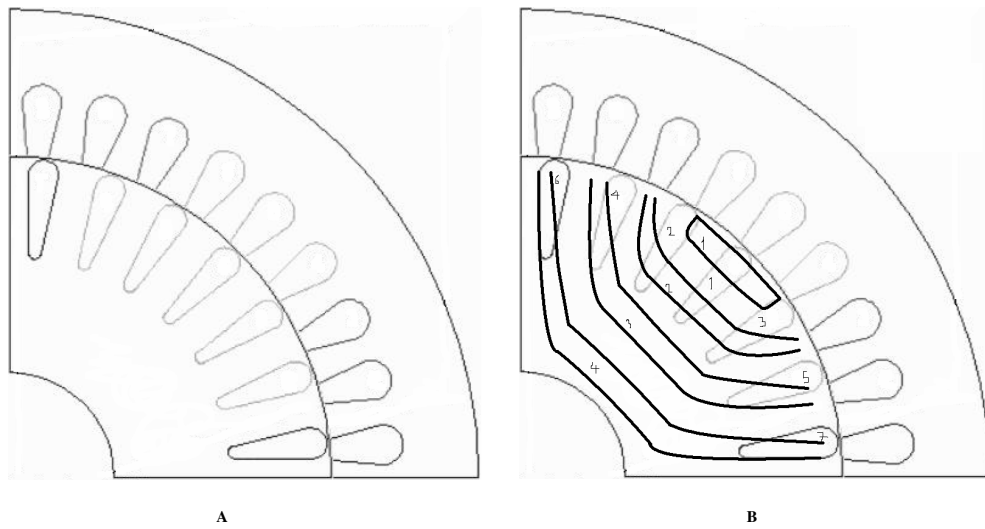


Fig. 5.8: IM rotor slots number: A, and related SynRM barriers: B.

Of course for IM, internal barriers are not necessary, because the current in rotor bars will force the flux pass through the rotor internal body as it is shown in Fig. 5.4.B. But for SynRM they are necessary, because of the absence of the rotor current.

The main idea is that the IM is also a kind of SynRM, because when rotor bars have current then from air gap point of view the rotor is electro-magnetically acting like an anisotropic structure and it is letting the flux pass smoothly along one axis and blocking the flux along the other axis.

Again a rotor slots pitch for SynRM equal to or multiple of stator slots pitch is emphasized, which means 2 or 4 barriers for a 36 slot stator.

Effect of $[N_L]$, the number of layers per pole (laminations + barriers), on L_d & L_q for a machine with 3 slots per pole per phase, is demonstrated in Fig. 5.9 [23].

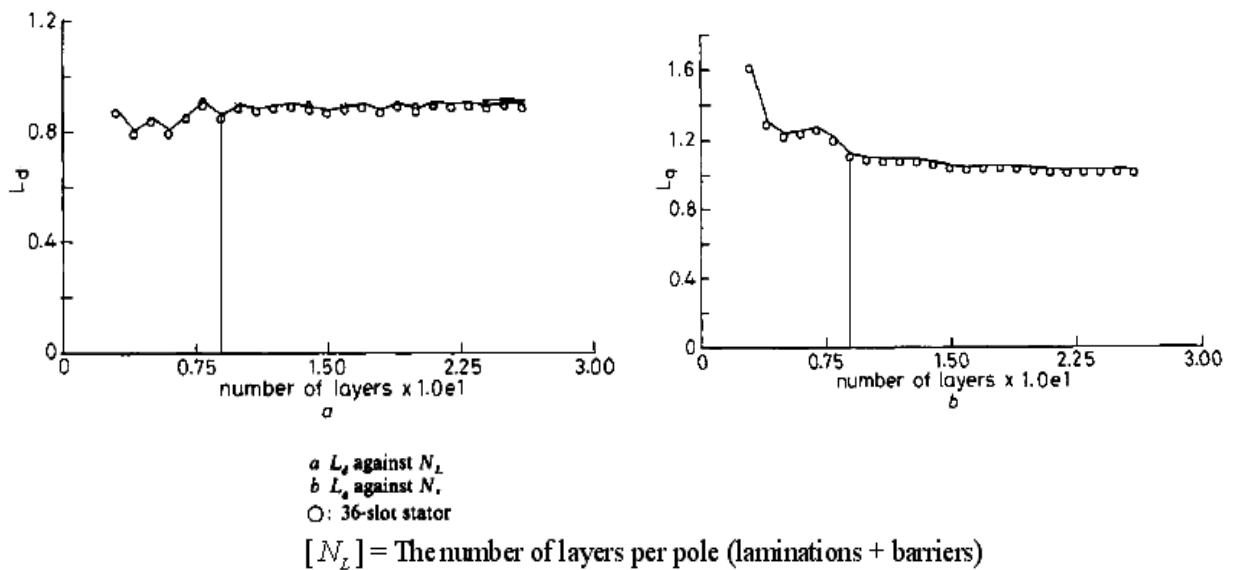


Fig. 5.9: Typical behavior of L_d and L_q with changing N_L [23]. In the figure $1.0e1$ is equal to 10, also L_d values must be multiplied by 100 and L_q values by 10 to get the inductances in mH.

Actually for $N_L > 8$, increasing the number of barrier, have little effect on machine inductances. Fig. 5.9 shows that 4 is a suitable number of barriers for this stator. Furthermore, varying N_L has little effect on L_d , But has a big influence on L_q if $N_L < 3$. For $N_L > 10$ L_q is almost unaffected.

5.1.4 Rotor barrier Insulation ratio

For purposes of comparison between different geometries and to have another criterion to judge between different designs and also for final tuning of the primary designs, it is useful to define the ratio:

$$K_w = \frac{W_{ins}}{W_{iron}} \quad (5.4)$$

W_{ins} - the sum of the widths of the flux *barrier* layers

W_{iron} - the sum of the widths of iron layers (*Segments* - flux guides)

Clearly, when $K_w = 0$, the rotor is assumed to be completely made of iron, (i.e., no saliency). When $K_w = 1$ the rotor is constructed of lamination segments in which the air space and lamination segments are equal [29, 12].

Normally this definition is used, when the subject is the ALA type of SynRM, but with the following discussion, it will be shown, that it is also a good tool for tuning the barrier shape near the air gap, and also for maximizing the iron utilization in the rotor body and increasing the barrier width in the q-axis.

If the minimum insulation ratio in the rotor near the air gap is assumed to be equal to that in the stator k_{wg} and the insulation ratio in the q-axis k_{wq} , the maximum total required segment thickness in the q-axis is, see Fig. 5.10:

$$W_{sq} = \frac{l \cdot k}{(1 + k_{wg})} \quad (5.5)$$

Where (k) is MMF factor and (l) is the half of one pole length in the air gap, and:

$$k_{wq} = \frac{\frac{D}{2} - \frac{DRI}{2} - W_{sq}}{W_{sq}} \quad (5.6)$$

For stator of the machine which is being studied in this report $k_{wg} \approx \frac{BSS_1}{BTS_1} = \frac{6.5}{7.99} = 0.81$. Using

the above equations gives $k_{wq} = 0.96$ ($k=0.8$ is related to air gap MMF distribution and number of active stator teeth in the main flux path). Increasing the insulation ratio in the q-axis effectively will reduce L_q .

Fig. 5.11 shows the flux density in different part of a machine that has constant barrier width rotor design. Because of the high insulation ratio near the air gap some stator teeth are blocked with rotor barriers and this reduced the flux densities effectively in some stator teeth, specially in the second and forth stators teeth (marked with a white circle). For modification a K_{wg} (insulation ratio near the air gap) reduction for the rotor is necessary.

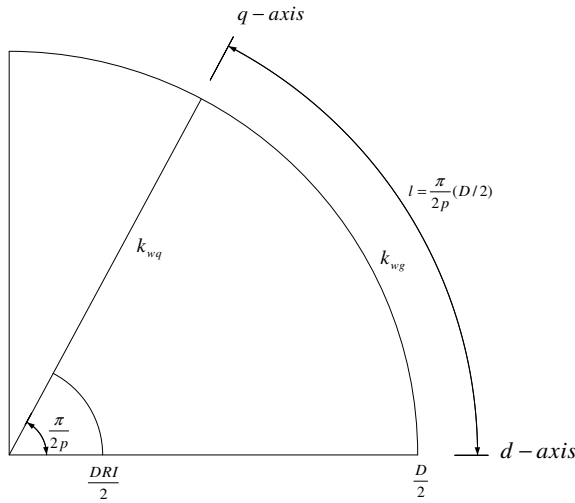


Fig. 5.10: Half pole overall geometry schematic for a p pole-pair machine.

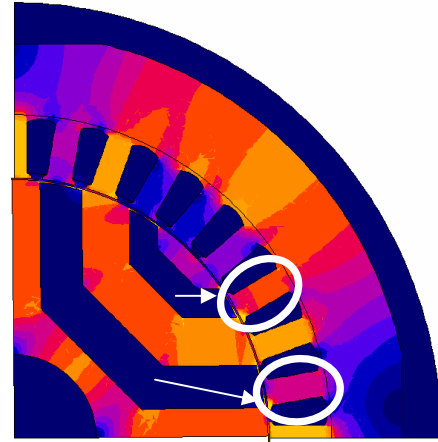


Fig. 5.11: Primary design without modification regarding the insulation ratio near the air gap.

Insulation ratio has been studied in different papers [29, 12, 23, and 30]. In Fig. 5.12 the normalized inductances (with respect to their values when $K_w=0$), are shown [29]. Fig. 5.12 presents the typical effect of insulation ratio on torque, which is proportional to (L_d-L_q) , a value between 0.2-0.6 seems to be an optimum value for the average insulation ratio in the rotor.

Fig. 5.12 shows that introducing air to a solid rotor especially in the q-axis does not have a significant effect on L_d , but L_q is highly affected (see also [30]). Actually in order to have a high reluctance saliency and a high reluctance difference, the main aim is to find an optimum value for L_q without highly disturbing L_d .

A general rough rule for a primary design (max. torque) of rotor structure is evident from the claim in the last paragraph, this should be combined with the knowledge that the number of segments must be as high as possible, of course taking mechanical limits into considered:

Firstly decide on the number of barriers per pole (normally higher than the number of stator slots per pole per phase, q), then secondly define an insulation ratio especially in the q-axis, and finally, by using some simple finite-element method try to find best insulation ratio in the q-axis. Such kind of design procedure is used in [15, 16, 36, 33 (Lipo, Miller and Boldea), 23 and somewhat in 12] and all ALA type designs.

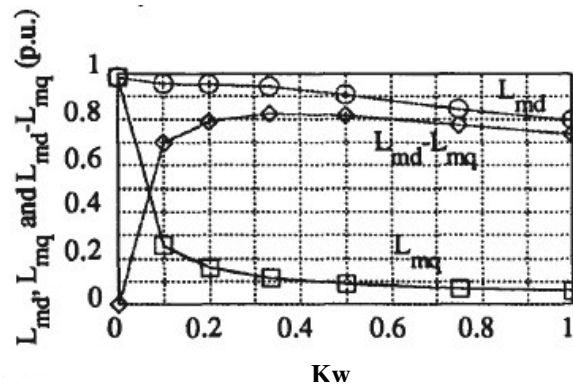


Fig. 5.12: L_{md} , L_{mq} and $(L_{md}-L_{mq})$ vs. K_w resulting from the finite-element study of a SynRM with 24 stator slots [29, 33].

Actually the shape and position of the barriers in the rotor has a small effect, if maximum torque is targeted.

5.1.5 Tangential and radial ribs

Certainly the rotor structure of Fig. 5.11 is not mechanically self-sustained. Somehow the rotor segments must be interconnected to each other. One way is to introduce radial ribs in the q-axis and tangential ribs near the air gap, see Fig. 5.13. These ribs will be saturated by q-axis MMF, during normal operation. And therefore disconnect the different segments from each other from the magnetic potential point of view.

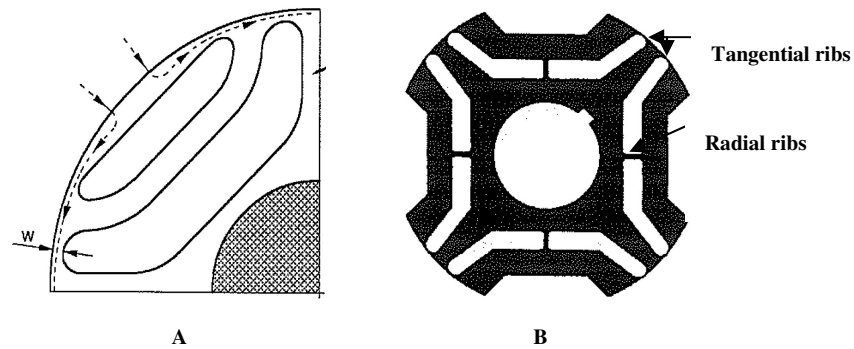


Fig. 5.13: Tangential and radial ribs in the rotor structure [31, 32], A) The additional q-axis flux required, to saturate the ribs. B) Definition of two different ribs.

The approximate effect of introducing ribs based on figure (A) above is presented in [2, 32, 33, 34], based on the extra flux (λ_r) needed to saturate the ribs at $B_s=2T$. This directly causes a torque reduction, which can be estimated by eq. (5.7) [2].

$$\Delta T = \frac{3}{2} p \lambda_r i_d = \frac{4}{\mu_0} (w l B_s) p^2 B_d (k_c g k_s) \quad (5.7)$$

It is clear that this torque loss is proportional to p^2 and the rib width w which is of course dependent on the mechanical limit. The effect of radial rib width on machine (see Fig. 5.13.B) inductances is presented in [31], and is shown in Fig. 5.14.

The effect of this flux loss in the q-axis is much more complex, see also [34]. This can be explained by Fig. 5.14 as, increasing the rib width will change both L_d and L_q equally $\Delta L_q \approx \Delta L_d$. However the relative change compare to the base values is much greater for the inductance in the q-axis than in the d-axis. Actually the L_d reduction is caused by the increase of the effect of the q-axis cross-magnetization on the d-axis [31] and not directly by increasing the rib width. The current in the q-axis is normally greater than in the d-axis, this means that $\Delta \lambda_{qr} \gg \Delta \lambda_{dr}$, due to the introduction of the ribs. It is reasonable to assume that $\Delta \lambda_r \equiv \Delta \lambda_{qr}$ and $\Delta \lambda_{dr} \approx 0$.

Torque (which is proportional to $(L_d - L_q)$) reduction is direct proportionality with the rib width which is evidential from both eq. 5.7 and the finite-element analysis results shown in Fig. 5.14.

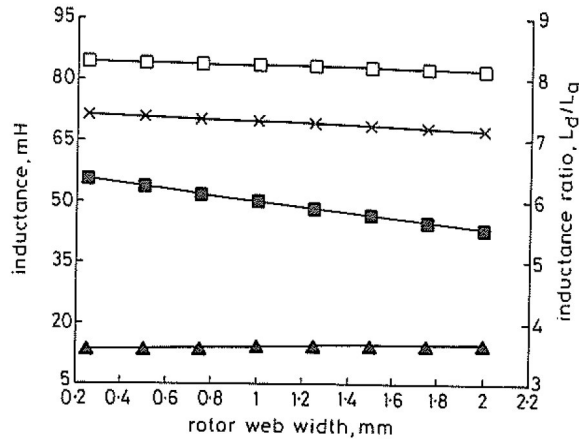


Fig. 5.14: [31],

(web = rib)

Effect of web width on inductances of RSM

 $I_d = 10$ A; $I_q = 17.4$ A; actual web width = 2.0 mm

$\square-\square$ L_d
 $\times-\times$ $L_d - L_q$
 $\blacksquare-\blacksquare$ L_d/L_q
 $\blacktriangle-\blacktriangle$ L_q

5.1.6 Air gap length

The air gap length 'g' has a considerable effect on the d-axis inductance L_d , but no effect on the q-axis inductance L_q . Result from a study is presented in [31], which is shown in Fig. 5.15. This figure shows that 'g' must be kept as low as possible, in order to increase the torque only limited by mechanical considerations. If the torque ripple is considered this 'g' reduction will increase the torque ripple (also the iron losses), because of the increase in the Carter's factor but, this is general for all slotted stators. With this situation circulating flux at the end of segment is also increasing.

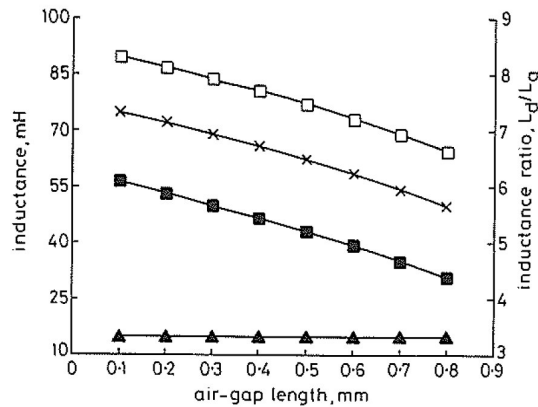


Fig. 5.15: [31],

Effect of air-gap length on inductances of RSM

 $I_d = 10$ A; $I_q = 17.4$ A; actual air-gap length = 0.35 mm

$\square-\square$ L_d
 $\times-\times$ $L_d - L_q$
 $\blacksquare-\blacksquare$ L_d/L_q
 $\blacktriangle-\blacktriangle$ L_q

The fact that L_q is not affected by the change in the air gap length can be explained by the positive effect of d-axis cross-magnetization on the q-axis inductance and the different nature of L_d and L_q .

Generally the d-axis inductance is inversely proportional to 'g', total air gap that the d-axis flux is crossing, and L_q is inversely proportional to '(la+g)', total air gap that the q-axis flux is crossing. As (la>>g) L_d is much more sensitive to air gap changes than L_q . This subject is widely explained in [20, 23] and somewhat also in [33].

5.2 Design variables

Based on design parameters a simple theory can be used to determine the best final geometry by using some intermediate design variables or microscopic parameters.

5.2.1 Position and Size of barriers

The basic goal is to find a suitable procedure for positioning and sizing the flux barriers in the rotor body for a selected number of barriers and insulation ratios. The criteria here is to reach maximum anisotropy and best rotor design, in order to obtain optimal performance values of torque, power factor, torque ripple and efficiency. This is a difficult task at first view, because there are a lot of geometrical parameters, each one of which introduces a degree of freedom in designing of the rotor structure. Such parameters are defined in Fig. 5.16. It is obvious that if another barrier is introduced in the rotor the number of combinations will be doubled.

Directly working with just geometrical parameters is a time consuming process which is not supported by any electromagnetically based theory. Such kind of analysis finally breaks down to the solution of the problem of finding suitable mathematically based optimization strategies. Most of these solutions present a time consuming procedure combining some kind of finite-element calculation with mathematical optimization algorithm. For some examples related to this issue refer to [7, 8, 18 and 35].

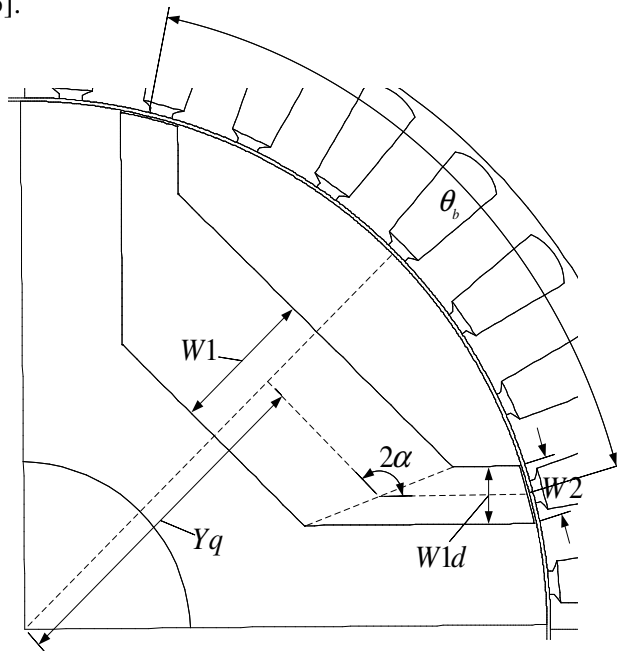


Fig. 5.16: One Barrier involving geometrical parameters.

It is clear that by using finite-element calculation it is possible to overcome the nonlinearity nature of the problem, especially saturation, but mathematical optimization can be avoided.

For this purpose a theoretical behavior explanation (qualitative and parametric) is necessary. After that a translation between geometric parameters and theory and vice versa is needed.

Fortunately, for the first time, in 1923 a theoretical analysis of a possible anisotropic rotor structure and its behavior has been presented by: J. K. Kostko [30] and his works developed by A.

Vagati during 1980s and 1990s, [33, 34, 32, 2] also [31]. The main ideas of these works are presented here.

5.2.2 Basic theory of a transversally laminated anisotropic rotor (Barriers sizing)

Here it is assumed that the stator of SynRM and IM are the same. This assumption is not valid if someone is looking for the best SynRM performance which will require an overall review of the rotor and stator structure design. But the same concepts can be used for a general approach theory [2].

It has been shown that for the same outer diameter for both SynRM and IM the best inner diameter will be chosen to achieve the main goal (max. of: PF, T/Amp ...) [18] and will depend on the machine type. But roughly for maximum stall torque the inner diameter needed for a SynRM is smaller than for an IM for the same ohmic power dissipation [4, 32, 18 and chapter 2].

Some of these basic concepts have been used in the last chapters' discussion, especially ch. 5.1.2, 5.1.3 and 5.1.5.

For simplicity saturation, stator slotting, iron potential drop, unperfect stator winding and MMF distribution effects are disregarded without any major loss in the theory's generality [30].

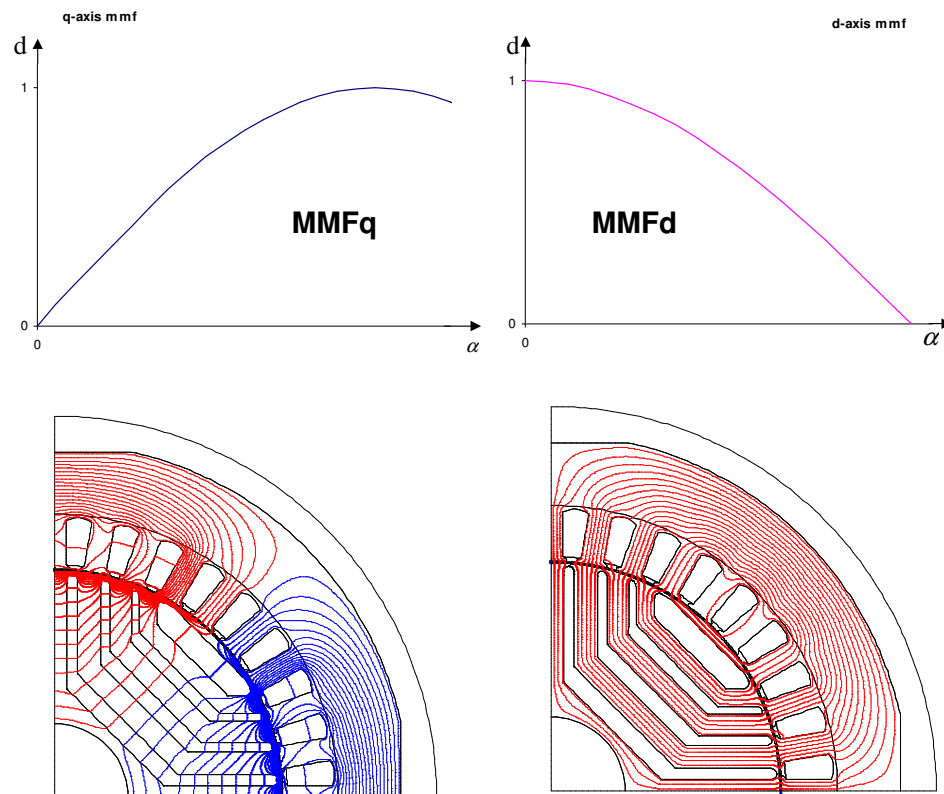


Fig. 5.17: The d & q-axis fundamental components of the air gap MMF(p.u.) and their corresponding flux distribution.

Any stator air gap MMF in synchronous reference frame from the rotor point of view has two components in the d-axis (where the rotor has minimum reluctance) and the q-axis (where the rotor has maximum reluctance), see Fig. 5.17.

Generally, the rotor structure must satisfy the following requirements [33]:

- The direct-axis flux has to flow across the whole pole surface in order to obtain a large magnetizing inductance.
- The quadrature-axis flux needs to be minimized in order to get a low L_q .

Using these two rules simultaneously leads to a segmented rotor with a high number of segments. These segments are oriented in the d-axis flux direction to minimize the d-axis reluctance, and perpendicular to the q-axis flux path. The amount of air along the q-axis flux path and the reluctance in the q direction are thus maximized.

When only a d-axis component (MMFd) is applied, the rotor magnetic potential and reaction is zero. However, if a q-axis component (MMFq) is applied, the rotor magnetically reacts and each segment gets a different magnetic potential; the central segment potential due to symmetry is always zero [33]. See also chapter 5.1.2.

Schematically, the situation is shown in Fig. 5.18. As was mentioned in the last chapter the q-axis MMFq caused two kinds of fluxes. One part of the flux flows through the segment, and the other part circulates across each segment end, the circulating flux is represented in Fig. 5.18 (right) by the shaded areas. For more details refer to [33].

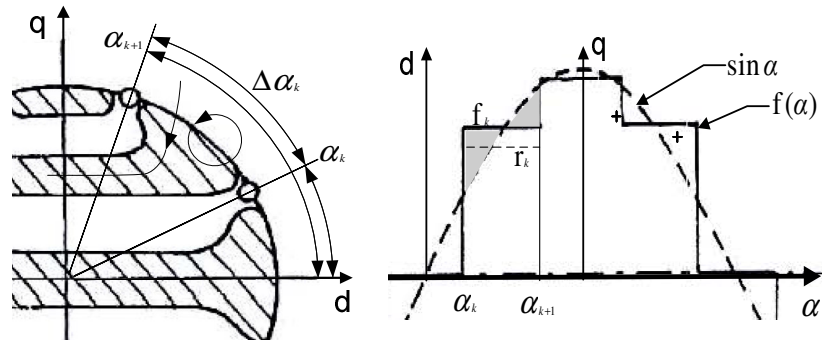


Fig. 5.18: The k-th segment air gap position parameters (left) and its related p.u. potentials reaction due to the q-axis p.u. component of MMF ($\sin \alpha$) [33, 37].

By using the following simple definition of the p.u. MMFq over the k-th segment:

$$f_k = \frac{1}{\Delta \alpha_k} \int_{\alpha_k}^{\alpha_{k+1}} \sin \alpha \cdot d\alpha = \frac{\cos \alpha_k - \cos \alpha_{k+1}}{\alpha_{k+1} - \alpha_k} \quad , \quad (5.8)$$

and with some simple calculations [30, 33], the related flow through and circulating flux inductances ratios can be calculated. For circulating inductance the equation below [33] can be derived (compare with eq. 5.2):

$$\frac{L_{cq}}{L_{md}} = 1 - \frac{4}{\pi} \sum_k f_k^2 \cdot \Delta \alpha_k \quad , \quad (5.9.1)$$

and for the flow through inductance ratio [33] (see also [30]):

$$\frac{L_{fq}}{L_{md}} = \frac{4}{\pi} \sum_k f_k \cdot (f_k - r_k) \cdot \Delta \alpha_k \quad (5.9.2)$$

Using eq. 5.9.1 is straight forward (for some examples refer to [33]), but for eq. 5.9.2 some geometric parameters related to the k-th segment are needed to calculate r_k . Referring to Fig. 5.19, which shows the equivalent circuit of the k-th segment and by some mathematical manipulations eq. 5.9.2 can be rewritten as a function of barrier dimensions [33].

$$\frac{L_{fq}}{L_{md}} = \frac{4}{\pi} \left(\frac{p}{2} \frac{g}{(D/2)} \right) \cdot \sum_k (p_k \cdot \Delta f_k^2) \quad \text{where} \quad p_k = \frac{S_{bk}}{W1_k} \quad (5.9.3)$$

As the end points of barriers in the air gap were defined before, and consequently α_k is constant or selected, S_{bk} values will be constant and the main degree of freedom will be the dimensions of the barriers width $W1_k$, see Fig. 5.19. The total amount of air in the q-axis is defined by 'la' (see Fig. 5.3).

$$la = \sum_k W1_k \quad (5.10)$$

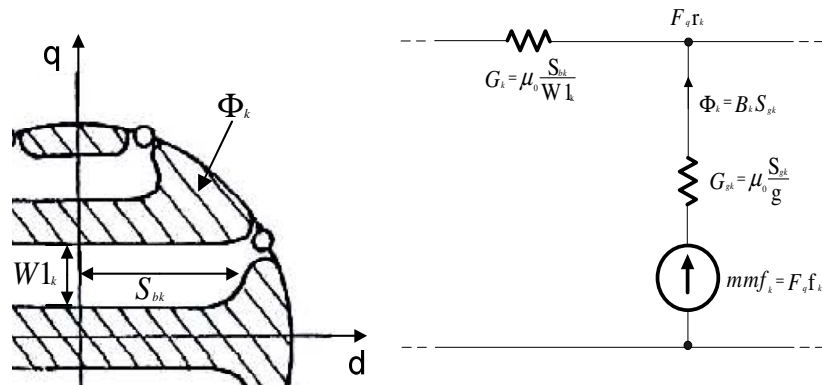


Fig. 5.19: Equivalent circuit of the k-th segment (ideal) for the q-axis excitation [33], where (F_q) is the q-axis MMF, (B_k) is the average air gap flux density over the k-th segment, (S_{gk}) is the air gap tangential length over the k-th segment.

Minimizing eq. 5.9.3 with respect to eq. 5.10 will give for the h-th and the k-th rotor barriers [33]:

$$\frac{W1_k}{W1_h} = \frac{\Delta f_k}{\Delta f_h} \sqrt{\frac{S_{bk}}{S_{bh}}} \quad , \quad (5.11)$$

and related minimum inductance ratio becomes [33] (compare with eq. 5.3):

$$\left. \frac{L_{fq}}{L_{md}} \right|_{\min.} \cong \frac{4}{\pi} \left(\frac{p}{2} \frac{k_c g}{la} \right) \cdot \left(\sum_k \Delta f_k \cdot \sqrt{\frac{S_{bk}}{(D/2)}} \right)^2 \quad (5.9.4)$$

Rotor segment k-th p.u. MMFd, responsible for the going through component of the segment flux, which is part of the applied d-axis MMF is shown in Fig. 5.21 in such a situation.

One simple rule for dimensioning the segments can be based on the amount of MMFd that is flowing through each segment (MMFdk). This will guarantee an almost constant flux density in all segments. It will also increase the iron utilization in the rotor and reduce the non-uniformity of the saturation level in the segments.

For maximizing the captured MMF by each segment it is clear that this rule can not be followed close to the end points, and the segments near the air gap must be disconnected from each other just by a small opening or rib. But for segment widths in the q-axis and all along the segment except for 10% of the length near the ends, the width can be assumed to be proportional to MMFdk, see Fig. 5.21.

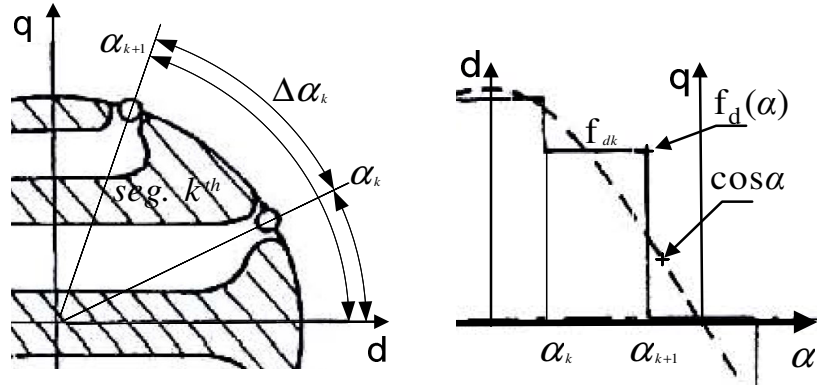


Fig. 5.21: The k-th segment and its related p.u. applied d-axis MMF.

Therefore a simple segment dimensioning rule for the k-th and h-th segments can be written as the equation below:

$$\frac{S_k}{S_h} = \frac{f_{dk}}{f_{dh}} \quad (5.14)$$

Where S_k is the segment width in the q-axis and f_{dk} is the average p.u. MMF which is going through the k-th segment and can be calculated as:

$$f_{dk} = \frac{1}{\Delta \alpha_k} \int_{\alpha_k}^{\alpha_{k+1}} \cos \alpha \cdot d\alpha = \frac{\sin \alpha_{k+1} - \sin \alpha_k}{\alpha_{k+1} - \alpha_k} \quad (5.15)$$

Barrier positioning at last in the q-axis can be derived from the segments and barriers widths for a certain number of barriers and insulation ratio in the q-axis (k_{wq}).

Positioning the end points if the general rules are followed for sizing the segment and barriers and also almost fixing the end angles is not a difficult task at this stage. A suitable procedure will be explained in details in the next chapters.

Using a simple theory the geometrical parameters in Fig. 5.16 can be replaced by general, significant and expressive parameters like the design parameters described in the last chapters. These parameters are for example insulation ratio, barrier number, end points position. This also makes it possible to avoid directly dealing with geometric dimensions.

5.3 Target variables

Every optimization and sensitivity analysis targets some goals with respect to the input parameters this is also true for SynRM. There are some geometrical parameters that can be varied and it is interesting to investigate the effect of these parameters on common target variables such as torque, power factor, torque ripple, efficiency and generally the machine performance.

In SynRM another important issue is that the optimum value for target variables can be achieved by both machine design and closed loop control, for example compare [31] with [25, 26].

5.3.1 Torque per stator current and Efficiency

For any kind of machine two important design characteristics are torque/Amp capability and efficiency. In the SynRM torque is expressed by the equation below:

$$T = \frac{3}{2} \frac{p}{2} (L_d - L_q) \cdot i_d i_q = \frac{3}{2} \frac{p}{2} (L_d - L_q) \cdot I_s^2 \cdot \sin(2\theta) \quad (5.16)$$

Where (p) is the pole numbers, (I_s) is the stator rms current, and (θ) is the current angle. On the other hand if iron losses are disregarded (low speed), efficiency can be obtain according to [18]:

$$\eta = \left(1 + \frac{P_{loss}}{\omega_r \cdot T} \right)^{-1} \quad (5.17)$$

And for losses:

$$P_{loss} \approx P_{cu} = 3R_s I_s^2 \quad (5.18)$$

Introducing eq. (5.18) to (5.17) gives:

$$\eta \approx \left(1 + \frac{1}{\frac{\omega_r}{3 \cdot R_s} \cdot \left(\frac{T}{I_s^2} \right)} \right)^{-1} \quad (5.19)$$

The above equations clearly show that maximizing T/Is is equivalent to maximize the efficiency if iron and stray losses are neglected compared to copper losses. Thus eq. 5.18 becomes valid.

This condition situation is almost true for low speed but for high speeds it is not correct. Also normally high torque ripple due to poor design, affect the efficiency by increasing the torque ripple and consequently the iron losses [3, 33] but it does not affect the average torque [33]. Actually iron losses are strongly dependent on flux fluctuation in the iron and therefore on the torque ripple.

On the other hand eq 5.16 shows maximizing T/Amp is directly related to the $(L_d - L_q)$ maximization, and consequently some geometrical parameters become involved [31].

However, the geometrical parameters that affect the losses and efficiency could be different from those involved in torque, in other words optimum point for torque can be different from optimum point for efficiency. For more discussion regarding the effect of iron losses on the geometry design refer to [3, 25, 26].

5.3.2 Iron losses and torque ripple

5.3.2.1 Iron losses (total)

Iron losses can be divided into the hysteresis losses (first term in eq. 5.20), the classical eddy current losses or Joule losses (second term in eq. 5.20) and the excess losses or high frequency hysteresis losses (third term in eq. 5.20).

For each flux density harmonic in a semi-point area (flux density is assumed to be constant at all points in that area) the total iron losses density, W/Kg is given by:

$$dP_{tot} = k_h B_{0m}^2 f_0 + \pi^2 \frac{d^2 \sigma}{6} (B_m^h(hf_1))^2 + k_e (B_m^h(hf_1))^{3/2} \quad (5.20)$$

Where (B_{0m}) is the maximum value of hysteresis curve flux density in a particular area with frequency (f_0) and (B_m^h) is the h-th order harmonic with frequency (hf_1) , (σ) is the conductivity, (d) the lamination sheet thickness, (k_h) the coefficient of hysteresis loss and (k_e) the coefficient of excess loss. Total iron losses are the sum of all the harmonics iron losses.

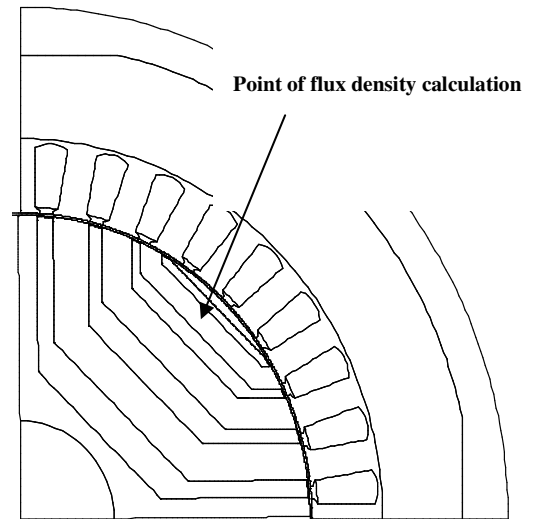
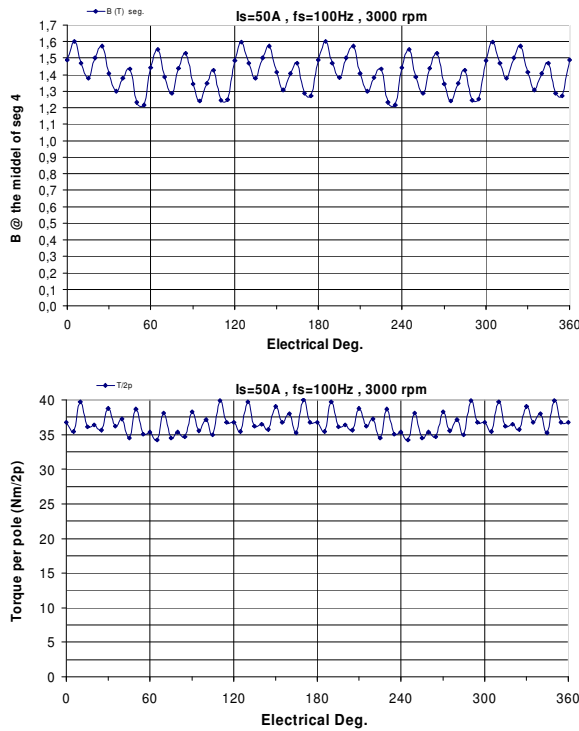


Fig. 5.22: Air gap torque (left-bottom) and flux density (left-top) at a point in the middle of segment 4 (right), variations over one electrical period. Finite element calculation was done just at 73 points which is quite low.

If torque harmonics of different barriers in the air gap do not eliminate each other (for more details related to harmonics elimination techniques refer to [39, 40]), it is roughly correct to assume that the torque harmonics amplitude are directly proportional to the flux harmonics when pure sinusoidal current is applied. Depending on the type of motor control, current or flux ripple will produce torque ripple [33] and iron losses. Due to torque harmonic elimination it can be claimed that minimum flux harmonics content are those that also exist in torque and $B_m^h \propto T_m^h$, see Fig. 5.22. Such condition takes place if the machine is skewed.

Fig. 5.23 shows that factor $T_m^h \cdot (hf_1)$, (harmonic amplitude x harmonic frequency) spectrum, from a finite-element (350 point/period) modeling for a SynRM supplied by constant current source. The air gap space harmonic due to the stator slots, and the belt harmonics (order: $6h$; $h=1, 2, 3, \dots$) will be the most dominating harmonics [33].

This shows that the iron losses according to eq. 5.20 for high order slot harmonic could be as high as for the low order harmonics. More study is needed to investigate the exact effect.

In a SynRM rotor it is expected that the flux density inside the rotor should be a constant due to synchronism, but there are two different effects that cause flux density disturbances [33], and consequently increase the iron losses inside the rotor. One is the space harmonic due to the slotted air gap, and the second is directly related to the rotor structure which due to its anisotropic nature interacts with the slotted air gap [33].

In a SynRM the rotor segments must periodically loose their flux when passing in front of the stator slot. The flux of one segment must be transferred to adjacent segment in a *very short time*.

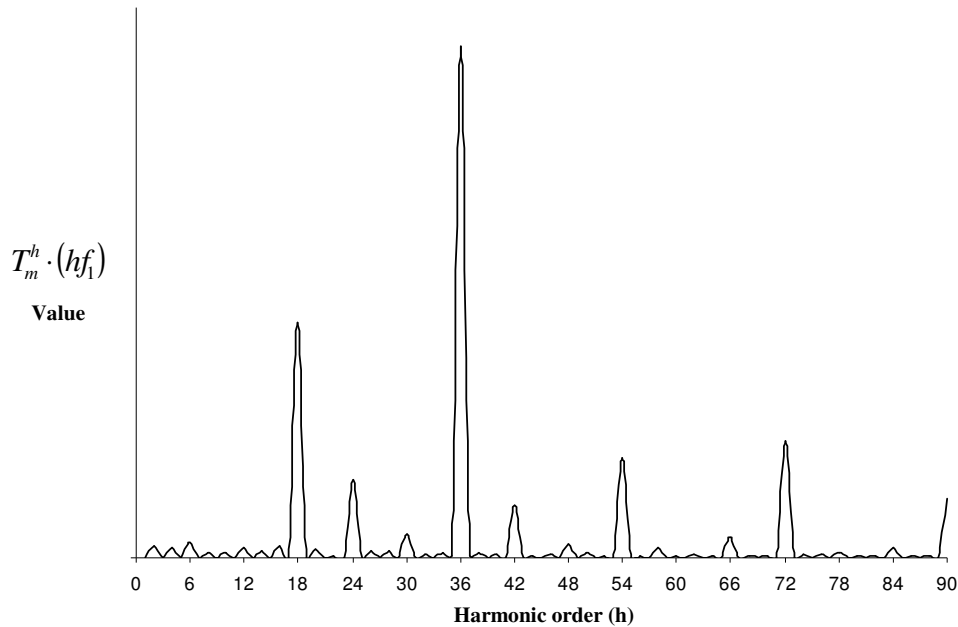


Fig. 5.23: Torque harmonic amplitude multiply with harmonic frequency obtained from FE modeling of a SynRM with pure sinusoidal current supply.

The peculiarity of SynRM is that this flux change affects the entire segment length and cyclically, the whole rotor. Normally, in other machines, only the near-to-air gap-surface zone is affected.

In comparison, IM rotor includes a shared rotor back iron structure which acts like an accumulator for all rotor teeth flux variation, and by proper slot end positioning this will reduce

the internal flux variation inside the rotor body effectively (at almost zero slip), see Fig. 5.5. But the surface variation is not affected by this. Rotor iron losses in an IM are low compared to those in the stator.

Indeed in the SynRM rotor iron losses could reach a level that can be comparable to the stator ([33] and a measurement result is presented for ALA-type in [27]).

Efficiency consideration could change and modify the design procedure compared to the strategy of just maximizing torque.

Furthermore on changing of geometrical parameter, Fratta for example suggests [3, 33] the introduction of barriers in the rotor in a suitable manners as shown in Fig. 5.7.a. There are some other solutions to reduce the iron losses; for example using low loss magnetic material in the rotor [12] or reducing the lamination thickness, also filing the stator slots ends with semi-magnetic material to reduce the slotting effect in the air gap [12, 33].

5.3.2.2 Torque ripple

Analytically torque ripple estimation, is treated in [33] and deeply in [41] this is briefly presented here:

If the first harmonic of torque ripple due to stator slotting is considered, the following equations can be written (all equations from [33]):

$$\begin{bmatrix} \lambda_d \\ \lambda_q \end{bmatrix} = \begin{bmatrix} L_d(\vartheta) & L_{dq}(\vartheta) \\ L_{dq}(\vartheta) & L_q(\vartheta) \end{bmatrix} \cdot \begin{bmatrix} i_d \\ i_q \end{bmatrix}; \quad \frac{\partial \lambda_d}{\partial i_q} = \frac{\partial \lambda_q}{\partial i_d} \quad (5.21)$$

$$L_d(\vartheta) \cong L_{d0} + \Delta L_d \cdot \cos(3pq\vartheta) \quad (5.22)$$

$$L_q(\vartheta) \cong L_{q0} - \Delta L_q \cdot \cos(3pq\vartheta) \quad (5.23)$$

$$L_{dq}(\vartheta) \cong -\Delta L_{dq} \cdot \sin(3pq\vartheta) \quad (5.24)$$

Due to the inductances dependency to rotor angle, another term must be added to eq. 5.16 in which (p) is the pole number:

$$\frac{2}{3}T(\vartheta) \cong \frac{p}{2}(\lambda_d i_q - \lambda_q i_d) + \frac{1}{2} \left(i_d \frac{\partial \lambda_d}{\partial \vartheta} + i_q \frac{\partial \lambda_q}{\partial \vartheta} \right) \quad (5.25)$$

Of course the average value of the second term is zero, but this term dominates when it comes to the torque ripple. By introducing inductances dependency to position in the above equation in a one stator slot skewed machine, torque can be calculated by the following equation in which (p) is the pole number:

$$T(\vartheta) \cong \frac{3}{2} \frac{p}{2} \left(\frac{3q}{\pi} \sin \frac{\pi}{3q} \right) \left[(L_{d0} - L_{q0}) i_d i_q + (\Delta L_d + \Delta L_q) i_d i_q \cos(3pq\vartheta) - \Delta L_{dq} (i_d^2 - i_q^2) \sin(3pq\vartheta) \right] \quad (5.26)$$

Torque ripple has two components, first one is proportional to average torque ($i_d i_q$), and the second term one is responsible for no load ($i_q=0$) condition ripple.

ΔL_d is caused by oscillation of the Carter's factor, while ΔL_q is mainly related to oscillation of the circulating flux component (L_{cq}) [33]. By using a distributed anisotropic rotor both these parameters will vanish, but in this case ΔL_{dq} will not be zero, because of the presence of the stator slots.

Considering eq. 5.25, regarding the effect of supply on torque and iron losses, there are two ideal conditions: ideal current source or constant current condition, and ideal voltage source or constant flux condition.

In the constant current case the main responsible for torque ripple is the second term of the torque equation, where slot harmonics force the fluxes to change.

But in the constant voltage case slot harmonics effect cause harmonics in the current, and the torque ripple is transferred from the second term to the first term. In this case fluxes are not highly affected. (Refer to [33] for analysis from the control point of view)

From the torque ripple point of view these two ideal conditions do not change the ripple; it is not clear what will happen if a control loop is introduced which combines these two ideal conditions [33]. More study is needed to investigate the exact effect.

But from the iron losses point of view in the first case higher losses are expected due to bigger flux variation compare with the constant voltage case. More study is needed to investigate the exact effect.

An important geometrical parameter that affects the torque ripple is the number and position of the barrier ends in the air gap. Based on this concept some suggestions are discussed in [37]. The main rule is that the barrier number and positions are strongly related to the stator slot number.

5.3.3 Torque per kVA & power factor

Another two important performance characteristics are the torque/KVA and PF. Using eq. 5.16 and the vector diagram in Fig. 5.24 the T/Amp ratio can be derived according to the following.

Observe that $\left(\xi = \frac{L_d}{L_q} \right)$ is the saliency ratio, see also [18, 34]:

$$T = k_1 L_d p \left(1 - \frac{1}{\xi} \right) i_s^2 \cdot \sin \theta \cdot \cos \theta \quad (5.27)$$

$$KVA = k_2 v_s i_s = k_2 \omega_r i_s \sqrt{L_d^2 i_d^2 + L_q^2 i_q^2} =$$

$$= k_2 \omega_r i_s L_d \sqrt{i_d^2 + \frac{i_q^2}{\xi^2}} \approx k_2 \omega_r i_s L_d i_d = \quad (i_d \gg \frac{i_q}{\xi})$$

$$KVA \approx k_2 \omega_r L_d i_s^2 \cdot \cos \theta \quad (5.28)$$

Using the above equations we have:

$$\frac{T}{KVA} \approx \frac{k_1 L_d p (1 - \frac{1}{\xi}) i_s^2 \cdot \sin \theta \cdot \cos \theta}{k_2 \omega_r i_s L_d i_s^2 \cdot \cos \theta} \approx k \frac{p}{\omega_r} (1 - \frac{1}{\xi}) \cdot \sin \theta \quad (5.29)$$

The fundamental apparent power factor, by using the ideal vector diagram in Fig. 5.24, is [23, 31]:

$$IPF = \cos \Phi = \cos \left(\tan^{-1} \left(\frac{\frac{L_d i_d + i_q}{L_q i_q + i_d}}{\frac{L_d - 1}{L_q}} \right) \right) = (\xi - 1) \sqrt{\frac{\sin(2\theta)}{2(\tan \theta + \xi^2 \cot \theta)}} \quad (5.30)$$

This has a maximum value of [23]:

$$IPF_{\max} = \frac{\xi - 1}{\xi + 1} \quad \text{with: } \tan \theta = \sqrt{\xi} \quad (5.31)$$

Eq. 5.29 for T/KVA and the above equations for IPF clearly show that the saliency ratio has a great influence on these parameters. The higher the saliency ratio, the better are the PF and T/KVA values. Fig. 5.25 shows variation in apparent power factor with saliency ratio [23]. If one step more realistic calculation is made by considering Lsl: stator leakage reactance and Rs: winding resistance, there will be a small improvement in power factor. Maximum power factor including Rs and Lsl has been analyzed in [29, 9], and compared with analysis without Rs and Lsl in [Lipo, 33].

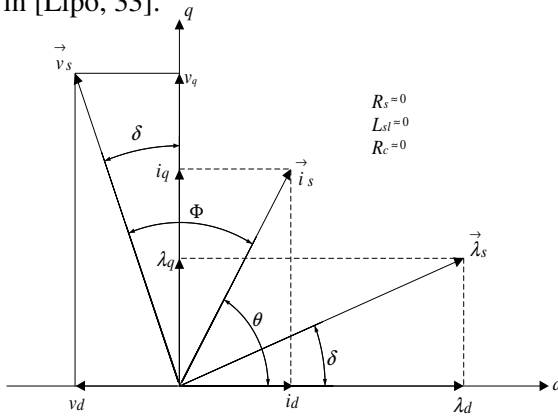


Fig. 5.24: SynRM ideal (air gap) vector diagram (all values are peak values).

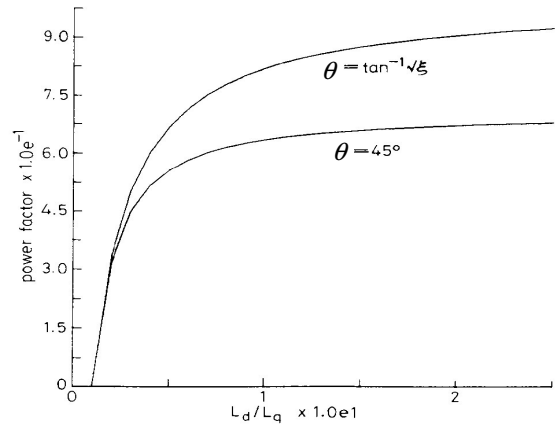


Fig. 5.25: Variation in power factor with saliency ratio [23].

5.3.4 Inverter size and field-weakening range

Field-weakening range and inverter size are also strongly dependent on the saliency ratio. For example it will be shown below that for two different cases to field-weakening is strongly dependent on saliency.

1- Field-weakening with maximum torque [3, 33, 28, 27] see Fig. 5.26.a.

2- Field-weakening with maximum PF and constant d-axis flux [33, 9] see Fig. 5.26.b.

For case one and a certain rating of inverter (i_0, v_0), neglecting assuming that saturation, and using the ideal motor with vector diagram according to Fig. 5.24 the field weakening ratio is given by the following:

$$r_{\max T} = \frac{\omega_1}{\omega_0} \bigg|_{\max T} = \frac{1}{2} \left(\xi + \frac{1}{\xi} \right) \quad (5.32)$$

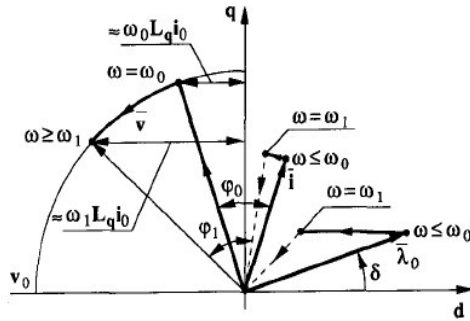
$$\text{where :} \quad \omega_0 \big|_{\max T} = \frac{v_0}{i_0 L_q} \sqrt{\frac{2}{\xi^2 + 1}} \quad \omega_1 \big|_{\max T} = \frac{v_0}{i_0 L_q} \sqrt{\frac{1}{2} \left(1 + \frac{1}{\xi^2} \right)}$$

And for case two:

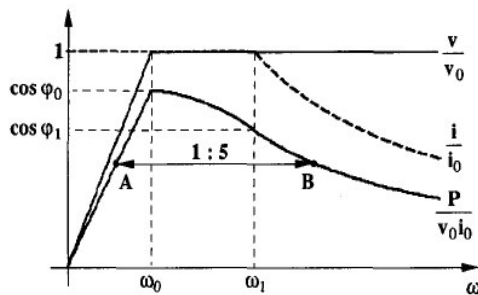
$$r_{\max PF} = \frac{\omega_1}{\omega_0} \bigg|_{\max PF} = \frac{1}{2} \left(\sqrt{\xi} + \frac{1}{\sqrt{\xi}} \right) \quad (5.33)$$

$$\text{where :} \quad \omega_0 \big|_{\max PF} = \frac{v_0}{i_0 L_q} \sqrt{\frac{2}{1 + \xi^2}} \quad \omega_1 \big|_{\max PF} = \frac{v_0}{i_0 L_q} \left(\frac{\frac{1}{2} \left(1 + \frac{1}{\xi} \right)}{\sqrt{\frac{1}{2} \left(\xi + \frac{1}{\xi} \right)}} \right)$$

For more detailed derivation of these equations refer to Appendix B and [33, 9]. In both cases the field weakening range is strongly dependent on the saliency ratio.

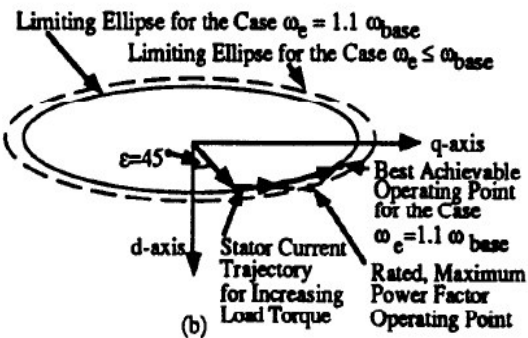
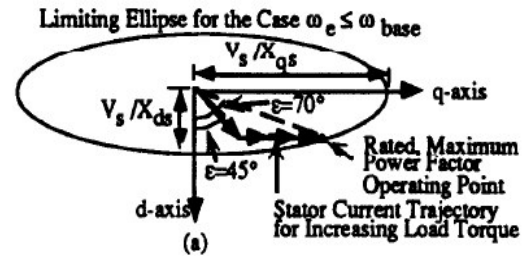


Vector loci for maximum power.



Voltage, current, and power versus speed.

(a)



Showing elliptical boundaries for the current vector I_s for the cases a) $\omega_e \leq \omega_{\text{base}}$ and b) $\omega_e = 1.1 \omega_{\text{base}}$.

(b)

Fig. 5.26: Field weakening with reference conditions as maximum torque (a) [3], and as maximum power factor (b) [9].

In both cases when the operation speed is below base speed, the maximum voltage v_0 is reached at a flux angle, which mainly depends on the ratio below. The lower this ratio is, the wider will be the constant power speed range for a given utilization factor of the inverter [3], also see (ω_1) in eqs. 5.32 and 5.33.

$$\frac{i_0 L_q}{\lambda_0} = \frac{\Lambda_q F_0}{\Phi_0} \quad (5.34)$$

Where Λ_q is the permeance, Φ_0 is the pole flux, and F_0 is the total stator MMF. Thus the ratio can be directly related to the machine design. It follows that it is preferable to increase the torque by increasing the pole flux instead of the magneto motive force (for more detail refer to [3]).

The base speed equations for both cases and the above equation, all suggest that for having high inverter utilization and high field weakening range we need to have as much as possible a machine design with **low L_q** and high saliency ratio.

5.3.5 Maximum saliency ratio, inductance difference and efficiency times power factor

$$\left. \frac{L_d}{L_q} \right|_{\max} \quad \& \quad (L_d - L_q)_{\max} \quad \text{and} \quad (\eta \cdot \cos \phi)_{\max}.$$

An important aspect to consider in the design of the SynRM rotor is the effect of the rotor dimensions on the machine inductances. The inductances are important due to the fact that the torque of the SynRM is directly related to the difference between the two axis inductances, while the maximum power factor in turn is dependent on the ratio of the two-axis inductances, [31].

On the other hand, the inductances difference ($L_d - L_q$) takes no account of the voltage requirements of the motor. The saliency ratio ($\xi = L_d / L_q$) provides a more general guide to the overall performance, because the power factor, the speed range at constant power, and several aspects of the dynamic response, are all directly related to ξ [23].

In fact both above claims are important, and also with refer to last chapter's contents, it can be conclude that the machine design strategy is directly related to the expected performance of the final design. High torque and efficiency is equivalent to maximizing the ($L_d - L_q$) and vice versa. A high power factor and T/KVA is equivalent to maximize ($\xi = L_d / L_q$) and vice versa.

Inverter rating not only is for example related to the power factor but also to the motor efficiency, this suggests that for optimum inverter size a maximum of $(\eta \cdot \cos \phi)$ for the motor design must be targeted.

Taking this into consideration the optimum geometric dimensions are different when maximizing ($L_d - L_q$) compared to the dimensions when maximizing the saliency ratio simple anisotropic structure shown in Fig. 5.27 is used to explain the optimization process for both situations. For detailed calculation refer to Appendix C, the main idea is derived from [23].

For maximizing the inductances difference, the following relations are applicable (see Fig. 5.27 for the definition of (t)):

$$t = \frac{1}{\sqrt{\mu_r}} \quad \& \quad k_{wq} = \frac{1}{\sqrt{\mu_r} - 1}$$

And for maximizing the inductance ratio (saliency):

$$t = 0.5 \quad \& \quad k_{wq} = 1$$

This simply shows that the optimum geometric shape is directly related to the targeted variables.

There are other examples related to this issue in [31, 18], which investigates the effect of geometric parameters on machine inductances and performance by means of a finite-element analysis.

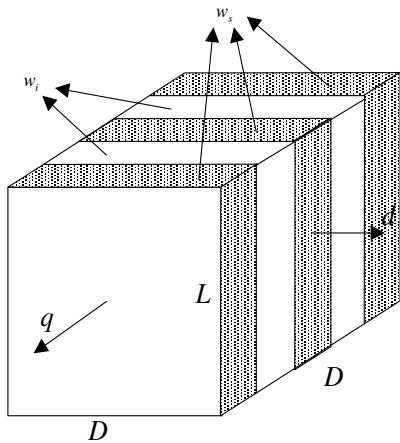


Fig. 5.27: A simple anisotropic structure.

$$\begin{aligned} & \text{iron } \mu_r \\ & \text{insulation} \\ & k_{wq} = \frac{\Delta w_i}{w_s} \\ & = \frac{1}{\frac{1}{t} - 1} \\ & t = \frac{\Delta w_i}{w_s + w_i} \\ & = \frac{1}{1 + \frac{1}{k_{wq}}} \end{aligned}$$

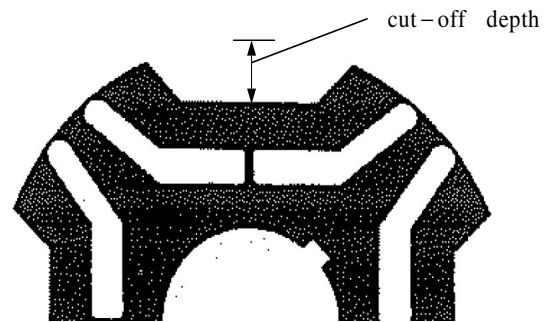


Fig. 5.28: cut-off depth definition [31].

For example in the rotor structure shown in Fig. 5.28, the cut-off depth has been changed and its effect on machine inductances is shown in Fig. 5. 29, for more information refer to [31].

Fig. 5.29 shows that ($L_d - L_q$) is maximized if the cut-off depth is set to about 6mm, on the other hand if (L_d/L_q) is to be maximized then the cut-off depth must set to 12mm, or qualitatively the more iron there is the bigger is the value of the ($L_d - L_q$); and the lower is (L_d/L_q). Increasing air reduces L_q effectively, and increasing iron increases L_d significantly.

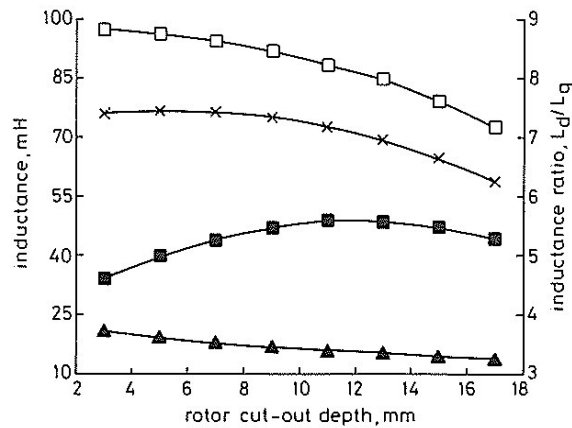


Fig. 5.29: [31],

Effect of cut-out depth on inductances of RSM

$I_d = 10 \text{ A}$; $I_q = 17.4 \text{ A}$; actual cut-out depth = 14.0 mm

□—□ L_d
 ×—× $L_d - L_q$
 ■—■ L_d/L_q
 ▲—▲ L_q

6 PRIMARY DESIGN PROCEDURE

6.1 Scope

Due to the complexity of the geometry and the high number of variables involved, a simple procedure for rotor design will be developed in this chapter by using the simple theory of rotor magnetic behavior.

The main goal is to find an optimum distribution of rotor barriers for each series of major selected parameters. This main selected parameters are for example: insulation ratio in q- and d-axis, number of barriers, number of poles, end points of barriers in the air gap, type of barrier distribution ie. with- or without-cut-off, see Fig. 6.1, stator slots per pole per phase (q). Intermediate variables are barriers position and sizes.

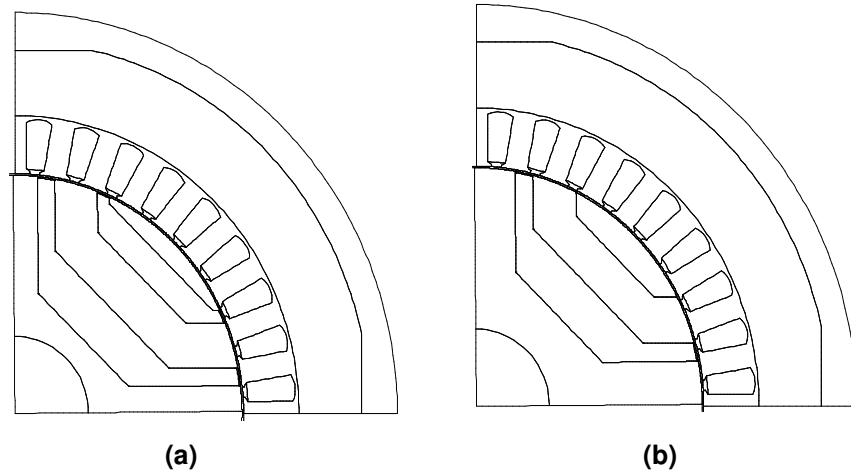


Fig. 6.1: Two main rotor barriers positioning; (a) 2 barriers without cut-off, (b) 2 barriers with cut-off (1 barrier + 1 cut-off).

This analysis is based on a completely linear theory, the main assumptions are: stator geometry is fixed especially the air gap diameter, Saturation is disregarded, pure stator sinusoidal MMF in the air gap is assumed and the stator slotting effect is neglected.

Positioning of barriers in the rotor has two main patterns as Fig. 6.1 shows. In type (a) the part of the rotor along the q-axis nearest to the air gap for, is iron, but in type (b) this layer is air. The main procedures for analyzing both of them are quite similar but with some differences. Here the without-cut-off type will be treated.

6.2 Without cut-off distribution type

General arrangement in the without cut-off type is shown in Fig. 6.2.

6.2.1 End point angles (rotor slot pitch angle: α_m)

For positioning the barriers end points in the air gap two assumptions are considered, constant rotor slot (barrier opening in the air gap) pitch, and an imaginary extra point for the last segment (S_{k+1}), point (B), $*$, in Fig. 6.2 [37].

For introducing air in the rotor there is another simple rule for size of the barrier in the air gap or size of barrier in the d-axis that make it possible to achieve the initial condition of barrier position in the rotor to search the optimum insulation ratio. We introduce rule number 3.

- 3- Barrier opening equivalent angle and position in the air gap should follow the rotor slot pitch values in the theoretical calculations (see chapter 5 & 6 for more information).

This means that for one barrier, by considering an extra imaginary point for the second segment near the q-axis, the rotor slot pitch is:

$$\alpha_m = \frac{\frac{\pi}{2p}}{k+1} = \frac{\frac{\pi}{2 \times 2}}{1+1} = \frac{\pi}{8} = 22.5^\circ \text{ mec.}$$

(k: number of barriers, p: pole pair numbers, detailed discussion is presented in chapters 5 & 6). Therefore the equivalent angle of barrier opening in the air gap and angle between axis of barrier and the d-axis are almost equal to $\alpha_m / 2 = 11.25$ using a first approximation.

For the first approximation we assume that the amount of iron in rotor and stator back are equal. Therefore barrier width in q-axis (W1) will be:

$$\left(\frac{DR - DRI}{2} \right) - HRS = 55.45 - 25.5 = 29.95 \text{ mm.}$$

For calculating each segment size, we make the same assumptions ie. segment width is proportional to MMFd (p.u.) over the segment and this gives segment one a width of about 12.3mm and segment two a width of about 13.2mm. consequently the radial position of the barrier in the q-axis becomes Yq=53.8mm, using this first approximation.

Using rule two makes it possible to position and size the barrier in the d-axis. The d-axis barrier width (W1d) for an air gap opening which should be around 11 degrees will be 16mm.

Now for finding the best insulation ratio in the q-axis there is a starting point. By changing the barrier width in the q-axis and also, proportionally with it, for a first barrier approximation the width in the d-axis, the effect of insulation ratio can be investigated.

Effect of increasing air in the constant radial position in the rotor (Yq=cte) for the first approximation, is shown in Fig. 7.1. The optimum value (W1=22.5) for air is lower than the initial point (W1=29.95mm). This can be explained by the positive effect of the second (upper) segment in capturing more flux from the stator MMFd and thereby increasing Ld.

Because maximization of torque strategy needs maximum iron in the rotor structure, as more MMFd can be captured by the rotor. Around the optimum point torque sensitivity to W1 or kwq (q-axis insulation ratio) is very low, and the reason for this is the low effect of increasing the air on the reduction of Lq and also low effect of increasing iron to increase Ld due to constrain which exists in the stator part of the d-axis flux path, and consequently low torque sensitivity around the optimum point W1. On the other hand there is an optimum point, because there is a trade off between reducing Lq and Ld by increasing W1 (or insulation ratio) for maximum torque. Torque is proportional to (Ld-Lq).

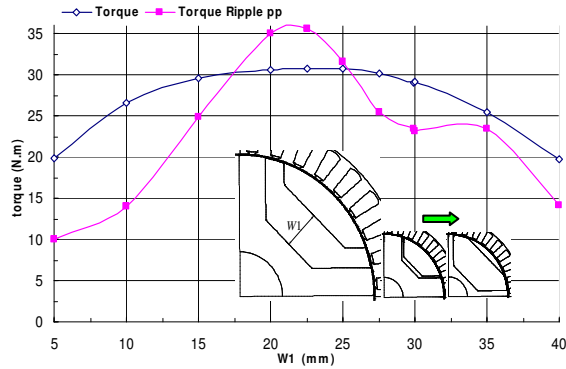


Fig. 7.1: Torque and torque ripple for different barrier width in the q-axis and proportionally in the d-axis in a constant radial position ($Y_q = cte$).

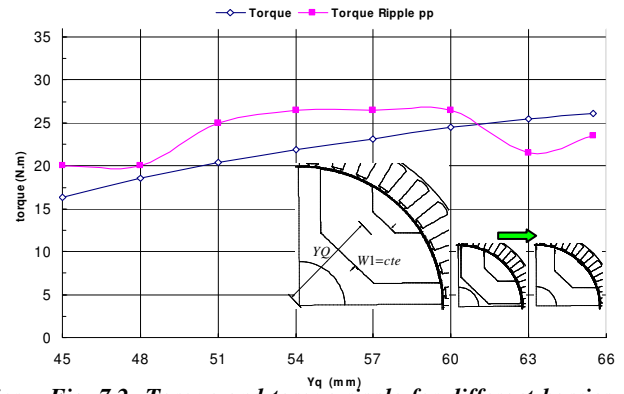


Fig. 7.2: Torque and torque ripple for different barrier q-axis position (Y_q) with a constant and large width ($W_1=29.95$).

In the next analysis, the importance of finding optimum insulation ratio in the q-axis as the first priority for the design will be demonstrated. This analysis clearly shows that having an initial design is necessary.

If instead of insulation ratio in the q-axis, the barrier position in the q-axis (Y_q) is considered as the first parameter for analysis then there will be two bounding situations. First the changing of the q-axis position of a barrier by small width, for example equal to stator slot width. Second use of one barrier with maximum possible width for example in this case 29.95mm.

Both of these have been analyzed and the results are shown in Figs.7.2 and 7.3. Also the same analysis for optimum insulation ratio ($W_1=22.5$), is shown in Fig. 7.4.

In both cases (small and large barrier width) the maximum achievable torque does not exceed 27 Nm/pole. But for the optimum insulation ratio as is shown in Fig. 7.4, torque can reach a value that is higher than 31 Nm/pole.

The problem complexity will arise if the number of barriers is increased. These three analysis show:

- 1- First priority for optimization is finding the optimum insulation ratio.
- 2- Torque sensitivity in Y_q is small if the barrier width and insulation ratios are selected suitable and optimum (Fig. 7.4). L_q is inversely proportional to 'la' which is the total air in the q-axis and changing Y_q does not change 'la'.
- 3- Comparison of Figs. 7.2 and 7.3, clearly shows the existence of an optimum barrier width W_1 (or equivalently insulation ratio kw_q) and also an optimum for its related position in the q-axis (Y_q), between these two boundaries.

Fig. 7.4 shows that the optimum q-axis position of barrier is clearly close to the initial point ($Y_q=54$ mm). Also parameter Y_q , which is the barrier radial position in the q-axis for each barrier around optimum torque point, is a strong tool to control the torque ripple without interference with the average torque. What is very important about Y_q is that adjusting Y_q makes it possible to adjust the end points of the barrier at the air gap, which directly determine the torque ripple [37, 39, 40], and at the same time it does not change the average torque. In fact torque around maximum torque point is a function of the insulation ratio, mainly in the q-axis (kw_q).

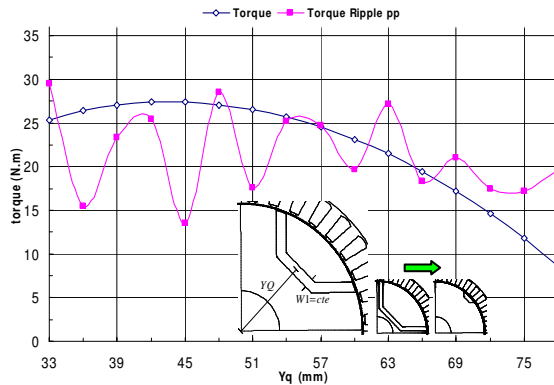


Fig. 7.3: Torque and torque ripple for different barrier q-axis position (Yq) with a constant and small width (W1= stator slot width).

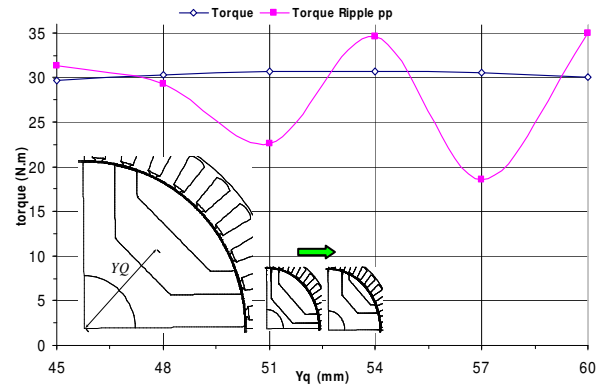


Fig. 7.4: Torque and torque ripple for different barrier q-axis position (Yq) with constant width (W1=22.5mm, the insulation ratio with maximum torque in Fig. 7.1).

To show the importance of the second rule (constant segment width all along the segment length) and its related conclusions, the correctness of this rule for this example is analyzed in the next section.

7.1.2 Barrier end points in the air gap and d-axis insulation ratio

Position and size of barrier in the d-axis can be investigated for the optimum point of insulation ratio, by three different parameters: the first one is the q-axis radial position Yq parameter which has been analyzed and shows that the end position is completely in agreement with rule 3, the second one is the d-axis barrier width or total insulation ratio in the d-axis (kwd), and the third one is the barrier leg angle in the d-axis (α).

Effect of the barrier width in the d-axis (W1d) on torque is shown in Fig. 7.5.

From W1 analysis the optimum value for W1d was 12 mm corresponding to W1=22.5 mm, which is smaller than the initial value of 16mm corresponding to W1=29.95 mm (equivalent to half of rotor slot pitch in the air gap). But optimum value for W1d from Fig. 7.5, shows a value that is quite close to the value from the kwq analysis.

First of all, amount of air in the d-axis is less than in the q-axis. This follows the second rule, which is segment sizing rule. Increasing iron especially in the d-axis increases MMF capturing capacity in the rotor d-axis and consequently gives a higher value of Ld.

On the other hand the amount of iron in the q- and d-axis must be equal and the ratio of total available width for segment and barriers in the d-axes to the q-axis is a factor of $\sin\left(\frac{\pi}{2p}\right)$

which for 2 pole pair machine ($p=2$) is 0.7. All of these issues show that the barrier width in the d-axis must be reduced. Also in a wide range from 8 to 12 mm (Fig. 7.5) torque sensitivity to W1d is very low, the reason for this can be the same as for W1 in the q-axis, which is mainly due to the unbalanced non optimum iron distribution between the rotor and the stator ie. due to a non-

optimum air gap diameter. Another important issue is that the barrier width in the d-axis changes the third rule according to the following:

3- Sizing the barrier in the d-axis which follow the second rule, segment sizing, is more effective than the equivalent barrier angle in the air gap, in the previous rule three. And following rule two can distort a little the previous third rule in optimum torque situation.

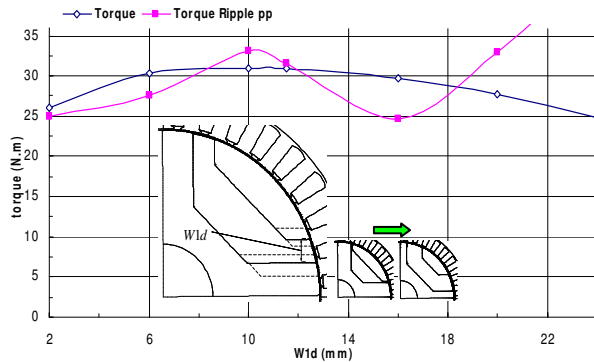


Fig. 7.5: Effect of the barrier width in the d-axis (\equiv insulation ratio) on torque for constant barrier width and position in the q-axis.

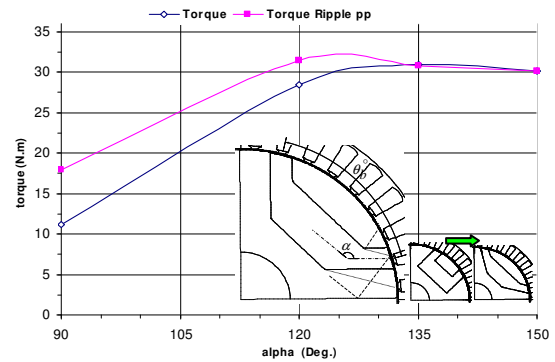


Fig. 7.6: Effect of barrier leg angle (α) in the d-axis on torque for constant barrier width and position in the q-axis.

Another parameter regarding end part of barrier in the d-axis position is the barrier leg angle. Effect of this angle on torque is shown in Fig. 7.6.

This analysis clearly shows that the segment edges in the d-axis must be parallel to the d-axis. Actually this angle is supporting those segments whose axial line curve follow the natural path of the d-axis flux component and orthogonal to the q-axis flux line. Here this angle is 135 deg.

Actually there are two bounding situations (α) for a fixed q-axis position of barrier. Low (α) not only increases the amount of the iron and captured flux from MMF_d but also increases the q-axis flux going through the rotor component and therefore also L_q , while high (α) reduces the amount of iron and the captured flux from MMF_d and increases saturation at least in some part of the segment and therefore reduces L_d . Thus there will be an optimum point for both parameters. This will be the same for (θ_b).

There is a different between the effect of leg angle at high and low (α), see Fig. 7.6. For angles higher than 135 deg increasing leg angle reduces the torque slightly. Reason for this can be explained by rotor MMF_d capturing capability in the d-axis. The rotor MMF capturing capability in the d-axis in this case is transferred between two segments from segment one to segment two.

7.1.3 Optimum q-axis barrier positioning

In this section the effect of changing the radial position of the barrier in the q-axis (Y_q) on machine torque is studied. But the insulation ratios and end points of barrier in the air gap are kept unchanged. This will show how critical is the constant segment width and the relative

division of iron between the two segment inside the rotor ? The result of such analysis is shown in Fig. 7.7.

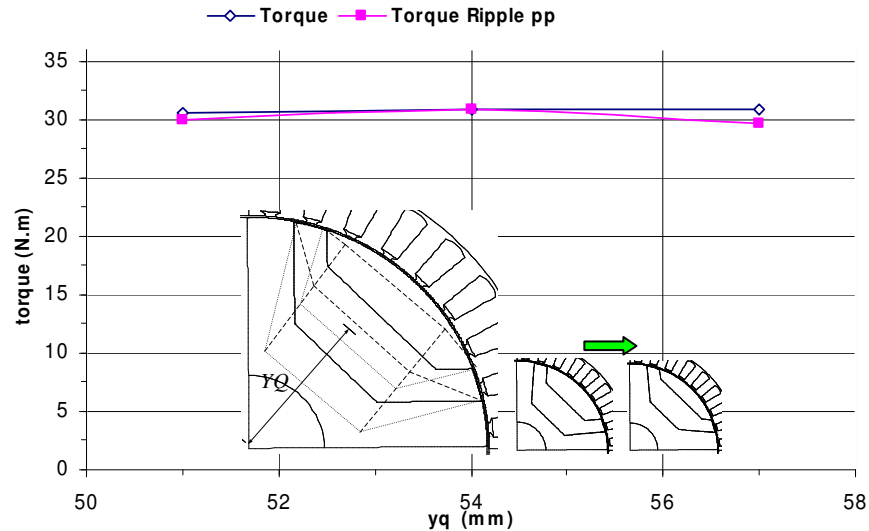


Fig. 7.7: Torque and torque ripple for different barrier position in q-axis and constant width and endpoints in the air gap.

This figure shows that the most important specifications of a barrier in the rotor are insulation ratios and end positions of the barrier.

Regarding the amount of iron in the rotor it seems that the division of iron between two segments in the q-axis is not a sensitive parameter and the second rule is weakened here. This critique shows that there are different rotor structures which really have torque close to optimum, but also rule two can still be used as a strong guide to find the best insulation ratio very close to the absolute optimum value at the first step of the design. Other analysis results can then be used for final tuning of the optimum structure.

On the other hand if the total iron in rotor is set to a critical minimum value by reducing the air gap diameter then torque sensitivity to this division must be increased.

7.2 One barrier analysis conclusions

By analyzing the effect of main parameters which are involved in barrier geometry for the simplest situation, which is the single barrier, the following general rules can be derived:

- 1- Introducing maximum anisotropy in the rotor to find optimum insulation ratio, or total air in the q-axis (l_a) is a major task.
- 2- Segments width all along the length of each one must be kept constant to achieve almost constant flux density in the segment and to increase the utilization factor of rotor iron.
- 3- A simplified but general shape of segments and barriers will be similar to those shown in Fig. 5.16. The edges of barriers and segments in the d-axis must be parallel to the d-axis and perpendicular to the q-axis. In the q-axis inside the rotor it must generally follow the natural path of the d-axis flux in the rotor and perpendicular to the q-axis flux.

- 4- The insulation ratio in the d-axis also can, independent of the insulation ratio in the q-axis, be considered as another parameter for positioning the barriers and end points of barriers in an optimal way in the d-axis. This technique is much more effective than the constant rotor slot pitch to position the rotor barriers end point in the air gap.
- 5- The insulation ratio in the d-axis of machines with more than two pole pair is smaller than the insulation ratio in the q-axis.

Almost all these rules also have been considered in chapter 6, to develop a theoretical method for dimensioning of the rotor structure.

7.3 One barrier and one cut-off

In this chapter two procedures are used to find the optimum rotor geometry for 2 barriers with cut-off type or one barrier + one cut-off rotor:

- 1- Combined theoretical and finite element method, which has been explained in chapter 6. This method uses the insulation ratios in the d- and q- axes as design parameters.
- 2- Changing the rotor geometry for all possible combination of the geometric parameters.

And finally the two methods will be compared.

7.3.1 Theoretical model aided sensitivity analysis

With the fix stator structure and a simple geometry for the rotor barriers and if theoretical methods are used with constant rotor slot pitch for all rotor slots as is explained in chapter 6, then only two parameters are involved in the optimization of the rotor geometry for maximum torque. These are the insulation ratios in the q-axis (k_{wq}) and in the d-axis (k_{wd}). The main idea of insulation ratio comes from [29, 33].

7.3.1.1 Insulation ratio in q-axis

Effect of the q-axis insulation ratio, when k_{wd} is half of k_{wq} on torque and torque ripple is modeled and the result is shown in Fig. 7.8.

The optimum insulation ratio in the q-axis for maximum torque is around 0.6~0.7, which is equivalent to (l_a) around 21mm. a little lower than the value when there is just one barrier, see last chapter. Parameter (l_a) is reduced because of the more distributed insulation and iron in the air gap. Better insulation distribution reduces the circulating component of the q-axis flux and L_q and increases the insulation utilization factor. Furthermore better iron distribution increases the rotor capturing capability of the flux from the stator d-axis MMF_d and consequently gives higher L_d . By reducing the total required insulation we can increase the amount of iron and therefore increase L_d again. The result will be higher torque (~32 Nm per pole) with lower amount of insulation (l_a).

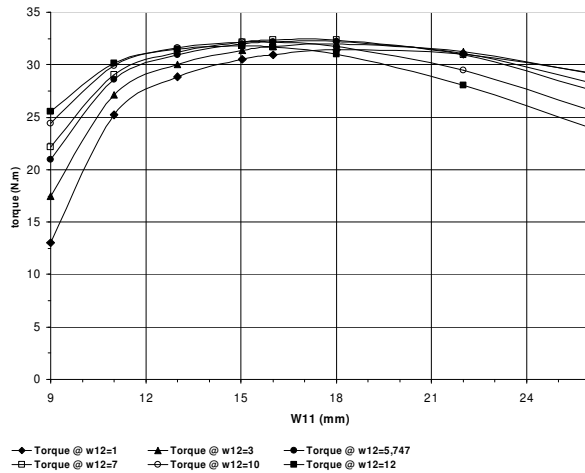


Fig. 7.12: Torque as a function of barrier width with cut-off width as parameter for two barriers with cut-off rotor geometry shown in Fig. 7.10.

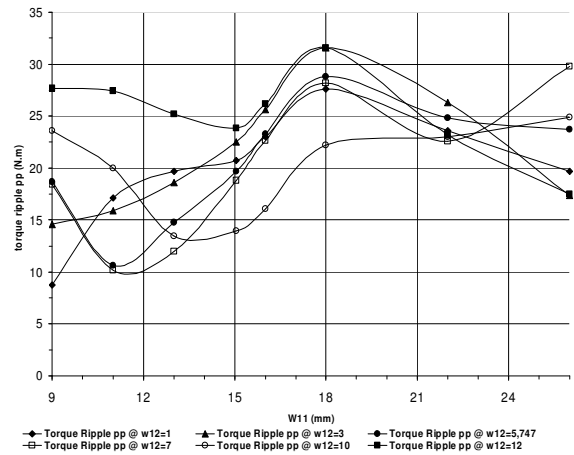


Fig. 7.13: Torque ripple as a function of barrier width with cut-off width as parameter for two barriers with cut-off rotor geometry shown in Fig. 7.10.

Parametric curves for torque are shown in Fig. 7.12, and for torque ripple in Fig. 7.13. Fig. 7.12 clearly shows that the optimum rotor geometry for maximum torque is not unique, and practically there are different geometries with almost the same maximum torque. But the optimum torque is the same for both pure geometrical and theoretical aided analysis.

Torque behavior as a function of barrier width in Fig. 7.12 is comparable with insulation ratio in the q-axis effect on torque. Therefore Fig. 7.8 shows a general effect of increasing air in the rotor on machine torque. Similarly barrier width analysis results in [31] also show the same behavior in torque if the barrier width is changed and the cut-off width is taken as parameter.

This analysis shows that the insulation ratios in both axes can be simply determined by the insulation analysis (theoretical & finite-element combined approach) and the number of calculations can be significantly reduced, here from 48 calculations in Fig. 7.11 to 19 calculations in Figs. 7.8 and 7.9.

7.3.2.2 Barrier radial position

Another parameter that involves in the rotor final geometry shape is the radial position of barrier (Y_{q1}). For the optimum $kw_q=0.6$ and $kwd=0.2$, (Y_{q1}) is around 50.4mm. For constant insulation ratios in both axis the effect of (Y_{q1}) on torque and torque ripple are shown in Fig. 7.14.

Optimum value for (Y_{q1}) from finite-element analysis is compatible with previous values (50mm). Also Fig. 7.14 shows that preliminary assumption regarding constant radial position for barrier during pure geometrical analysis of barrier and cut-off widths is quite reasonable.

As is expected (Y_{q1}) does not affect torque around the optimum point. But torque ripple is completely affected due to the change in the end point position.

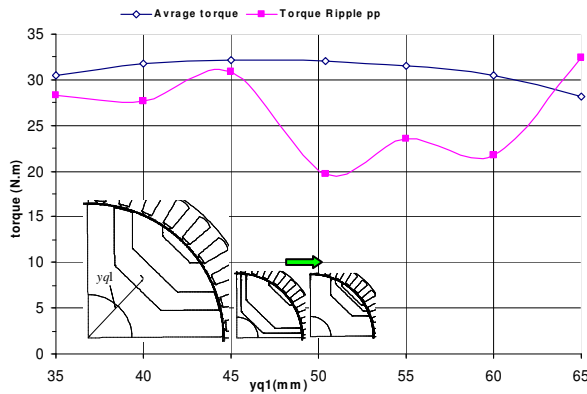


Fig. 7.14: Effect of radial position of barrier on torque and torque ripple at constant insulation ratio in d- and q-axis.

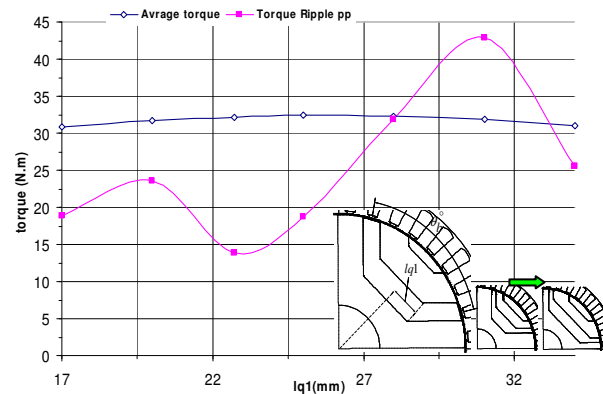


Fig. 7.15: barrier leg length in q-axis (l_{q1}) effect on torque and torque ripple for optimum insulation ratios in d- and q-axis.

7.3.2.3 Barrier leg length in q-axis

Barrier leg length in the q-axis (l_{q1}) is changed for one of the optimum points in the previous analysis ($W_{11}=15$ and $W_{12}=10$ mm) to check the constant segment width and end position effect. The result is shown in Fig. 7.15. The optimum value for (l_{q1}) was around 22.7mm which is compatible with the value of (l_{q1}) in Fig. 7.15.

Radial position (Y_{q1}) and leg length in q-axis (l_{q1}) of the barrier analysis show that the exact position of barrier and consequently constant segment size are not deeply affecting the torque but changing the end point position will affect the torque ripple.

7.3.3 Comparison

From the analysis of two barriers with cut-off type geometry the following results can be abstracted:

- 1- Both results from pure geometrical analysis and combined theoretical and finite-element analysis are reasonably close to each other, so it will be correct to say that the combined theoretical-FEM analysis is the faster and much more practical and understandable method of optimization.
- 2- From the above note and other analysis such as the radial position and leg length of barrier analysis it has been shown that the most important parameters in the rotor anisotropic geometry characteristic are firstly the insulation ratio in the q-axis and secondly the insulation ratio in the d-axis. The shape and path of the barrier line inside the rotor do not affect the torque significantly. It has been shown that in some cases when required, it is possible not to follow the constant segment width rule especially when there is unbalance and non-optimal iron distribution in the motor.
- 3- The theoretical aided method can be used as a fast procedure to find the most important parameter values which are insulation ratios, for any number of rotor barriers, and motor pole numbers.

- 4- For points 3 and 4 the result is around and very close to the optimum point if the theoretical aided method is used, but it is not the absolute optimum.
- 5- Torque ripple can be controlled by the end point positions of barriers for example by using Y_{q1} and l_{q1} as parameters without affecting the torque.
- 6- Optimum point for maximum torque is not unique, see Fig. 7.12.

8 ELECTRO MAGNETIC SENSITIVITY ANALYSIS AND OPTIMIZATION (BASED ON THE THEORETICAL INITIAL DESIGN PROCEDURE)

8.1 Average torque optimization

From confirmation of the theoretical aided design procedure in chapter 7, the number of finite-element calculations is reduced effectively and other parameter's effect on torque can be investigated. One of these parameters is the number of barriers.

With refer to chapter 6, an extra angle (β) is defined to introduce another degree of freedom for barriers end points in the air gap. This angle is kept constant in this part of analysis, because the main goal here is to investigate the effect of rotor barrier number on torque, and not torque ripple. It will be shown that some kind of independent torque and torque ripple optimization is possible by introducing this angle.

Therefore, for normal rotor structure and with cut-off structure this angle is kept constant so that the rotor slot pitch by considering two imaginary point in the q-axis for normal (without cut-off) and one point for the cut-off structure, becomes constant all around the rotor circumference, for more information refer to chapter 6.

(Rotor structure in Fig. 7.10 shows a - two barriers with cut-off.)

8.1.1 Torque and torque ripple for different number of barriers

The optimum point for each number of barriers is calculated, base on finding the optimum insulation ratio in the q-axis when insulation ratio in the d-axis is half of that in the q-axis. Then at optimum q-axis insulation ratio the best d-axis insulation ratio is determined. The position and size of barriers, with each selection of insulation ratios is calculated base on theoretical calculation in chapter 6.

The resultant torque and torque ripple per pole as a function of barrier number for both arrangement models are shown in Figs. 8.1 and 8.2. Also a comparison between the two models from the torque point of view is demonstrated in Fig. 8.3.

Actually the cut-off barrier becomes very small if the number of barriers is increased. Generally one extra barrier higher in with cut-off model is equivalent to the without cut-off model. This is correct if rotor slot pitch is kept constant.

Increasing the number of barriers directly and effectively reduces the circulating component of q-axis flux but it does not affect the going-through component. Also increasing the numbers of barriers does not affect the d-axis inductance very much. Therefore the torque will not be affected if the number of barriers is increased more than a certain value [2, 4], which from Fig. 8.3 is

around 3~5 barriers. The barrier widths are calculated according to constant permeance for barriers and optimum distribution rule for minimizing the going through component of the q-axis flux [33] and chapter 6.

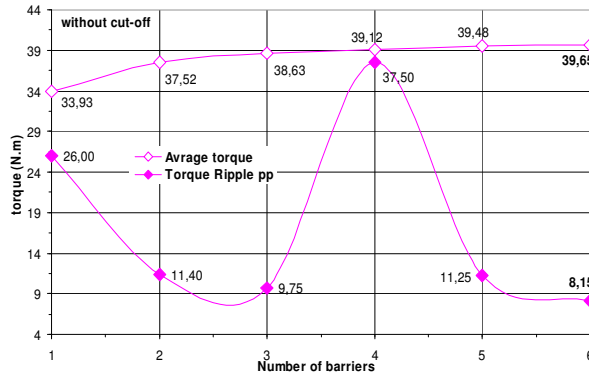


Fig. 8.1: Number of barriers effect on optimum torque and its related torque ripple per pole for rotor structure model: without cut-off. There are no tangential ribs and assumed optimum current angle control is.

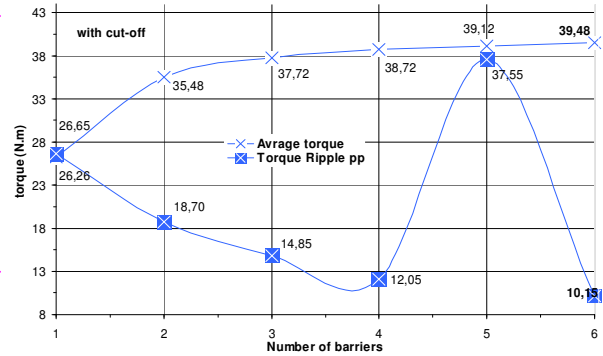


Fig. 8.2: Number of barriers effect on optimum torque and its related torque ripple per pole for rotor structure model: with cut-off which is also considered as a barrier. There are no tangential ribs and optimal current angle control is assumed.

8.1.2 Number of layers effect on machine's inductances

Another way to compare all different structure is to calculate the machine inductances at an operating point. Results from such an analysis are presented in Fig. 8.4.

By increasing the number of layers from 2 (salient pole machine) to 5 (2 barrier machine without cut-off) the q-axis inductance reaches its minimum.

As it is discussed in chapter 6, the q-axis flux has two components: The circulating component and going through component.

For each number of barriers, using the optimum distribution rule for barrier width, guarantees a minimum of q-axis flux going through component. Furthermore the circulating component is inversely proportional to the square of layer number and by increasing the layer number the circulating flux reduces rapidly [2, 33].

Increasing the number of layers also increases the rotor d-axis flux capturing capability and therefore the d-axis inductance.

Machine torque is proportional to the inductances difference ($L_d - L_q$). Increasing the number of rotor layers more than 9, actually does not change the difference.

Also machine power factor is strongly dependent to inductances ratio, saliency ratio (L_d/L_q). This also does not change for number of layer more than 9.

The effect of the number of layers on machine inductances is completely compatible with the direct torque analysis in the last chapter (Fig. 8.3), and it shows that increasing the number of barrier more than 5 or number of layer more than 10 will not have any significant gain in the machine performances.

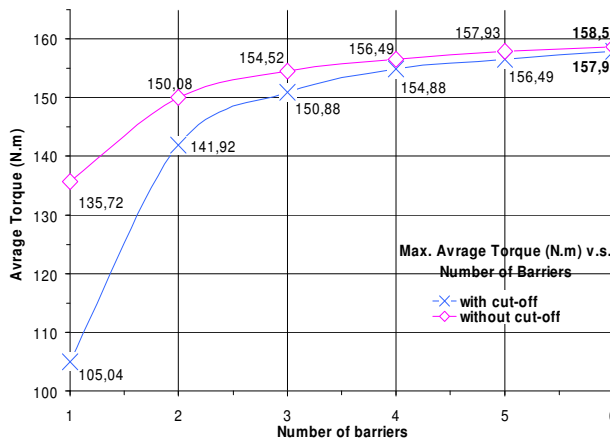


Fig. 8.3: Effect of number of barriers on optimum total torque for both rotor structure models. Comparison are made at the best current angle.

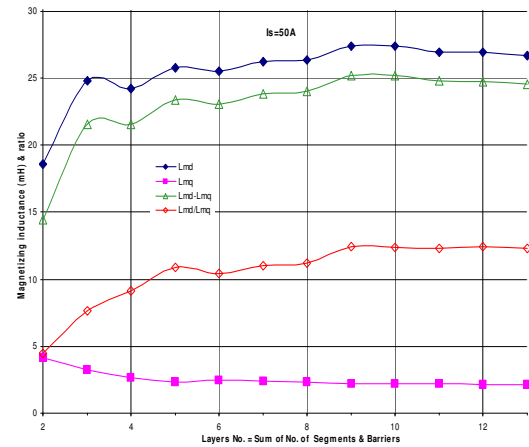


Fig. 8.4: Inductances in q- and d-axis, inductances difference and saliency ratio for different number of rotor layers. Number of layers is the sum of number of segments and number of barriers [23]. Current angle is 60 Deg., current 50A, 50Hz, 0 rpm, for inductance calculation procedures refer to chapter 2.

8.1.3 Optimum number of barriers for maximum torque

Increasing the number of layers or barriers from the mechanical and manufacturing point of view is not recommended. On the other hand increasing the barrier number more than 5, according to the discussion in the last chapter and sensitivity analysis, does not practically affect the machine torque.

Therefore three different designs are selected for more analysis. First is the 4 barrier rotor with cut-off model, second is the 4 barrier rotor without cut-off model and the third is the 5 barrier rotor with cut-off model. These designs are shown in Fig. 8.5.

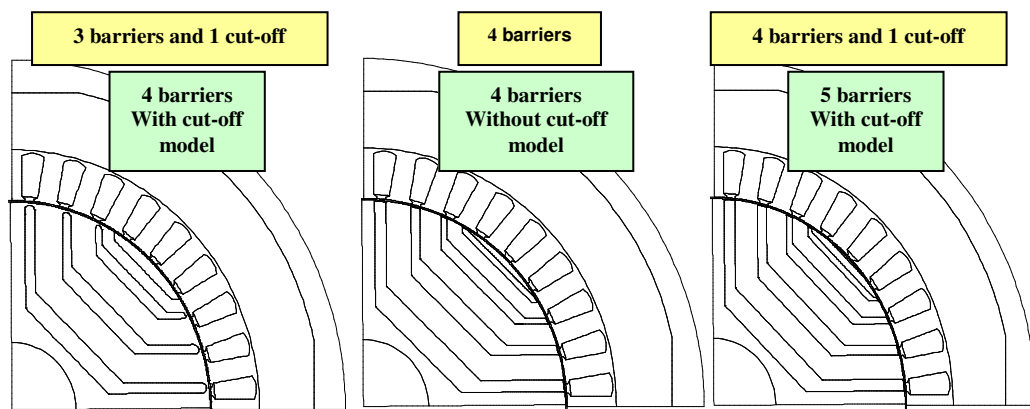


Fig. 8.5: Three different designs, from number of barriers optimization analysis selected for torque ripple minimization.

8.2.3 Torque ripple minimization results

Torque ripple minimization is applied to all selected geometries shown in Fig. 8.5 and Fig. 8.9.a again, and the final optimum geometries for maximum torque and minimum torque ripple are shown in Fig. 8.9.b.

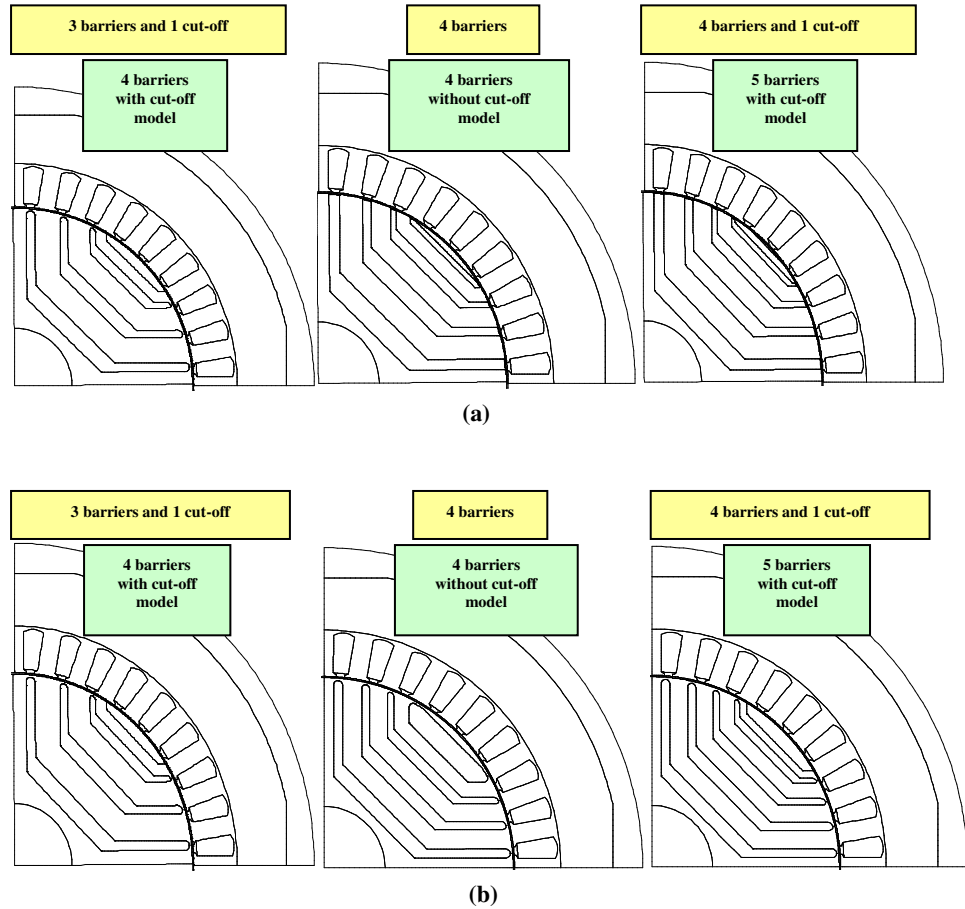


Fig. 8.9: (a): Three different geometries selected for optimization of barrier number for optimum torque performance, (b): Final geometries after applying the torque ripple minimization technique (optimizing angle (β)).

The resultant torque and torque ripple per pole as a function of barrier number for both arrangement models are shown in Figs. 8.10 and 8.11. A comparison between two models from the torque point of view is demonstrated in Fig. 8.12.

Also the torque and torque ripple of the selected modified geometries (Fig. 8.9.(b)), are demonstrated in these figures. Modifications are including the minimization of torque ripple and introduction of 1mm tangential ribs at the end of all barriers, compare barriers end-points in Fig. 8.9.a and in Fig. 8.9.b.

In all the final geometries due to the introduction of the 1mm tangential ribs in the rotor slot openings, torque is reduced by an average of 2%, because a small amount of flux is lost in the saturated ribs.

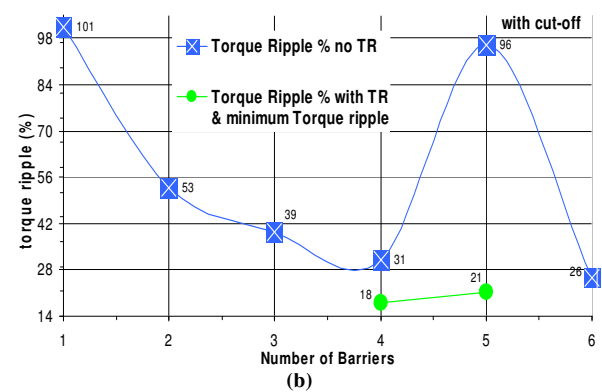
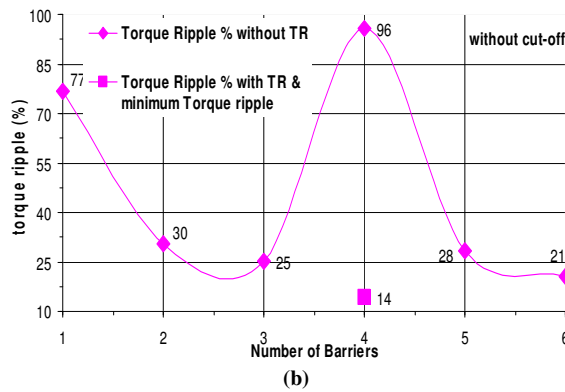
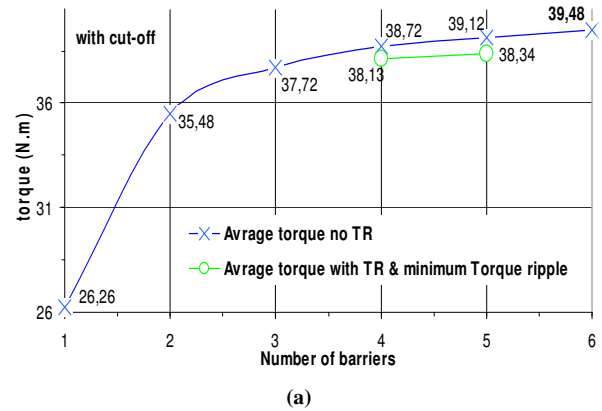
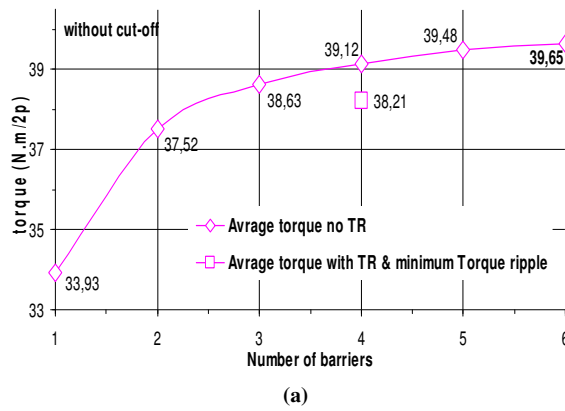


Fig. 8.10: Effect of the number of barriers on optimum torque per pole (a) and its related torque ripple in (%) (b) for rotor structure model without cut-off. Compare the results before (Fig. 8.9. (a)) and after (Fig. 8.9.(b)) applying torque ripple minimization technique and at the best current angle (TR = tangential rib).

Fig. 8.11: Number of barriers effect on optimum torque per pole (a) and its related torque ripple in (%) (b) for rotor structure model with cut-off. Compare before (Fig. 8.9.(a)) and after (Fig. 8.9.(b)) applying torque ripple minimization technique at the best current angle (TR = tangential rib).

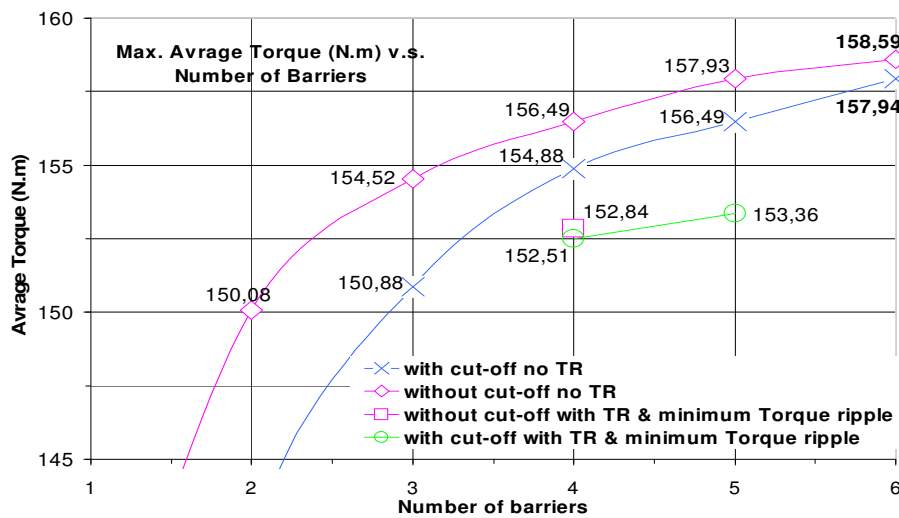


Fig. 8.12: Effect of the number of barriers on optimum total torque for both rotor structure models. Also compare before (Fig. 8.9.(a)) and after (Fig. 8.9.(b)) applying torque ripple minimization technique at the best current angle (TR = Tangential Rib).

These designs do not show a significant difference from torque and torque ripple point of view. This can be explained by the effect of barrier or layer number. With reference to Fig. 8.4 it is obvious that increasing the number of layers by more than 9 or number of barriers more than 4 do not have a significant effect on machine main inductances in the d- and q-axis. Observe that all geometries satisfy this. The main result of this analysis up to this stage can be summarized by stating that an effective procedure has been presented that reduces the number of barriers to the minimum possible value (from 5 to 3).

8.3 Main machines characteristics

In this chapter a more detailed analysis of the machine geometry is presented to enable better comparisons. Main characteristic calculations are based on inductance calculations (indirect) for a certain rotor position and different current and current angles. The other parameters are calculated by using the machine vector model. Here just the results for one of geometries in Fig. 8.9.b are presented first and then a comparative table for all will be added.

8.3.1 Inductances for different current loading and d-q axis cross-coupling

The static (the rotor is at standstill and the current vector in the stator is rotating) calculated inductances are presented in Fig. 8.13.

Regarding inductances there is not a significant different between the designs, but generally this graph is showing a specific characteristic that is related to SynRM: cross-coupling between the d-axis and q-axis inductances.

This means for example inductances in d-axis are not only a function of stator current but also a function of the current angle.

On the other hand for a certain d-axis current d-axis inductance is not only a function of d-axis current but also a function of q-axis current and it is reduced by increasing the q-axis current. The same situation also applies to the q-axis inductances. The effect of cross-coupling on d-axis inductance is negative but it is positive for the q-axis. Similar results are also reported in [23, 15, 31]. This effect can formulate as:

$$\begin{aligned} L_d &= L_d(i_d, i_q) \\ L_q &= L_q(i_d, i_q) \end{aligned} \tag{8.3}$$

Another important issue is the effect of saturation. By increasing the load the d-axis inductance is reduced, and consequently to compensate and restore the d-axis inductance and inductances difference (torque) a higher current angle is needed [42]. Effect of saturation in q-axis is not strong, mainly due to high amount of air in the q-axis flux path (high l_a). But for low loads (low currents in q-axis) the ribs (here tangential) saturation effect is obvious in the q-axis inductance also.

8.3.2 IPF for different current loading

The internal power factors as a function of the current angle for different current loadings is shown in Fig. 8.14.a. Power factor is calculated by eq. 8.4 observe that inductances are current and current angle dependent.

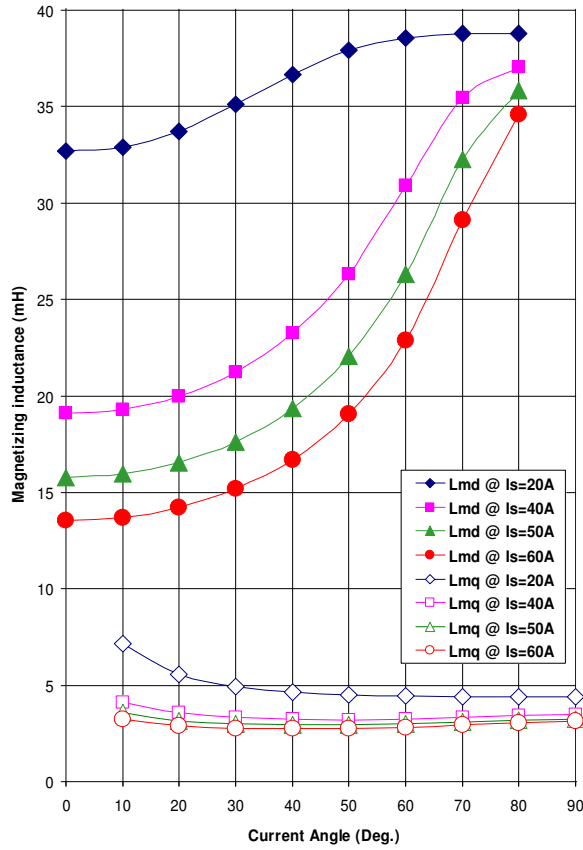


Fig. 8.13: 3 barriers + 1 cut-off models inductances as function of current angle and for different stator current.

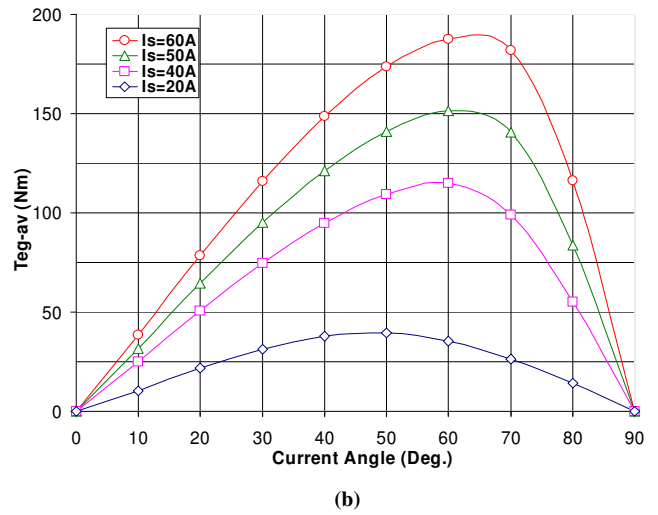
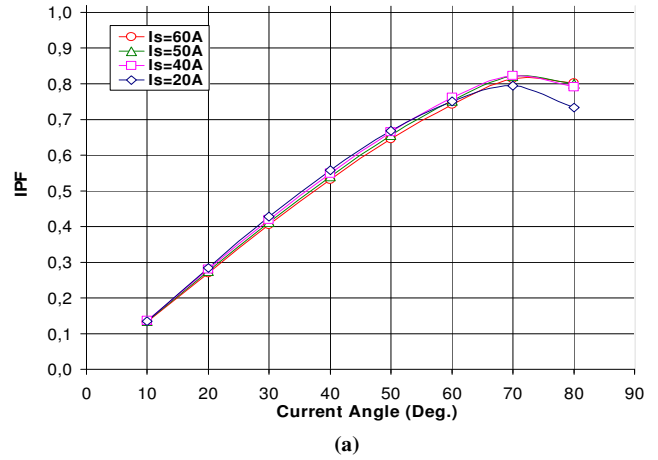


Fig. 8.14: Internal (apparent) power factor (a) and air gap electromechanical torque (b) as function of current angle and for different stator current, for the final design geometry.

$$IPF = \cos \left(\tan^{-1} \left(\frac{\frac{L_d i_d}{L_q i_q} + \frac{i_q}{i_d}}{\frac{L_d}{L_q} - 1} \right) \right) = (\xi - 1) \sqrt{\frac{\sin(2\theta)}{2(\tan \theta + \xi^2 \cot \theta)}} \quad (8.4)$$

Actually changing the stator current almost does not affect the IPF. The reason can be explained through Fig. 8.15, which shows the effects of current angle and saliency ratio on IPF in ideal conditions. Calculation results by FEM for the different final geometries show that increasing the current angle from zero to 90 deg., for all stator currents up to 50A, changes the machine saliency ratio from about 4 to 12. If this fact, increase of saliency ratio by current angle, which considers saturation and cross-coupling, is depicted in the ideal graphs of Fig. 8.15, it will be obvious that the power factor behavior is very close to the diagrams in Fig. 8.14.a and it is not sensitive to current.

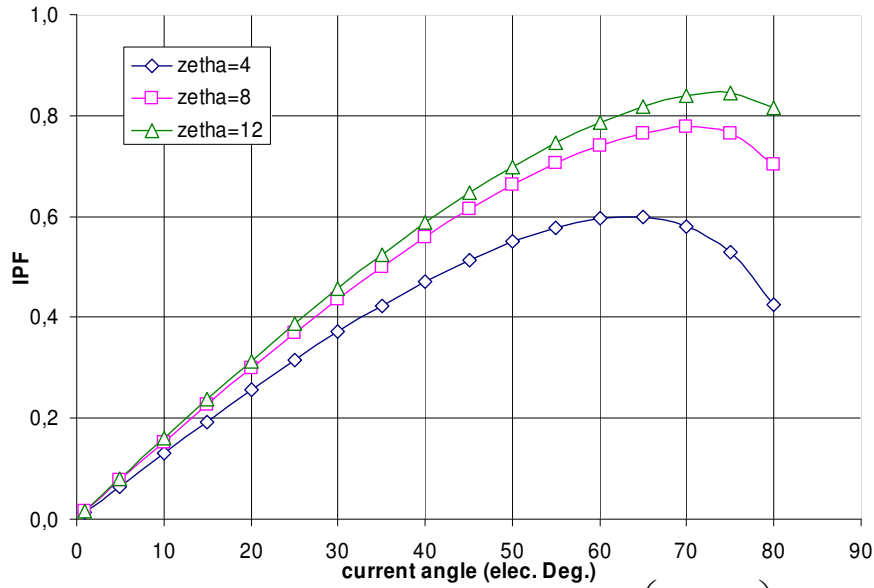


Fig. 8.15: Effect of current angle on IPF for different saliency ratios $\left(\xi = \frac{L_{dm}}{L_{qm}} \right)$, in ideal conditions (no saturation and no cross-coupling effects).

8.3.3 Torque vs. current angle curves

Air gap electro-mechanical torque as function of current angle for different current loading (at static situation) is shown in Fig. 8.14.b. Torque is calculated from the following equation assuming that inductances are current and current angle dependent:

$$T_{eg}^{av} = \frac{3}{2} \frac{p}{2} (L_d - L_q) I_s^2 \sin(2\theta) \quad (8.5)$$

Where: I_s is the stator (*rms*) current, θ is current angle and p is the pole number.

The above equation shows that the torque versus current angle graph has a sinusoidal shape with a maximum at $\theta = 45^\circ$, and this is not compatible with the FEM calculation results shown in Fig. 8.14.b.

Current angle shifts to higher values for the maximum torque mainly due to saturation effects. For a certain stator current, torque is proportional to the difference in inductances, and this is reduced by the saturation, mainly in the d-axis. For maximum torque in this situation factor $(L_d - L_q) \sin(2\theta)$ must be maximized. By increasing the current angle beyond 45° , the effect of saturation on the d-axis inductance is reduced significantly (Fig. 8.13). Similar behavior is reported in [15, 23, 42].

8.3.4 Torque, current characteristic

Regarding torque another important machine characteristic is the maximum torque for a certain stator current. Calculation results, also using Fig. 8.14.b, for maximum torque as function of stator current are shown in Fig. 8.16.

In ideal conditions (without considering saturation) equation (8.5) shows that torque is proportional to stator current square. But due to saturation and cross-coupling effects the maximum torque is an almost linear function of current as is shown in Fig. 8.16, similar response is reported in [23, 31, 7]. It seems that the maximum torque for a certain stator current always is given by the machine at a constant air gap flux and the torque follows eq. 8.6:

$$T \propto \lambda_s \cdot i_s \cdot \sin \beta \quad (8.6)$$

Another important issue is the non zero current at zero torque if a linear relation for torque versus current is assumed. This means that to make continuous working condition possible in SynRM a minimum stator current, mainly in the d-axis even for zero torque is needed, this makes it possible to keep the machine magnetized [28].

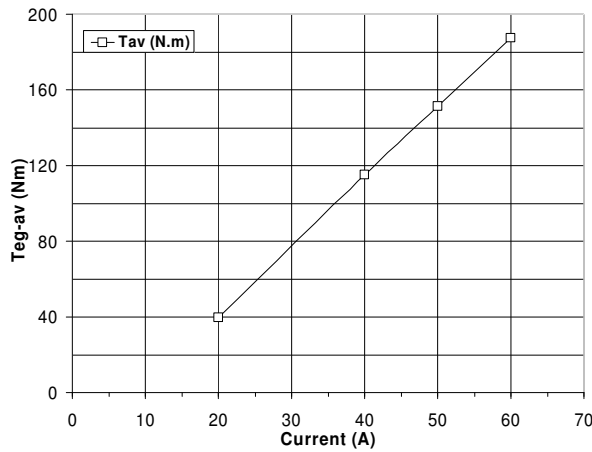


Fig. 8.16: maximum air gap electromechanical torque as function of stator current, for the final design geometry.

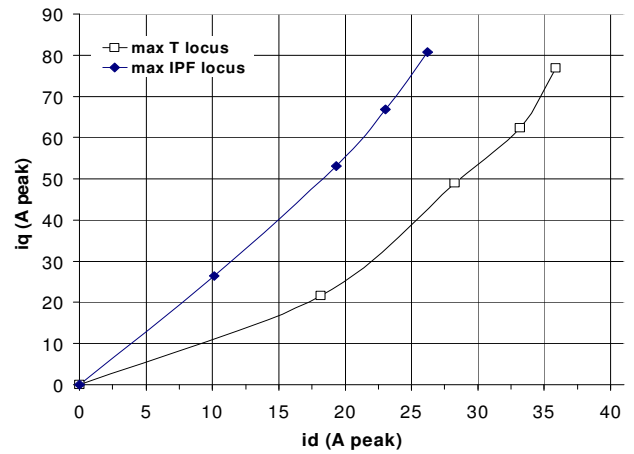


Fig. 8.17: maximum air gap electromechanical torque and apparent power factor loci, for the final design geometry.

8.3.5 Maximum torque and power factor loci

Maximum torque and power factor loci, derived from Fig. 8.14, are estimated and shown in Fig. 8.17. For a stator current maximum torque and power factor loci are different, and the current angle is larger for maximum power factor than for maximum torque. Due to saturation and cross-coupling the main machine inductances in the d- and q-axis are changing. On the other hand power factor is dependent strongly on the saliency ratio, while the torque is dependent on the difference in inductances. These last two parameters maximum values can be completely different, from a geometric and control point of view.

Simply, saliency ratio which is mainly a function of L_q and the difference in the inductances which is mainly a function of L_d can be different and consequently for a certain current they are maximized at different current angles.

8.3.6 Iron losses

Full iron losses analysis for all final geometries are done here, the results are summarized in Fig. 8.18.

I = 50A, 3000 rpm, fs = 100Hz = 2xfsn, theata (current angle) = 60 Deg.																		
Iron losses (W)																		
rotor					stator back				stator teeth						TOTAL (W)			
machine type	eddy	hyst	High freq. Hyst.	total rotor	eddy	hyst	High freq. Hyst.	total stat. Back	eddy	hyst	High freq. Hyst.	total stat. Teeth		eddy	hyst	High freq. Hyste.	total	
3 Bar. 1 cutoff	333,5	0	120,9	454,4	187,9	209,8	134,0	531,7	186,2	90,8	91,1	368,1		707,6	300,6	346,0	1354,2	
4 Bar.	385,7	0	152,7	538,4	177,9	199,2	160,6	537,7	155,5	87,7	76,8	320,1		719,2	287,0	390,1	1396,3	
4 Bar. 1 cutoff	389,2	0	153,6	542,8	187,9	185,4	129,6	502,8	195,0	87,6	84,3	366,9		772,1	273,0	367,5	1412,6	

Fig. 8.18: Iron losses calculation results for final design geometries at 3000rpm, and nominal current, for different motor regions and different Iron losses sources (calculated based on 350 points per electrical period).

Iron losses are calculated at high speed where the Iron losses become comparable to the copper losses. In the low frequency operation range the most dominant part of losses is the copper (Joule) losses. There is not a big difference between the different models with regard to this. But by increasing the frequency iron losses become comparable to copper losses.

The most dominant part of iron losses is the eddy iron losses. An important fact is related to the distribution of iron losses in the different motor regions. About 40% of the total iron losses are concentrated in the rotor! Normally due to synchronism a constant (DC) magnetic field and consequently low iron losses in the rotor body are expected, except at the rotor surface which interacts with the air gap space harmonics to create changes in flux density is along to the rotor surface.

A qualitative explanation of the iron losses in the rotor body is presented in [3, 33] based on the flux changing in the rotor body. Due to stator slot effect, the flux density is changing in the air gap but these changes are not limited to the rotor surface and are deeply affecting the iron in each rotor segment because the different segments are magnetically separated from each other inside the rotor body or just connected through some saturated ribs.

High flux fluctuation in the rotor body increases the iron losses. One solution is to design each segment position so that the total permeance of a closed flux path within the segment remains constant despite the change of the rotor position relative to the stator [3] (for more analysis refer to chapter 5.3.2).

8.4 Final comparison

Final comparison between different geometries is summarized in Fig. 8.19.

I=50A, current angle = 60 Deg.																	
static situation wm=0, fs=50Hz												non static situation, wm=ws					
												I=50,6A fs=50Hz 1/6 elec. cycle Calc.		Iron losses (W) 3000rpm			
machine type	~current angle theata (e-Deg.)	flux angle beatha (e-Deg.)	B1 peak (T)	I(A) rms ph Y	id (A)	iq (A)	Lmd (mH)	Lmq (mH)	Lmd/Lmq	Lmd-Lmq (mH)	IPF	Teg (Nm)	Tr (%)	eddy	hyste.	High freq. Hyst.	total
3 Bar. 1 cutoff	60	11,1	1,08	50	35,36	61,2	26,29	2,99	8,8	23,3	0,753	152,5	18	707,6	300,6	346,0	1354,2
4 Bar.	60	10,4	1,09	50	35,36	61,2	26,53	2,82	9,4	23,7	0,761	152,8	14	719,2	287,0	390,1	1396,3
4 Bar. 1 cutoff	60	9,8	1,07	50	35,36	61,2	26,22	2,62	10,0	23,6	0,768	153,4	21	772,1	273,0	367,5	1412,6

Fig. 8.19: Main machines specifications comparison table for three different final geometries.

8.5 Ribs

Mechanically strong and self sustained rotor structures are sought because the rotor structures in Fig. 8.9.b are not suitable for high speed application (even for spindle drives with a field-weakening range of 1:5). One way is to introduce some tangential and radial ribs in barriers and connect the segments to each other. Due to the manufacturing advantages the tangential ribs are already introduced in the rotor and their effect on torque was analyzed in chapter 8.2.3 (about 2% reduction in torque and ~5 -10% in torque ripple due to 1mm tangential rib for all barriers end). In this section the radial rib effect on torque is analyzed for the 3 barriers + 1 cut-off rotor structure.

8.5.1 Rib distribution

For a certain total radial rib width, and a distribution of ribs between two barriers of 3 barrier and one cut-off geometry, torque is calculated and the results are shown in Fig. 8.20. The sum of both radial ribs is constant (2mm), but for one of the calculations this width is introduced in the lower barrier and for other calculation it is equally divided between two barriers.

rib comb.	T/pole	dT (%)
no ribe	32,83	0,00
1 width 2mm	31,89	-2,86
2 width 1mm	32,04	-2,39

Fig. 8.20: Radial rib distribution effect on torque for a constant total radial rib width for a 3 barriers and one cut-off geometry.

The more a certain radial rib width is distributed the lower will be the torque reduction. This can be explained by considering the sharing of the flux path, which is saturating the ribs.

In a distributed situation there is a sharing of flux which is passing through the ribs. The flux that is saturating one rib in one barrier is also passing through the other rib in another barrier. But if the total width is introduced in one barrier then more flux is needed for saturation.

For this specific 3 barriers and one cut-off geometry, analysis shows that the difference between two situations is small and with good estimation, it can be concluded that the distribution does not have a significant effect on torque reduction which is almost 2.5% for a 2mm radial rib.

8.5.2 Rib width

Radial rib width effect on torque reduction is shown in Fig. 8.21. By increasing the rib width the required flux to saturate the rib is increasing and therefore the torque is reducing. The relation is linear (for some analytical estimation of torque reduction refer to [2, 32, 33] and chapter 5).

8.5.3 Rib radius

Another parameter that is involved in the dimensioning of the rib is the end part of the rib radius where it connects to the segments (see Fig. 8.22), and can be important for punching tools.

The rib radius effect on torque is analyzed and results are shown in Fig. 8.22. These show that electro-magnetically it does not affect the torque more than 0.5% for a 5mm radius. Increasing this radius mainly increases the q-axis inductance (L_q).

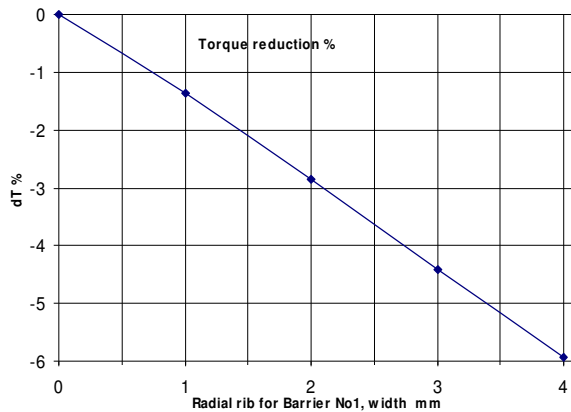


Fig. 8.21: Effect of Radial rib width in the lower barrier on torque in a 3 barriers + 1 cut-off rotor geometry.

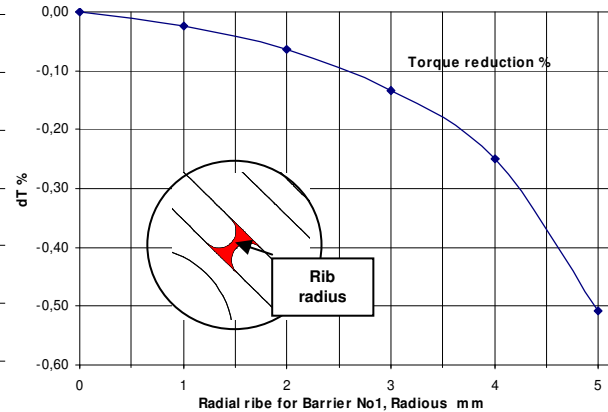


Fig. 8.22: Effect of radial rib (width 2mm) radius on torque, for 3 barriers + 1 cut-off rotor geometry.

8.6 Air gap length

The results from the effect of changing the air gap length on machine characteristics show that reducing the air gap effectively improves the machine performances. In the next sections the effect of air gap on major machine parameters are investigated.

8.6.1 Machine magnetizing inductances

General approach to investigate the effect of air gap length is to study the machine magnetization inductances, and consequently inductance difference and saliency ratio. Such analysis results are shown in Fig. 8.23(left), which are similar to the results in [31].

As expected reducing the air gap length does not change the q-axis inductance, but has a strong impact and increases the d-axis inductance. This is related to the different nature of d- and q-axis flux path material and inductances. The amount of air in the q-axis is proportional to ' $l_a + g$ ' and in the d-axis to ' g '. If the path in the iron is neglected then the q-axis inductance will be inversely proportional to ' $l_a + g$ ' and the d-axis inductance inversely proportional to ' g '. In normal condition ' l_a ' is much bigger than ' g '. Therefore q-axis inductance will not be too sensitive to the air gap length. On the other hand the d-axis inductance is strongly affected by the air gap length.

Reducing air gap length also increases the inductances different and ratio and consequently increasing the machine torque and power factor.

8.6.2 Torque and torque ripple

The effect of air gap length on torque and torque ripple is shown in Fig. 8.23(right). As expected the torque is increased mainly due to the increasing d-axis inductance. But torque ripple also is increasing a little (7% for a decrease in ' g ' from 0.75 to 0.35), mainly due to the air gap Carter's factor. Torque increase is significant, about 20% for a decrease of air gap length from 0.75 to 0.35

mm. At the air gap length of 0.55mm, FEM calculation for torque gives 150 Nm by considering a 3% loss due to the addition of radial ribs. Taking into consideration also a calibration factor of 89% we get a real torque value of 129.5 Nm, which is very close to the same IM nominal torque (131.4 Nm).

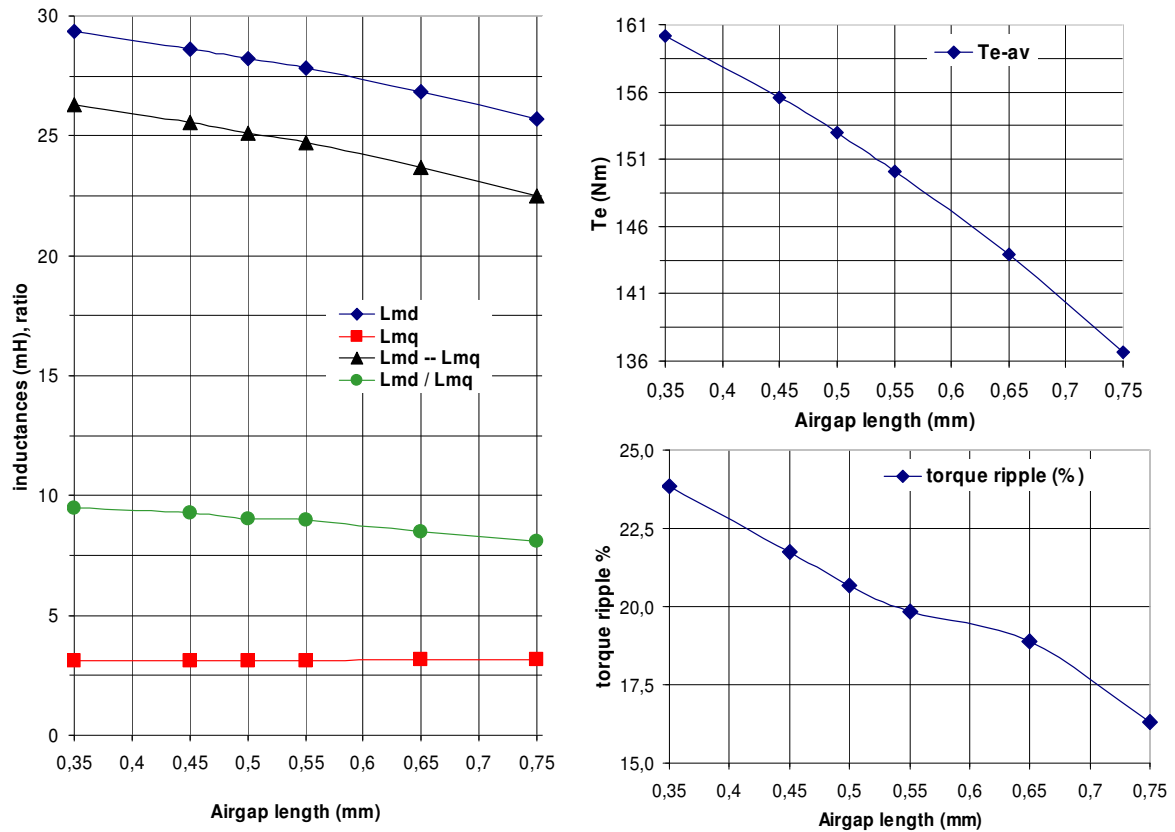


Fig. 8.23: Air gap length 'g' effect on machine magnetization inductances, inductances difference and saliency ratio (left), torque (up-right) and torque ripple (bottom-right). Calculations are based on 350 points in one electrical period and the best current angle of 63 deg. when $g = 0.55\text{mm}$, $I = 50\text{A}$, $f_s = 100\text{Hz}$, $w_r = 0\text{ rpm}$.

8.6.3 IPF

Power factor is strongly dependent on the saliency ratio. By decreasing the air gap length the saliency ratio $\left(\xi = \frac{L_d}{L_q}\right)$ is increased. Therefore an improvement in power factor is expected.

Fig. 8.24 shows the effect of air gap length on the IPF. Power factor is improved but the improvement is not significant.

The reason for this is that the saliency ratio is increased due to increase in the d-axis inductance, but the saliency ratio sensitivity to L_d is not as high as it is to L_q . This means that an improvement in saliency ratio is seeking a lower L_q and not a higher L_d .

The SynRM power factor ($g=0.55$, Fig. 8.24) compared to the power factor of an equivalent IM, which is about 0.85 shows 7.5% lower value when the current angle is set to the maximum torque conditions.

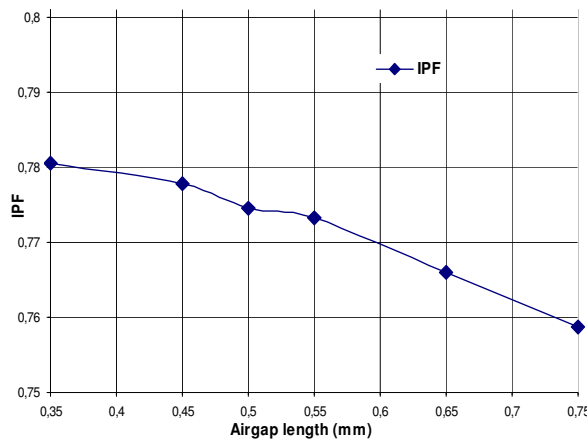


Fig. 8.24: Air gap length 'g' effect on apparent (air gap or internal) power factor (IPF). Calculations are based on 350 points in one electrical period and the best current angle of 63 deg. when $g = 0.55$, $I = 50A$, by using the calculated inductances.

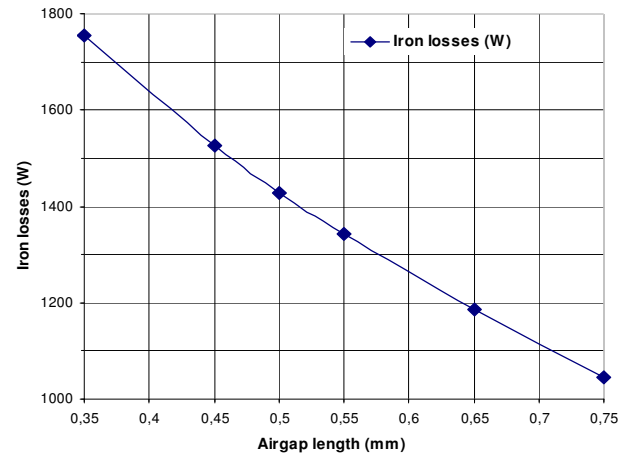


Fig. 8.25: Air gap length 'g' effect on Iron losses. Calculations are based on 350 points in one electrical period and the best current angle of 63 deg. when $g = 0.55$, $I = 50A$, $f_s = 100Hz$, $w_r = 3000$ rpm.

Normally the SynRM has a PF lower than the IM for the same frame size. To improve the power factor in the SynRM somehow the q-axis flux must be reduced, ie. the q-axis inductance by increasing should be reduced the insulation ratio in the q- and d-axis. Another way is to compensate the q-axis flux by inserting a small permanent magnet at the rotor structure. Such kind of technique is discussed in [3]. This kind of motor is named permanent magnet assistant SynRM, PMSynRM.

8.6.4 Iron losses

If the air gap length is reduced, two major machine performance parameters are changed. First the Carter's factor of the air gap is increased and secondly the flux density in all part of machine is increased. The first item indirectly increases the torque ripple and therefore the flux fluctuation is increased also. All these effects cause increased iron losses.

An iron losses calculation for different air gap length is shown in Fig. 8.25, and confirms the above discussions. Increasing the iron losses by reducing the air gap length maybe is considered as a draw back. A complementary analysis regarding the overall machine efficiency can present more detailed insight into the effect of air gap length on machine performance.

8.6.5 Efficiency

Result from the calculation of efficiency for different air gap lengths is shown in Fig. 8.26. Clearly it shows that the reduction of air gap length from a primary value of 0.55 to 0.45mm is reducing the overall efficiency by just 0.2% with the same current angle. This means that the

torque, see Fig. 8.23, and the losses are increasing in the same manner if the air gap length is reduced.

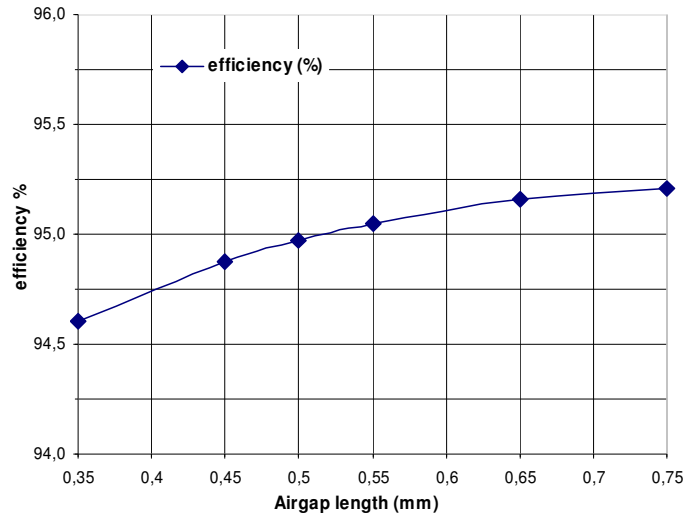


Fig. 8.26: Air gap length 'g' effect on overall machine efficiency. Calculations are based on 350 points in one electrical period and the best current angle of 63 deg. when $g = 0.55$, $I = 50\text{A}$, $f_s = 100\text{Hz}$, $w_r = 3000\text{ rpm}$. Only copper and iron losses are considered.

8.7 Over load capacity

The over load capacity of the SynRM is discussed deeply in [33]. Here just some main results are presented.

The over load capacity is affecting the machine geometric and operation optimization, because with regard to the definition for optimization of the nominal operating point there are two different bounding situations.

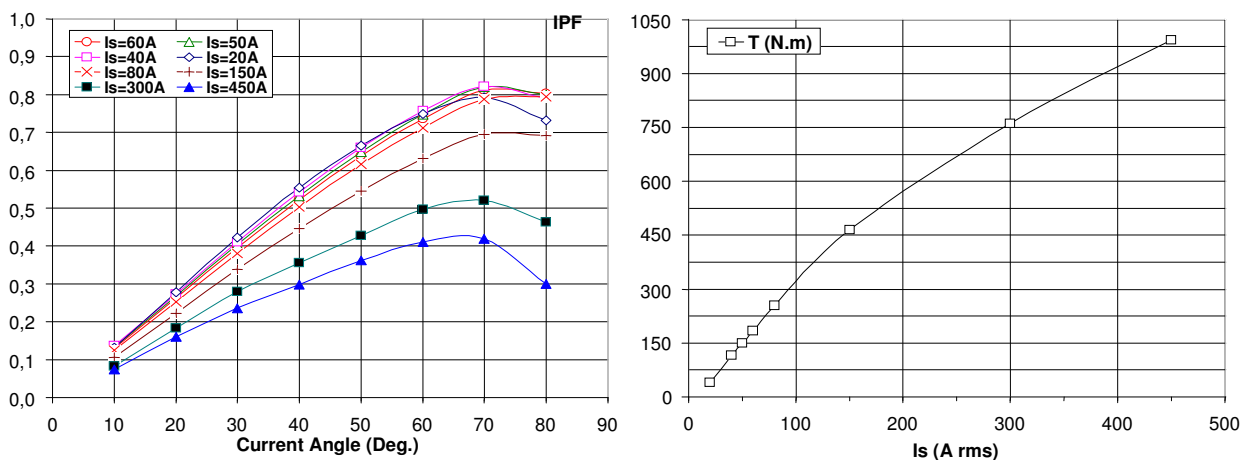


Fig. 8.27: Maximum air gap electromechanical torque as function of stator current (right) and power factor as function of current angle and stator current as parameter.

The optimization can be based on continuous maximum torque or a pulsed load operation point [33]. If the inverter size for variable speed operation is also considered then the power factor must be included, because it affects the required kVA [33].

Result from an over load study is shown in Fig. 8.27. Increasing the stator current shows that the torque versus current follows an almost linear relationship up to a very high over load condition of about 9 times assuming the current angle in this situation to be around 62 deg., see Fig. 8.27 (right). The nominal current is 50A and power factor is around 0.75. However for this heavily over loaded condition the power factor is dropped by 50%, see Fig. 8.27 (left).

If the power factor for over load capacity is also considered then a 3 times over load is achievable without affecting the power factor, see Fig. 8.27 (left) for 150 A stator current. Actually for this over load condition terminal power factor can be improved a little [33].

Compare to the induction machines (normally 2 p.u.) the SynRM shows higher over load capacity.

9 CONCLUSIONS

This report has presented the behavior of the SynRM and its nature based on available literatures and publications, materials and FEM sensitivity analysis studies.

In chapter 2 a basic principles and motor model of the machine have been developed based on Park's equations for traditional salient pole synchronous machines. Through chapters 3 and 4 the developing history and some comparison between SynRM and IM, different type of the machine rotor geometry and some basic control concepts are investigated.

In chapter 5, classified parameters descriptions involved in SynRM performance and their general effect on SynRM have been investigated and presented.

The most important design parameters are determined and generalized, under the design parameters category. These parameters are strong tools to characterize the rotor geometry, and they can generally describe the rotor structures and its effect on machine performance.

In Chapter 6 a suitable combined theoretical and finite element method (procedure) for SynRM optimal geometry is developed.

The main parameters involved in the rotor geometry, ie. insulation ratio in the d- and q-axis, rotor slot pitch and number of barriers (design parameters), are used by this procedure simultaneously with optimal distribution law to minimize the going through component of the q-axis flux for each selection of design parameters, and all geometrical parameters for each barrier are calculated.

Finally in chapters 7 and 8 the generated geometry of each set of design parameters is modeled with suitable FE software to evaluate the target variables.

In this manner a fast combined theoretical and finite-element rotor design procedure, see chapter 6, for a certain stator is developed that mainly focuses on torque maximization and reducing the torque ripple to a practical acceptable level. Also the numbers of barriers are reduced to the minimum number in order to make it as manufacturing friendly as possible.

	<p style="text-align: center;">MSc Final Project Report</p> <p style="text-align: center;">ABB Corporate Research & KTH</p>	
Doc. title	By: Reza Rajabi Moghaddam	Page
Synchronous Reluctance Machine Design		80

In chapter 7 pure geometrical parameter sensitivity analysis for the simplest rotor geometries have been done and compared with the combined theoretical-FEM method to and confirm the results.

In chapter 8 a full optimization for maximum torque, minimum torque ripple, and minimum number of barriers is done.

Finally other design parameters like ribs ,air gap ,over load capacity, iron losses and power factor have been investigated and related sensitivity analysis have been conducted for the final geometries.

10 FUTURE WORK

Future work can be concentrated on the following subjects:

- 1- Building prototype and measurement.
- 2- Study and develop more effective procedures for torque ripple reduction.
- 3- Iron losses and their effect on machine performance, especially rotor iron losses.
- 4- Due to lack of any starting torque and also stability issue SynRM is suitable for closed loop control variable speed drives. Different control schemes and machine behavior under close loop control can be another area of study.
- 5- By adding some asynchronous torque to the SynRM characteristics by introducing a rotor cage in the air barriers, starting torque can be obtained. The resultant machine characteristic study can be another future work.
- 6- Fault effect analysis of the SynRM under different operation conditions is important from protection and operation point of view, and is another study area.
- 7- Developing a thermal model.
- 8- Theoretical treatment for overall optimization.
- 9- Field-weakening capability and techniques and high speed applications.
- 10- Potential vehicle applications ie. HEV.
- 11- Flux fluctuation inside the rotor body and its effect on torque ripple and iron losses.

11 REFERENCES

- [1] A. VAGATI, M. PASTORELLI, P. GUGLIELMI, A. CANOVA, “*Synchronous reluctance motor based sensorless drive for general purpose application*”, Dipartimento di Ingegneria Elettrica Industriale, Politecnico di Torino, Corso Duca degli Abruzzi, 24, I-10129 Torino (Italy).
- [2] A. Vagati, G. Franceschini, I. Marongiu, G.P. Trogia, “*Design criteria of high performance synchronous reluctance motors*”, Industry Applications Society Annual Meeting, 1992., Conference Record of the 1992 IEEE 4-9 Oct. 1992 Page(s):66 - 73 vol.1.
- [3] A. Fratta, A. Vagati, F. Villata, “*On the evolution of A.C. machines for spindle drive applications*”, Industry Applications, IEEE Transactions on, Volume 28, Issue 5, Sept.-Oct. 1992 Page(s):1081 – 1086.
- [4] A. Vagati, A. Fratta, G. Franceschini, P. Rosso, “*AC motors for high-performance drives: a design-based comparison*”, Industry Applications, IEEE Transactions on, Volume 32, Issue 5, Sept.-Oct. 1996 Page(s):1211 – 1219.
- [5] J.J. Germishuizen, F.S. Van der Merwe, K. Van der Westhuizen, M.J. Kamper, “*Performance comparison of reluctance synchronous and induction traction drives for electrical multiple units*”, Industry Applications Conference, 2000. Conference Record of the 2000 IEEE, Volume 1, 8-12 Oct. 2000 Page(s):316 - 323 vol.1.
- [6] F. Parasiliti, M. Villani, “*Synchronous reluctance motors design and performance prediction using an analytical procedure*”, Electrical Engineering and Electromagnetics, WIT Press, 2003, ISBN- 1-85312- 981-X, pp. 147-156.
- [7] F. Parasiliti, M. Tursini, M. Villani, “*Design of synchronous reluctance motors by finite element analysis and optimization algorithm Prototype and tests*”, Department of Electrical and Information Engineering, University of 'Aquila, 67100 Poggio di Roio, L'Aquila, Italy, July 15th 2006.
- [8] Rae Hwa Lee, Min Myung Lee, Jung Ho Lee, “*Rotor design functional standard of Synchronous Reluctance Motor according to torque per volume using FEM & SUMT*”, Manuscript received June 30, 2006.²
- [9] T. Matsuo, T. A. Lipo, “*Field oriented control of synchronous reluctance machine*”, Power Electronics Specialists Conference, 1993. PESC '93 Record, 24th Annual IEEE, 20-24 June 1993 Page(s):425 - 431.
- [10] P. L. Alger, “*The Nature of Polyphase Induction Machines*”, New York: Wiley, 1951.
- [11] A. Boglietti, A. Cavagnino, M. Pastorelli, A. Vagati, “*Experimental comparison of induction and synchronous reluctance motors performance*”, Industry Applications Conference, 2005. Fourtieth IAS Annual Meeting, Conference Record of the 2005, Volume 1, 2-6 Oct. 2005 Page(s):474 - 479 Vol. 1.

² This work was financially supported by MOCIE through IERC program. R.H Lee Author is with the Hanbat National University, Dukmyung-Dong, Yuseong-Gu, Daejeon, 305-719, KOREA. (phone: 82-42-821-1626, Fax: 82-42-821-1088, e-mail: naezone@hanmail.net), M.M. Lee Author is with the Hanbat National University, Dukmyung-Dong, Yuseong-Gu, Daejeon, 305-719, KOREA. (phone: 82-42-821-1626) J.H. Lee Author is with the Hanbat National University, Dukmyung-Dong, Yuseong-Gu, Daejeon, 305-719, KOREA. (phone: 82-42-821-1098, e-mail: limoter@hanbat.ac.kr).

- [12] J. Haataja, “A comparative performance study of four-pole induction motors and synchronous reluctance motors in variable speed drives”, Lappeenranta University of Technology, ISBN 951-764-772-7, ISSN 1456-4491, Lappeenranta teknillinen yliopisto, Digipaino 2003.
- [13] Jung-Min Park, Seong-June Park, Min-Myung Lee, Jang-Sung Chun, Jung-Ho Lee, “Rotor Design on Torque Ripple Reduction for a Synchronous Reluctance Motor with concentrated winding using response surface methodology”, XVII International Conference on Electrical Machines, September 2-5, 2006, Chania, Crete Island, Greece.
- [14] A. Consoli, G. Scarcella, G. Scelba, A. Testa, D. Triolo, “Using Salient AC Machines as Virtual Resolvers”, XVII International Conference on Electrical Machines, September 2-5, 2006, Chania, Crete Island, Greece.
- [15] F. Magnussen, “Theoretical analysis and design of motors for variable speed drives”, ABB Technical Report, SECRC/PT/TR-06/039, 17th February 2006.
- [16] F. Magnussen, “Measurements of motors for variable speed drives”, ABB Technical Report, SECRC/PT/TR-06/040, 17th February 2006.
- [17] J. Malan, M.J. Kamper, “Performance of a hybrid electric vehicle using reluctance synchronous machine technology”, Industry Applications, IEEE Transactions on, Volume 37, Issue 5, Sept.-Oct. 2001 Page(s):1319 – 1324.
- [18] M.J. Kamper, F.S. Van der Merwe, S. Williamson, “Direct finite element design optimization of the cage less reluctance synchronous machine”, Energy Conversion, IEEE Transactions on, Volume 11, Issue 3, Sept. 1996 Page(s):547 – 555.
- [19] J. Malan, M.J. Kamper, P.N.T. Williams, “Reluctance synchronous machine drive for hybrid electric vehicle”, Industrial Electronics, 1998. Proceedings. ISIE '98. IEEE International Symposium on, Volume 2, 7-10 July 1998 Page(s):367 - 372 vol.2.
- [20] T. J. E. Miller, A. Hutton, C. Cossar, D.A. Staton, “Design of a synchronous reluctance motor drive”, Industry Applications, IEEE Transactions on, Volume 27, Issue 4, July-Aug. 1991 Page(s):741 – 749.
- [21] T. A. Lipo, “Synchronous reluctance machines - a viable alternative for AC drives? ”, Electric Machines and Power Systems, Vol. 19, no. 6, pp. 659-671. 1991.
- [22] J. G. W. West, “DC, induction, reluctance and PM motors for electric vehicles”, Power Engineering Journal, Volume 8, Issue 2, April 1994 Page(s):77 – 88.
- [23] D. A. Staton, T. J. E. Miller, S. E. Wood, “Maximizing the saliency ratio of the synchronous reluctance motor”, Electric Power Applications, IEE Proceedings B [see also IEE Proceedings-Electric Power Applications], Volume 140, Issue 4, July 1993 Page(s):249 – 259.
- [24] A. Boglietti, A. Cavagnino, M. Pastorelli, D. Staton, A. Vagati, “Thermal analysis of induction and synchronous reluctance motors”, Industry Applications, IEEE Transactions on, Volume 42, Issue 3, May-June 2006 Page(s):675 – 680.
- [25] T. Matsuo, A. El-Antably, T.A. Lipo, “A new control strategy for optimum-efficiency operation of a synchronous reluctance motor”, Industry Applications, IEEE Transactions on, Volume 33, Issue 5, Sept.-Oct. 1997 Page(s):1146 - 1153.

- [26] F. Fernandez-Bernal, A. Garcia-Cerrada, R. Faure, “*Efficient control of reluctance synchronous machines*”, Industrial Electronics Society, 1998. IECON '98. Proceedings of the 24th Annual Conference of the IEEE, Volume 2, 31 Aug.-4 Sept. 1998 Page(s):923 - 928 vol.2.
- [27] B. J. Chalmers, L. Musaba, “*Design and field-weakening performance of a synchronous reluctance motor with axially laminated rotor*”, Industry Applications, IEEE Transactions on, Volume 34, Issue 5, Sept.-Oct. 1998 Page(s):1035 – 1041.
- [28] A. Vagati, “*The synchronous reluctance solution: a new alternative in A. C. drives*”, Proc IEEE IECON'94 (Bologna), vol. 1, pp.1-13, 1994.
- [29] T. Matsuo, T. A. Lipo, “*Rotor design optimization of synchronous reluctance machine*”, Energy Conversion, IEEE Transactions on, Volume 9, Issue 2, June 1994 Page(s):359 – 365.
- [30] J. K. KOSTKO: “*Polyphase reaction synchronous motors*”, Journal Amer. Inst. Elect. Engrs, 1923, Vol 42, pp. 1162-1168.
- [31] M.J. Kamper and A.F. Volschenk, “Effect of rotor dimensions and cross magnetization on Ld and Lq inductances of reluctance synchronous machine with cage less flux barrier rotor”, IEE Proc.-Electr. Power Appl., vol. 141, no. 4, July 1994.
- [32] A. Fratta, A. Vagati, F. Villata, G. Franceschini, C. Petrache, “*Design comparison between induction and synchronous reluctance motors*”, ICEM September 1994, Vol. 3, pp. 329-334.
- [33] T. A. Lipo, T. J. E. Miller, A. Vagati, I. Boldea, L. Malesani, and T. Fukao, “*Synchronous reluctance drives*” tutorial presented at IEEE-IAS Annual Meeting, Denver, CO, Oct. 1994.
- [34] I. Boldea, “*Reluctance Synchronous Machines and Drives*”, Clarendon Press, Oxford 1996.
- [35] Jung-Min Park; Seong-June Park; Min-Myung Lee; Jang-Sung Chun; Jung-Ho Lee; “*Rotor Design on Torque Ripple Reduction for a Synchronous Reluctance Motor with concentrated winding using response surface methodology*”, XVII International Conference on Electrical Machines, September 2-5, 2006, China, Crete Island, Greece.
- [36] H. Kiriya, S. Kawano, Y. Honda, T. Higaki, S. Morimoto, Y. Takeda, “*High performance synchronous reluctance motor with multi-flux barrier for the appliance industry*”, Industry Applications Conference, 1998. Thirty Third IAS Annual Meeting, 1998 IEEE, Volume 1, 12-15 Oct. 1998 Page(s):111 - 117 vol.1.
- [37] A. Vagati, “*Synchronous Reluctance Electrical Motor having a low torque ripple design*”, USA patent No. 5,818,140, Oct. 6, 1998.
- [38] C. Sadarangani, “*Electrical machines: Design and Analysis of induction and permanent magnet motors*”, division of electrical machines and power electronics, school of electrical engineering, Royal institute of technology (KTH) Stockholm, Sweden, Feb., 2006.
- [39] N. Bianchi, S. Bolognani, D. Bon, M. Dai Pre', “*Torque Harmonic Compensation in a Synchronous Reluctance Motor*”, 37th IEEE Power Electronics Specialists Conference, June 18 - 22, 2006, Jeju, Korea.

	<h1 style="text-align: center;">MSc Final Project Report</h1> <p style="text-align: center;">ABB Corporate Research & KTH</p>	
Doc. title	By: Reza Rajabi Moghaddam	Page
Synchronous Reluctance Machine Design		84

- [40] N. Bianchi, S. Bolognani, D. Bon, M. Dai Pre', "Rotor flux-barrier design for torque ripple reduction in synchronous reluctance motors", Department of Electrical Engineering, University of Padova, Italy, 2006, 1-4244-0365-0/06/\$20.00 (c) 2006 IEEE.
- [41] A. Fratta, G. P. Troglia, A. Vagati, F. Villata, "Evaluation of torque ripple in high performance synchronous reluctance machines", IEEE-IAS Annual meeting, Toronto (Canada), October 1993, Vol. I, pp. 163-170.
- [42] L. Xu, X. Xu, T.A. Lipo and D. W. Novotny, "Vector control of a synchronous reluctance motor including saturation and iron loss", IEEE Trans. Industry Applications., vol. 27, no. 5, pp. 977-987, Sept. 1991.
- [43] A. Fratta, A. Vagati: "Synchronous reluctance vs. induction motor: a comparison", Proceedings Intelligent Motion (Nuremberg), April 1992, pp. 179-186.
- [44] Vagati, A.; Pastorelli, M.; Francheschini, G.; Petrache, S.C.; "Design of low-torque-ripple synchronous reluctance motors", Industry Applications, IEEE Transactions on, Volume 34, Issue 4, July-Aug. 1998 Page(s):758 – 765.
- [45] T. Fukami, M. Momiyama, K. Shima, R. Hanaoka, S. Takata, "Performance of a Dual-Winding Reluctance Generator with a multiple-Barrier rotor", Department of Electrical and Electronic Engineering, Kanazawa Institute of Technology, Ishikawa 921-8501, Japan, June 30, 2006³.
- [46] I. V. Hrabovcova, J. Pyrhonen, J. Haataja, "Reluctance Synchronous motor (RSM) and its performances", Lappeenranta University of Technology, May 2005.
- [47] Fratta A., Vagati A.: "Axially laminated reluctance motor: an analytical approach to the magnetic behaviour", ICEM, Pisa, Italy, 12-14 Sept. 1988, pp. 1-6.
- [48] I. Marongiu, A. Vagati, "Improved modelling of a distributed anisotropy synchronous reluctance machine", IEEE-IAS, 1991, Dearborn, USA, October 1991, pp. 238-243.
- [49] A. Fratta, A. Vagati, and F. Villata, "AC spindle drives: A unified approach to the field-weakening behaviour," in Proc. Int. Motor-Con Con\$, Munich, Germany, June 1988, pp. 44-56.

³ This work was partially supported by "High-Tech Research Center" Project for Private Universities: matching fund subsidy from Ministry of Education, Culture, Sports, Science and Technology, Japan, 2004-2008. The authors are with the (e-mail: fukami@neptune.kanazawa-it.ac.jp).

12 APPENDICES

12.1 Appendix A: Different possible operating points for SynRM

In the following analysis the ideal situation is assumed. Frequency is also assumed constant for all operating points. For details see Figs. 12.1, 12.2 and 12.6.

12.1.1 Comparison of point (A): max. T/A and (B): max. T/V for constant current

Consider two operating points (A) and (B) in Figs. 12.1 and 12.2 (see also Fig. 4.1 and Appendix B). Assume also that the stator current for both points is equal. Then the question is: Which point gives higher torque, and what are the voltages at these two operation conditions?

a) Torque comparison

Torque at point (A) can be calculated according to the equation 2.12 and $\theta_A = \frac{\pi}{4}$ as follows:

$$T_A = k \cdot (L_{dm} - L_{qm}) \cdot I_m^2 \quad (A.1)$$

Similarly Torque at point (B) can be calculated according to the equation 2.14 and $\delta_B = \frac{\pi}{4}$ as follows:

$$T_B = k \cdot \left(\frac{1}{L_{qm}} - \frac{1}{L_{dm}} \right) \cdot \left(\frac{E_{mB}}{\omega} \right)^2 \quad (A.2)$$

On the other hand at point (B) the internal voltage related factor $\left(\frac{E_{mB}}{\omega} \right)$ can be calculated according to the stator current as follows, using eqs. 2.15 and 4.1:

$$\begin{aligned}
 \left(\frac{E_{mB}}{\omega} \right)^2 &= (L_{dm} I_{dmB})^2 + (L_{qm} I_{qmB})^2 = \\
 &= 2 \cdot (L_{dm} I_{dmB})^2 = \left(\frac{I_{qmB}}{I_{dmB}} = \tan \theta_B = \text{using eq. 2.15} = \frac{L_{dm}}{L_{qm}} \right) \\
 &= 2 \cdot \left(L_{dm} I_m \cdot \frac{L_{qm}}{\sqrt{L_{dm}^2 + L_{qm}^2}} \right)^2 = 2 \cdot \frac{I_m^2 \cdot L_{dm}^2 \cdot L_{qm}^2}{L_{dm}^2 + L_{qm}^2} \quad (A.3)
 \end{aligned}$$

Introducing eq. A.3 to A.2 will give:

$$T_B = k \cdot (L_{dm} - L_{qm}) \cdot I_m^2 \cdot \frac{\overbrace{2}^a}{\frac{L_{dm}}{L_{qm}} + \frac{L_{qm}}{L_{dm}}} \quad (A.4)$$

In eq. A.4 factor (a) is clearly less than one, and comparing eqs. A.1 and A.4 shows that $T_A \geq T_B \Big|_{I_{mA}=I_{mB}}$.

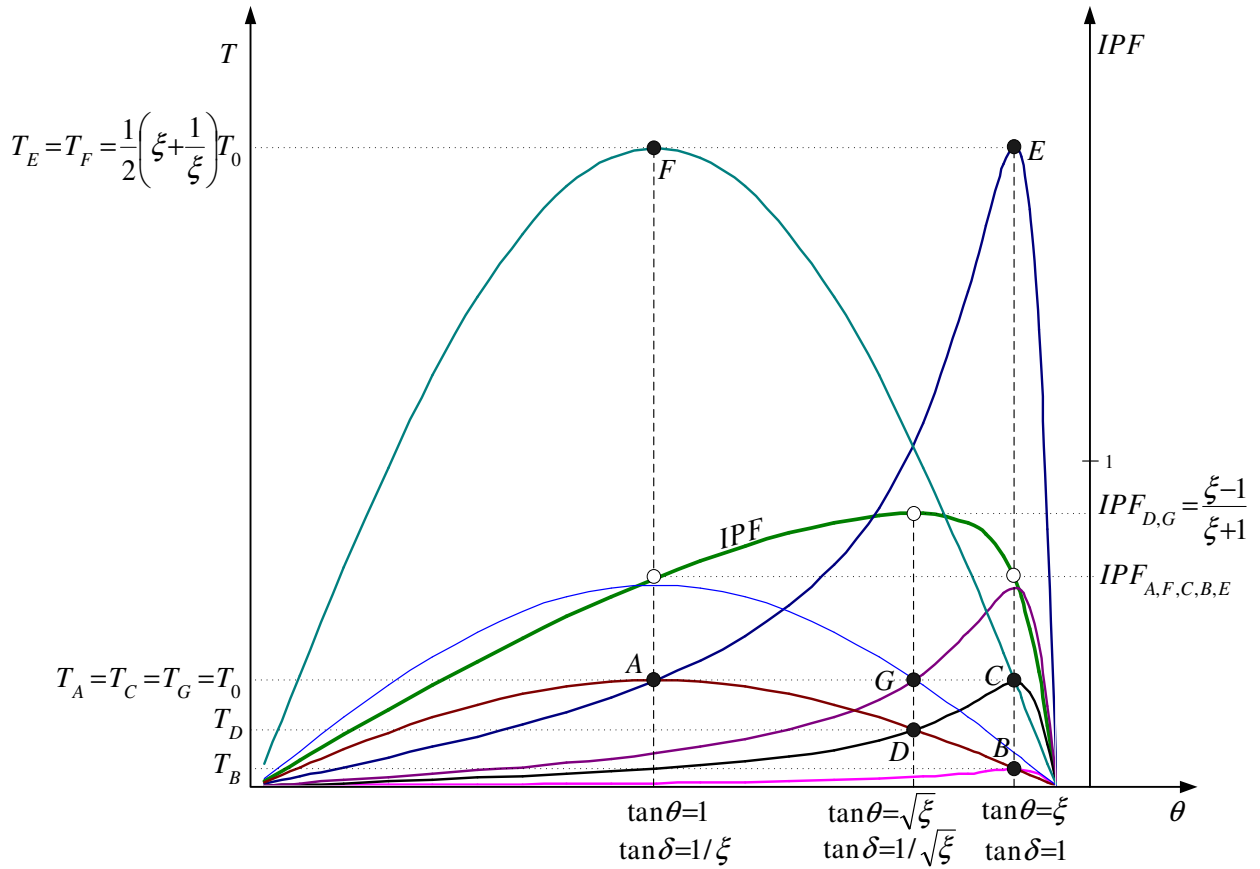


Fig. 12.1: Possible operating points for SynRM, see also Fig. 12.2 and eqs. D.1 and D.2.

b) Voltage comparison

Point (B) voltage can be calculated according to eq. A.3. Voltage at point (A) can be written as follows:

$$\begin{aligned}
 \left(\frac{E_{mA}}{\omega} \right)^2 &= (L_{dm} I_{dmA})^2 + (L_{qm} I_{qmA})^2 = \\
 &= \left(L_{dm} \frac{I_m}{\sqrt{2}} \right)^2 + \left(L_{qm} \frac{I_m}{\sqrt{2}} \right)^2 = \left(\frac{I_{qmA}}{I_{dmA}} = \tan \theta_A = 1 \Rightarrow I_{dmA} = I_{qmA} = \frac{I_m}{\sqrt{2}} \right) \\
 &= (L_{dm}^2 + L_{qm}^2) \cdot \frac{I_m^2}{2} \quad (A.5)
 \end{aligned}$$

By comparing eqs. A.3 and A.5 and adding some simple mathematical manipulations we can show that always $E_{mA} \geq E_{mB} \big|_{I_{mA}=I_{mB}}$.

c) Internal power factor comparison

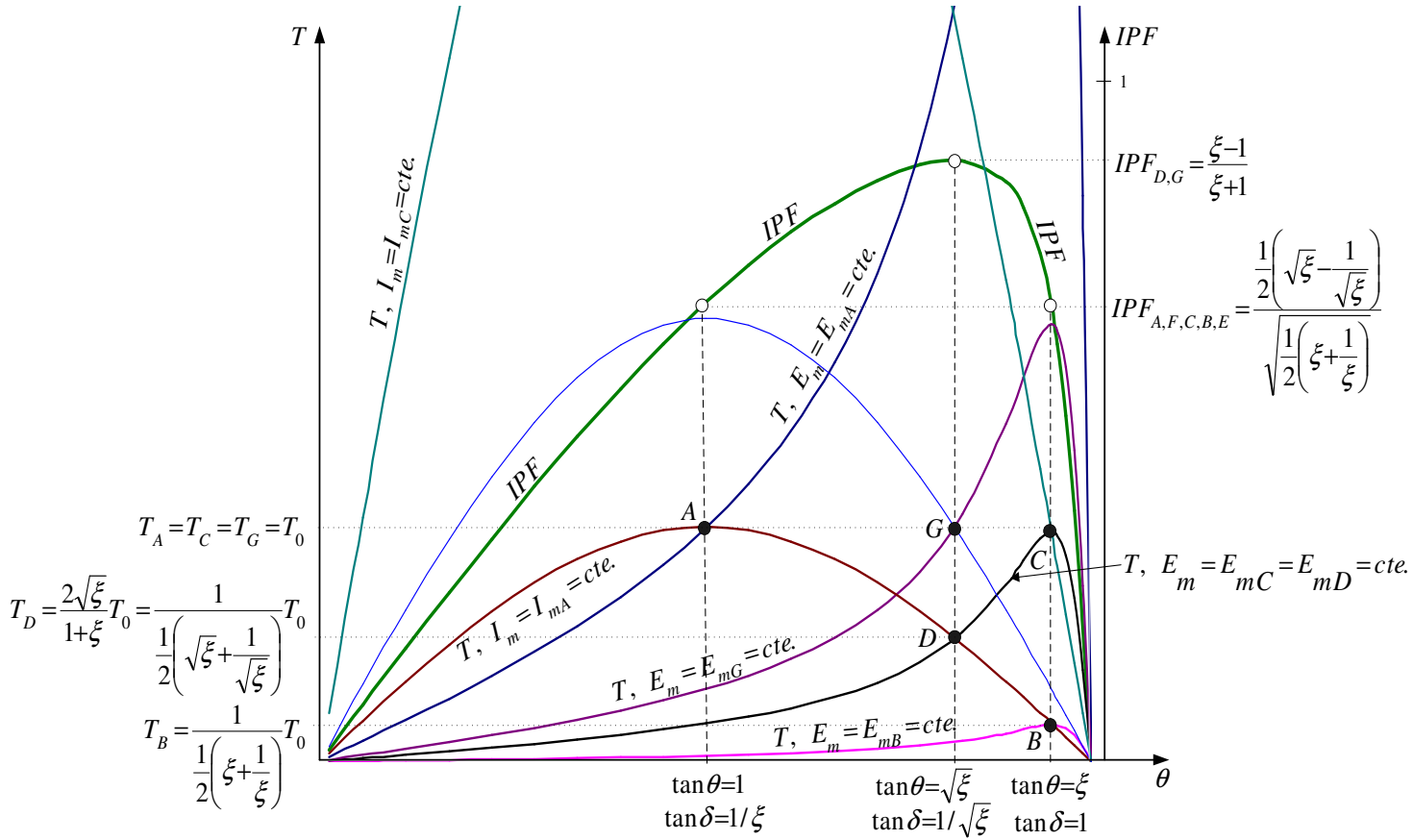


Fig. 12.2: Possible operating points for SynRM, see also Fig. 12.1 and eqs. D.1 and D.2.

The IPF for both operating points can be calculated according eq. 2.7 and using eq. 2.15 as follows:

$$IPF_A = IPF_B = \frac{\xi - 1}{\sqrt{2(\xi^2 + 1)}} = \frac{\frac{1}{2} \left(\sqrt{\xi} - \frac{1}{\sqrt{\xi}} \right)}{\sqrt{\frac{1}{2} \left(\xi + \frac{1}{\xi} \right)}} \quad (A.6)$$

d) Power comparison

The power ratio for the two operating points is as following, using eqs. A.3, A.6 and A.5:

$$\frac{P_A}{P_B} = \frac{k \cdot E_{mA} \cdot I_m \cdot \cos \varphi_A}{k \cdot E_{mB} \cdot I_m \cdot \cos \varphi_B} = \frac{E_{mA}}{E_{mB}} = \frac{L_{dm}^2 + L_{qm}^2}{2L_{dm}L_{qm}} = \frac{1}{2} \left(\xi + \frac{1}{\xi} \right) \quad (A.7)$$

e) Torque comparison

The torque ratio for the two operating point is as following, using eqs. A.1 and A.4:

$$\frac{T_A}{T_B} = \frac{L_{dm}^2 + L_{qm}^2}{2L_{dm}L_{qm}} = \frac{1}{2} \left(\xi + \frac{1}{\xi} \right) \quad (A.8)$$

	MSc Final Project Report ABB Corporate Research & KTH	
Doc. title	By: Reza Rajabi Moghaddam	Page
Synchronous Reluctance Machine Design		88

12.1.2 Comparison of point (A): min. Amp. and (C): min. voltage for certain torque

If the same amount of torque as in point (A) with minimum voltage is considered then point (C) will be the new operating point, see Fig. 12.2. In point (C): $\tan \delta_C = 1$ and $\tan \theta_C = \xi$.

a) Current comparison

Using eq. A.4 for point (C) will give the torque as follows for this point:

$$T_C = k \cdot (L_{dm} - L_{qm}) \cdot I_{mC}^2 \cdot \frac{2}{\frac{L_{dm}}{L_{qm}} + \frac{L_{qm}}{L_{dm}}} \quad (A.9)$$

By comparing this equation and eq. A.1, for current ratio for points (A) and (C) we can write:

$$T_A = k \cdot (L_{dm} - L_{qm}) \cdot I_{mA}^2 = T_0 = k \cdot (L_{dm} - L_{qm}) \cdot I_{mC}^2 \cdot \frac{2}{\frac{L_{dm}}{L_{qm}} + \frac{L_{qm}}{L_{dm}}} = T_C \quad \Rightarrow$$

$$\frac{I_{mA}}{I_{mC}} = \frac{1}{\sqrt{\frac{1}{2} \left(\xi + \frac{1}{\xi} \right)}} \quad (A.10)$$

b) Voltage comparison

Similar to point (B) the voltage at point (C) is as follows, see eq. A.3:

$$\left(\frac{E_{mC}}{\omega} \right)^2 = 2 \cdot \frac{I_{mC}^2 \cdot L_{dm}^2 \cdot L_{qm}^2}{L_{dm}^2 + L_{qm}^2} \quad (A.11)$$

Therefore the voltage ratio can be written as, see eqs. A.5, A.10 and A.11:

$$\frac{E_{mA}}{E_{mC}} = \frac{1}{2} \cdot \left(\frac{L_{dm}^2 + L_{qm}^2}{L_{dm} \cdot L_{qm}} \right) \cdot \left(\frac{I_{mA}}{I_{mC}} \right) = \sqrt{\frac{1}{2} \left(\xi + \frac{1}{\xi} \right)} \quad (A.12)$$

c) Power comparison

Using eqs. A.10, A.12 and A.6 (IPFA=IPFC, see Fig.7.1) will give the power ratio as follows:

$$\frac{P_A}{P_C} = \frac{k \cdot E_{mA} \cdot I_{mA} \cdot \cos \varphi_A}{k \cdot E_{mC} \cdot I_{mC} \cdot \cos \varphi_C} = \frac{E_{mA}}{E_{mC}} \cdot \frac{I_{mA}}{I_{mC}} = 1 \quad (A.13)$$

12.1.3 Comparison of point (A): max. T/A and (D): max. IPF for certain current

If the same amount of current as in point (A) with maximum power factor is considered then point (D) will be the new operating point. In point (D): $\tan \delta_D = 1/\sqrt{\xi}$ and $\tan \theta_D = \sqrt{\xi}$, see eq. 2.8. Therefore: $\sin \theta_D = \sqrt{\frac{\xi}{1+\xi}}$ & $\cos \theta_D = \sqrt{\frac{1}{1+\xi}}$.

a) Torque and power comparison

Torque in point (D) can be calculated as follows, see eq. 2.12:

$$\begin{aligned}
 T_D &= k \cdot (L_{dm} - L_{qm}) \cdot I_m^2 \cdot \sin(2\theta_D) = \\
 &= k \cdot (L_{dm} - L_{qm}) \cdot I_m^2 \cdot 2 \cdot \sin \theta_D \cdot \cos \theta_D = \\
 &= k \cdot (L_{dm} - L_{qm}) \cdot I_m^2 \cdot \left(\frac{1}{\frac{1}{2} \left(\sqrt{\xi} + \frac{1}{\sqrt{\xi}} \right)} \right) \quad (A.14)
 \end{aligned}$$

The torque ratio will be according to the following equation, see eqs. A.1 and A.14:

$$\frac{T_A}{T_D} = \frac{1+\xi}{2\sqrt{\xi}} = \frac{1}{2} \left(\sqrt{\xi} + \frac{1}{\sqrt{\xi}} \right) = \frac{P_A}{P_D} \left(= \frac{T_A \cdot \omega}{T_D \cdot \omega} \right) \quad (A.15)$$

b) Voltage comparison

The internal voltage related factor $\left(\frac{E_{mD}}{\omega} \right)$ can be calculated according to the stator current as follows, using eqs. 2.15 and 4.1, note that $\sin \theta_D = \sqrt{\frac{\xi}{1+\xi}}$, $\cos \theta_D = \sqrt{\frac{1}{1+\xi}}$:

$$\begin{aligned}
 \left(\frac{E_{mD}}{\omega} \right)^2 &= (L_{dm} I_{dmD})^2 + (L_{qm} I_{qmD})^2 = \\
 &= (L_{dm} \cdot I_m \cdot \cos \theta_D)^2 + (L_{qm} \cdot I_m \cdot \sin \theta_D)^2 = \\
 &= (L_{dm} L_{qm}) \cdot I_m^2 \quad (A.16)
 \end{aligned}$$

Using eqs. A.5 and A.16 will give the voltage ratio as follows:

$$\frac{E_{mA}}{E_{mD}} = \sqrt{\frac{1}{2} \left(\xi + \frac{1}{\xi} \right)} \quad (A.17)$$

c) Power factor comparison

By using eqs. 2.8 and A.6, power factors ratio can be written as following:

$$\frac{IPF_A}{IPF_D} = \frac{\frac{\xi - 1}{\sqrt{2(\xi^2 + 1)}}}{\frac{\xi - 1}{\xi + 1}} = \frac{\frac{1}{2} \left(\sqrt{\xi} + \frac{1}{\sqrt{\xi}} \right)}{\sqrt{\frac{1}{2} \left(\xi + \frac{1}{\xi} \right)}} \quad (A.18)$$

12.1.4 Comparison of point (A): min. current and point (G): max. IPF or min. kVA for certain torque

If the same amount of torque as in point (A) with maximum power factor or minimum kVA is considered then point (G) will be the new operating point. In point (G): $\tan \delta_G = 1/\sqrt{\xi}$ and $\tan \theta_G = \sqrt{\xi}$, see eq. 2.8. Therefore: $\sin \theta_G = \sqrt{\frac{\xi}{1+\xi}}$ & $\cos \theta_G = \sqrt{\frac{1}{1+\xi}}$.

a) Current comparison

Similar to point (D) the torque equation for point (G) can be written as, see eq. A.14:

$$T_G = k \cdot (L_{dm} - L_{qm}) \cdot I_{mG}^2 \cdot \left(\frac{2\sqrt{\xi}}{1+\xi} \right) = T_0 \quad (A.19)$$

Combining this equation with eq. A.1 will give the current ratio as following:

$$\frac{I_{mA}}{I_{mG}} = \frac{1}{\sqrt{\frac{1}{2} \left(\sqrt{\xi} + \frac{1}{\sqrt{\xi}} \right)}} \quad (A.20)$$

b) Voltage comparison

Voltage in point (G) similar to point (D) can be calculated according to eq. A.16 as follows:

$$\left(\frac{E_{mG}}{\omega} \right)^2 = (L_{dm} L_{qm}) \cdot I_{mG}^2 \quad (A.21)$$

Using eqs. A.21 and A.5 for voltage ratio will give:

$$\frac{E_{mA}}{E_{mG}} = \sqrt{\frac{1}{2} \left(\frac{L_{dm}^2 + L_{qm}^2}{L_{dm} \cdot L_{qm}} \right)} \cdot \left(\frac{I_{mA}}{I_{mG}} \right) = \sqrt{\frac{\left(\xi + \frac{1}{\xi} \right)}{\left(\sqrt{\xi} + \frac{1}{\sqrt{\xi}} \right)}} \quad (A.22)$$

c) Power factor comparison

Power factor in point (G) is maximum and in point (A) it is according to eq. A.6, thus power factor ratio can be written as follows:

$$\frac{IPF_A}{IPF_G} = \frac{\frac{\xi - 1}{\sqrt{2(\xi^2 + 1)}}}{\frac{\xi - 1}{\xi + 1}} = \frac{\frac{1}{2} \left(\sqrt{\xi} + \frac{1}{\sqrt{\xi}} \right)}{\sqrt{\frac{1}{2} \left(\xi + \frac{1}{\xi} \right)}} \quad (A.23)$$

d) Power comparison

Frequency and torque are the same for both points therefore the power will be the same as well.

e) Apparent power (kVA) comparison

Using eqs. A.20 and A.22 for kVA ratio gives:

$$\frac{kVA_A}{kVA_G} = \frac{E_{mA} \cdot I_{mA}}{E_{mG} \cdot I_{mG}} = \frac{\sqrt{\frac{1}{2} \left(\xi + \frac{1}{\xi} \right)}}{\frac{1}{2} \left(\sqrt{\xi} + \frac{1}{\sqrt{\xi}} \right)} \quad (A.24)$$

12.2 Appendix B: Field-weakening range calculation.

12.2.1 Maximum torque strategy (T)

For this case, maximum torque is targeted below base speed, assuming saturation and R_s , L_{sl} , R_c are neglected. For the base point, where the maximum limit for inverter voltage v_0 and maximum current i_0 are reached, the voltage equation is as follow:

$$v_0^2 = (\omega_0 L_q i_{q0})^2 + (\omega_0 L_d i_{d0})^2 \quad (B.1)$$

At this point we have: $\theta_0 = \frac{\pi}{4}$, $\delta_0 = \tan^{-1} \frac{1}{\xi}$, $i_{d0} = i_0 \cos \theta_0$, $i_{q0} = i_0 \sin \theta_0$ (saturation is disregarded). Using the above equations; for the base point frequency we have:

$$v_0^2 = \omega_0^2 i_0^2 \left[\left(L_q \frac{1}{\sqrt{2}} \right)^2 + \left(L_d \frac{1}{\sqrt{2}} \right)^2 \right] \Rightarrow \omega_0^2 = \frac{v_0^2}{i_0^2 L_q^2} \frac{1}{\frac{1}{2} \left[1 + \left(\frac{L_d}{L_q} \right)^2 \right]} = \frac{v_0^2}{i_0^2 L_q^2} \frac{2}{1 + \xi^2} \Rightarrow$$

$$\omega_0 \Big|_{\max.T} = \frac{v_0}{i_0 L_q} \sqrt{\frac{2}{1 + \xi^2}} \quad (B.2)$$

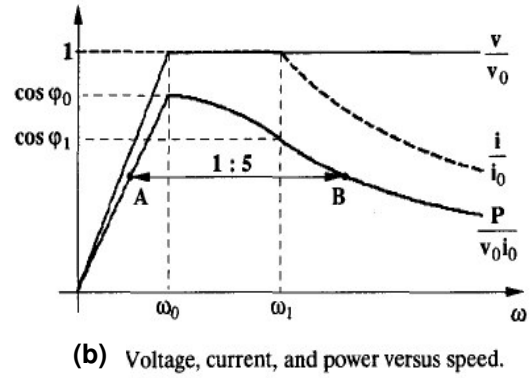
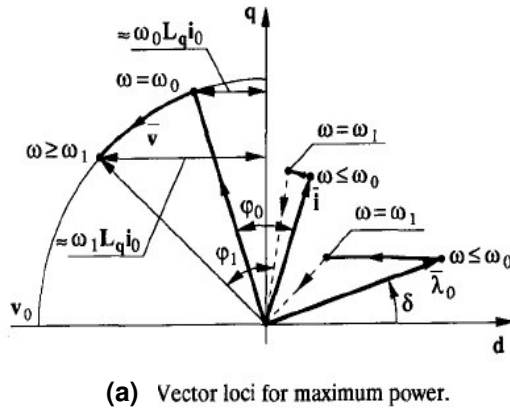


Fig. 12.3: Maximum torque field weakening [3].

The Next stage for increasing the speed is to increase the frequency at maximum allowed voltage and current, and this means moving from base point to point one (in Fig. 12.3 where $\omega = \omega_1$). At this point the flux angle reaches its maximum of 45 deg. beyond that the torque is reduced if the flux angle is increased more than 45 deg.

At point one there are: $\delta_1 = \frac{\pi}{4}$, $\theta_1 = \tan^{-1} \xi$, $i_{d1} = i_0 \cos \theta_1$, $i_{q1} = i_0 \sin \theta_1$, and voltage equation can be written as:

$$v_0^2 = (\omega_1 L_q i_{q1})^2 + (\omega_1 L_d i_{d1})^2 \quad (B.3)$$

Dividing eq. B.1 by eq. B.3 gives:

$$\left(\frac{\omega_0}{\omega_1} \right)^2 \cdot \frac{(L_q i_{q0})^2 + (L_d i_{d0})^2}{(L_q i_{q1})^2 + (L_d i_{d1})^2} = 1 \quad \Rightarrow$$

$$r = \frac{\omega_1}{\omega_0} \Big|_{\max.T} = \frac{1}{2} \left(\xi + \frac{1}{\xi} \right) \quad (B.4)$$

12.2.2 Maximum power factor strategy (PF)

Base point for maximum PF is also defined as the maximum reachable torque point at maximum voltage and current capacity of the inverter (v_0, i_0). Voltage equation at this point is as follows, however the upper operating point is defined at maximum PF:

$$v_0^2 = (\omega_0 L_q i_{q0})^2 + (\omega_0 L_d i_{d0})^2 \quad (B.5)$$

and: $\delta_1 = \frac{\pi}{4}$, $\theta_1 = \tan^{-1} \xi$, $i_{d1} = i_0 \cos \theta_1$, $i_{q1} = i_0 \sin \theta_1$.

Therefore voltage equation can be written as:

$$v_0^2 = \omega_0^2 i_0^2 [(L_q \sin \theta_0)^2 + (L_d \cos \theta_0)^2] \Rightarrow \omega_0^2 = \frac{v_0^2}{i_0^2 L_q^2} \frac{1}{\frac{1}{2} \left[1 + \left(\frac{L_d}{L_q} \right)^2 \right]} = \frac{v_0^2}{i_0^2 L_q^2} \frac{2}{1 + \xi^2} \Rightarrow$$

$$\omega_0 \big|_{\max.PF} = \frac{v_0}{i_0 L_q} \sqrt{\frac{2}{1 + \xi^2}} \quad (B.6)$$

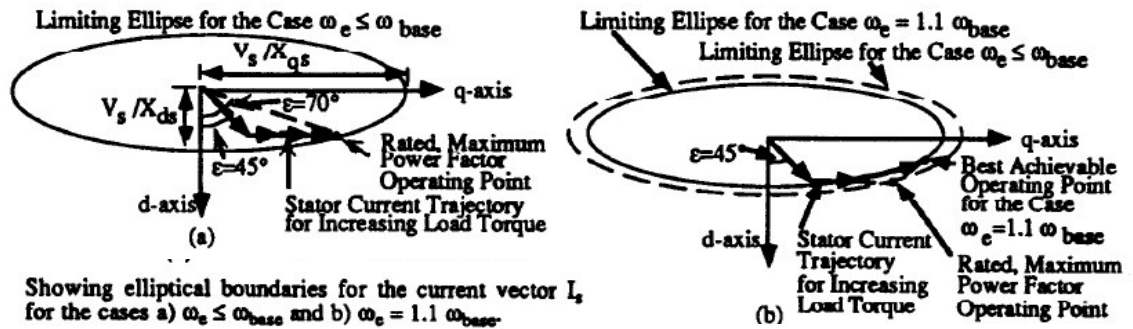


Fig. 12.4: Maximum power factor field weakening [9].

For the field weakening range a complete analysis is presented in [33, Lipo], the result is summarized by the equation below:

$$r = \frac{\omega_1}{\omega_0} \bigg|_{\max.PF} = \frac{1}{2} \left(\sqrt{\xi} + \frac{1}{\sqrt{\xi}} \right) \quad (B.7)$$

12.3 Appendix C: Optimum insulation ratio for a simple anisotropic structure

Considering anisotropic structure in Fig. 12.5, reluctances in the d- and q-axis can be calculated from the following equations:

$$R_q = \frac{Dt}{\mu_0 DL} = \frac{t}{\mu_0 L} \quad (C.1)$$

$$R_d = \frac{D}{\mu_0 \mu_r D(1-t)L} = \frac{1}{\mu_0 \mu_r (1-t)L} \quad (C.2)$$

where:

$$t = \frac{\Delta \text{total} - \text{insulation}}{\text{total} - \text{width}} = \frac{w_i}{w_s + w_i} = \frac{1}{\frac{1}{k_{wq}} + 1} \quad (C.4)$$

$$k_{wq} = \frac{\Delta \text{total} - \text{insulation}}{\text{total} - \text{iron}} = \frac{w_i}{w_s} = \frac{1}{\frac{1}{t} - 1} \quad (C.3)$$

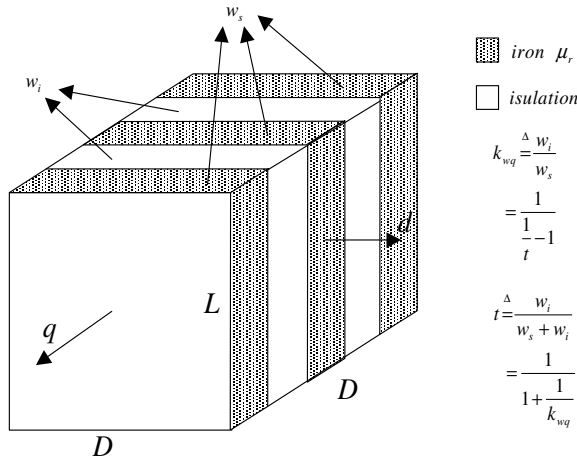


Fig. 12.5: A simple anisotropic structure

On the other hand for the difference in inductances:

$$\frac{\partial}{\partial t}(L_d - L_q) = 0 \Leftrightarrow \frac{\partial}{\partial t}\left(\frac{1}{R_d} - \frac{1}{R_q}\right) = 0 \Rightarrow t|_{\max.T} = \frac{1}{\sqrt{\mu_r}}$$

And consequently for optimum insulation ratio at maximum torque:

$$t|_{\max.T} = \frac{1}{\sqrt{\mu_r}} \Leftrightarrow k_{wq}|_{\max.T} = \frac{1}{\sqrt{\mu_r} - 1} \quad (C.5)$$

Similarly for the saliency ratio:

$$\frac{\partial}{\partial t}\left(\frac{L_d}{L_q}\right) = 0 \Leftrightarrow \frac{\partial}{\partial t}\left(\frac{R_q}{R_d}\right) = 0 \Rightarrow t|_{\max.PF} = 0.5$$

And for optimum insulation ratio at maximum power factor:

$$t|_{\max.PF} = 0.5 \Leftrightarrow k_{wq}|_{\max.PF} = 1 \quad (C.6)$$

12.4 Appendix D: Torque equations in constant current and constant voltage conditions

Mainly there are two different operations condition: constant voltage and constant current, in constant current condition by combining eqs. 2.12 and 2.15 we can write, see Fig. 12.6 (right):

$$\begin{aligned}
 T &= \frac{3}{2} \frac{p}{2} (L_{dm} - L_{qm}) \cdot I_m^2 \sin(2\theta) = \\
 &= \frac{3}{2} \frac{p}{2} (L_{dm} - L_{qm}) \cdot I_m^2 \sin(2 \cdot \tan^{-1}(\xi \cdot \tan \delta)) \quad (D.1)
 \end{aligned}$$

Similarly in constant voltage condition by combining eqs. 2.14 and 2.15 we can write, see Fig. 12.6 (left):

$$\begin{aligned}
 T &= \frac{3}{2} \frac{p}{2} \left(\frac{1}{L_{qm}} - \frac{1}{L_{dm}} \right) \cdot \left(\frac{E_m}{\omega} \right)^2 \sin(2\delta) = \\
 &= \frac{3}{2} \frac{p}{2} \left(\frac{1}{L_{qm}} - \frac{1}{L_{dm}} \right) \cdot \left(\frac{E_m}{\omega} \right)^2 \sin \left(2 \cdot \tan^{-1} \left(\frac{\tan \theta}{\xi} \right) \right) \quad (D.2)
 \end{aligned}$$

Actually in Figs. 12.1 and 12.2 these eqs. are used to draw the constant voltage and current trajectories vs. current angle.

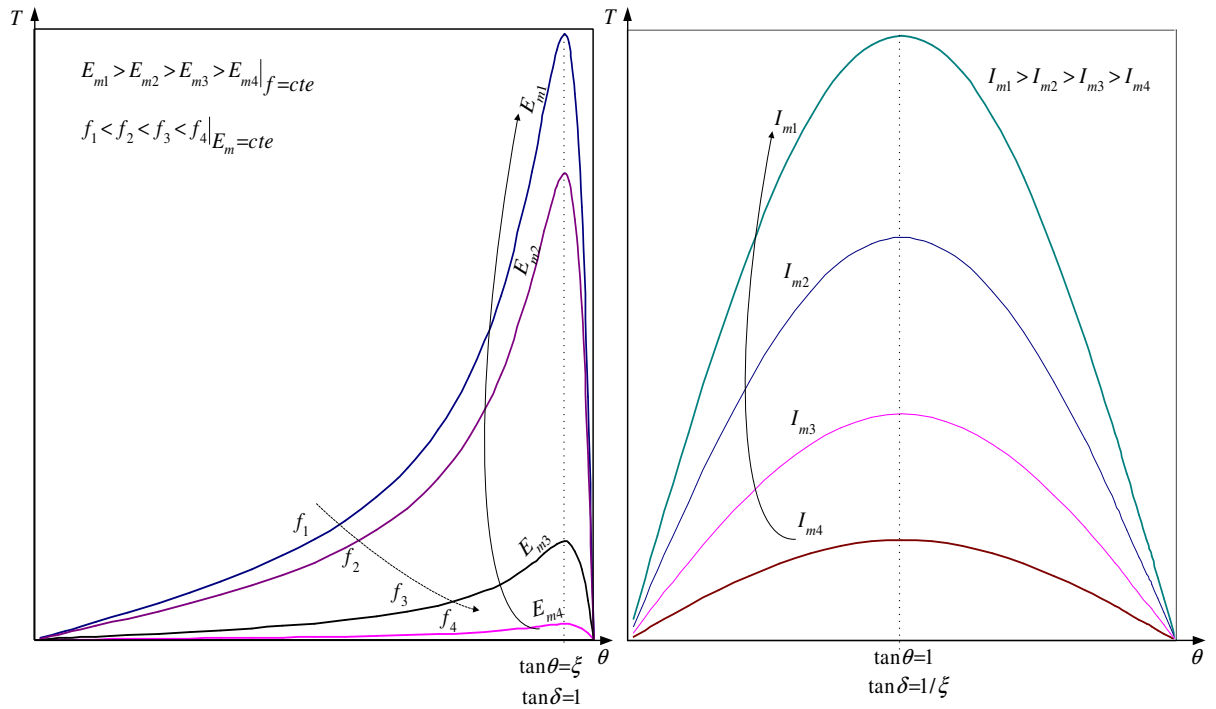


Fig. 12.6: Constant voltage (left) for different voltage and constant current (right) for different current torque trajectories vs. current angle (ideal conditions).